

Diagrammatic routes to non-local correlations beyond dynamical mean field theory

G. Rohringer,^{1,2} H. Hafermann,³ A. Toschi,² A. A. Katanin,^{4,5} A. E. Antipov,^{6,7} M. I. Katsnelson,^{8,5} A. I. Lichtenstein,^{9,5} A. N. Rubtsov,^{1,10} and K. Held²

¹*Russian Quantum Center, 143025 Skolkovo, Russia*

²*Institute for Solid State Physics, TU Wien, 1040 Vienna, Austria*

³*Mathematical and Algorithmic Sciences Lab, France Research Center, Huawei Technologies France SASU, 92100 Boulogne-Billancourt, France*

⁴*Institute of Metal Physics, Russian Academy of Sciences*

⁵*Ural Federal University, 620990 Ekaterinburg, Russia*

⁶*Department of Physics University of Michigan, Randall Laboratory, Ann Arbor, Michigan 48109-1040*

⁷*Station Q, Microsoft Research, Santa Barbara, California 93106-6105*

⁸*Radboud University Nijmegen, Institute for Molecules and Materials, NL-6525 AJ Nijmegen, The Netherlands*

⁹*I. Institut für Theoretische Physik, Universität Hamburg, Jungiusstraße 9, D-20355 Hamburg, Germany*

¹⁰*Department of Physics, M.V. Lomonosov Moscow State University, 119991 Moscow, Russia*

(Dated: May 2, 2022)

Strong electronic correlations pose one of the biggest challenges to solid state theory. We review recently developed methods that address this problem by starting with the local, eminently important correlations of dynamical mean field theory (DMFT). On top of this, non-local correlations on all length scales are generated through Feynman diagrams, with a local two-particle vertex instead of the bare Coulomb interaction as a building block. With these diagrammatic extensions of DMFT long-range charge-, magnetic-, and superconducting fluctuations and (quantum) criticality can be addressed in strongly correlated electron systems. We provide an overview of the successes and results achieved—hitherto mainly for model Hamiltonians—and outline future prospects for realistic material calculations.

PACS numbers: 71.10.-w,71.10.Fd,71.27.+a

CONTENTS

I. Introduction	1	IV. Applications and Results	31
A. Brief History	3	A. Hubbard Model	31
B. Outline	4	1. Three dimensions	32
II. Diagrammatics at the two particle level	5	2. Two dimensions: square lattice at half filling	33
A. Formalism and symmetries	5	3. Two dimensions: square lattice off half-filling	36
B. Synopsis of dynamical mean-field theory (DMFT)	8	4. Two dimensions: triangular lattice	37
C. Physical contents of the local vertex	9	5. One and zero dimensions	38
D. Calculation of the local vertex	11	B. Heavy fermions and Kondo lattice model	39
1. Exact Diagonalization (ED)	12	C. Falicov-Kimball model	40
2. Quantum Monte Carlo (QMC)	12	D. Models of Disorder	42
3. Handling vertex asymptotics	13	E. Non-local interactions and multi-orbitals	43
III. Methods	13	V. Open source implementations	45
A. Dynamical vertex approximation (DGA)	14	VI. Conclusion and outlook	46
1. Parquet DGA	14	Acknowledgements	48
2. Ladder DGA	15	References	48
3. <i>Ab initio</i> DGA for materials calculations	16		
4. QUADRILEX: a functional integral perspective	17		
B. Dual fermion (DF) theory	18		
1. Non-local expansion scheme	22		
2. Generalizations and superperturbation theory	22		
C. One-particle irreducible (1PI) approach	23		
D. DMFT plus functional renormalization group	25		
E. Extending vertex approaches to clusters	26		
F. DMFT + non-local self-energy	27		
G. EDMFT++ theories	28		
1. EDMFT+GW approach	29		
2. Dual boson (DB) approach	29		
3. TRILEX approach	31		

I. INTRODUCTION

The understanding of strongly correlated systems counts among the most difficult problems of solid state physics, since standard perturbation theory in terms of the bare Coulomb interaction breaks down. Dynamical mean field theory (DMFT) represents a breakthrough in this respect as it includes a major part of electronic correlations: the local ones. It does so in a nonperturbative

way. For a three-dimensional ($3d$) lattice at elevated temperature and in the absence of a close-by second-order phase transition, these local DMFT correlations prevail. They bring forth, among others, quasiparticle renormalizations, Mott-Hubbard metal-insulator transitions, orbital, charge and magnetic ordering, see [Georges *et al.*, 1996](#) for a review. Building on its success, DMFT nowadays is routinely employed for realistic material and non-equilibrium calculations, for reviews see [Kotliar *et al.*, 2006](#), [Held, 2007](#), [Katsnelson *et al.*, 2008](#) and [Aoki *et al.*, 2014](#), respectively. It also fostered the development of new impurity solvers ([Bulla *et al.*, 2008](#); [Gull *et al.*, 2011b](#)).

Non-local correlations, on the other hand, are at the heart of some of the most fascinating physical phenomena such as high-temperature superconductivity ([Bednorz and Müller, 1986](#)) and quantum criticality ([von Löhneysen *et al.*, 2007](#)). They are also responsible for the long-range correlations in the vicinity of phase transitions or [Lifshitz, 1960](#) transitions, and play a crucial role in the physics of graphene ([Kotov *et al.*, 2012](#)) to name but a few. These non-local correlations are missing in DMFT, which is mean field in space but takes into account correlations in time. Often we can understand non-local physics in terms of perturbation theory or the ladder replication thereof. Let us take, for example, the elementary excitations of a ferromagnet: magnons. These can be described by the repeated scattering of a minority-spin electron at the prevalent majority-spin electrons, see [Fig. 1 \(a\)](#). This corresponds to ladder-type Feynman diagrams which allows us to calculate the magnetic susceptibility, or to identify its spin wave poles as the elementary excitations of the system: the magnons. As described by [Hertz and Edwards, 1973](#) one can diagrammatically “close” the Green’s function in the majority-spin channel (dashed line in [Fig. 1](#)) to describe the scattering of quasiparticles with the particle-hole excitations which yields the minority-spin self-energy.

Such feedback of collective excitations on the fermionic degrees of freedom is crucially important, e.g., for the non-quasiparticle states in the spin gap of half-metallic ferromagnets. These are an important limiting factor for spintronics applications, see [Katsnelson *et al.*, 2008](#) for a review. In DMFT such magnon contributions to the self-energy are only contained in its local version, where all sites in [Fig. 1](#) are the same, $i = j = \dots = k$. In \mathbf{k} -space, this translates into a \mathbf{k} -independent contribution. Instead of a magnon dispersion relation $E(\mathbf{k})$, in DMFT we have a single magnon energy and a gap in the magnon spectrum. Consequently, the peculiar importance of low-energy long-range magnon fluctuations is *not* reflected in the DMFT self-energy.

The same kind of diagrams but also including $SU(2)$ -related transversal spin fluctuations describe the paramagnons in the paramagnetic phase ([Moriya, 1985](#)). These are nothing but the spin fluctuations dominating in the

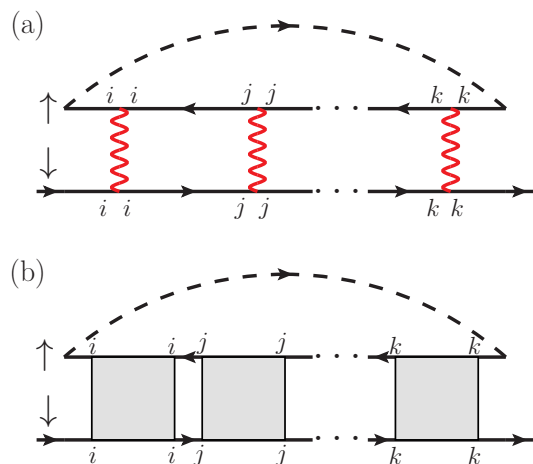


Figure 1 (Color online) (a) Ladder series of Feynman diagrams describing the repeated scattering of a minority (down) spin at the majority (up) spins. Wiggly line: (local) interaction at sites i, j, k etc.; straight line: interacting Green’s function line yields the magnon contribution to the self-energy. (b) In diagrammatic extensions of DMFT the same kind of diagrams are generated with the non-perturbative local vertex (gray box) instead of the bare interaction as a building block. This local vertex contains the bare interaction and all local vertex corrections.

vicinity of a magnetic phase transition. Their effect on the spectrum and self-energy may be dramatic and may alter a metallic into a (pseudo-) gapped phase. Such physics is missing in DMFT which does not feature these precursors of the forthcoming magnetic ordering. The spin fluctuations may also serve as a pairing glue, an attractive interaction in the particle-particle or cooperon channel, possibly leading to high-temperature superconductivity ([Scalapino, 2012](#)). Also at a quantum critical point the paramagnon contribution is important. Indeed, it is at the basis of the [Hertz, 1976](#), [Millis, 1993](#) and [Moriya, 1985](#) theory of quantum criticality.

The aim of the diagrammatic extensions of DMFT is to describe the physics of long-ranged collective excitations – but now for strongly correlated systems. In fact, the key to such physics lies in Feynman diagrams such as those in [Fig. 1 \(a\)](#), but with the bare interaction replaced by a strongly renormalized, local two-particle vertex, as illustrated in [Fig. 1 \(b\)](#). This way the important local DMFT correlations can be fully included from the beginning and—through the vertex—also affect the short- and long-range correlations. As we will see, spin fluctuations and other non-local correlations such as the critical fluctuations in the vicinity of a (quantum) critical point can be described this way—even in strongly correlated systems.

A. Brief History

Let us start with a brief synopsis of the various methods and approaches that aim at extending DMFT to include non-local correlations. We recall that DMFT becomes exact in the limit of high coordination number or alternatively for dimension $d \rightarrow \infty$ (Metzner and Vollhardt, 1989). DMFT maps a lattice model onto the self consistent solution of an Anderson impurity model (AIM) (Georges and Kotliar, 1992) which can be solved numerically (Jarrell, 1992).

From the very beginning, there have been attempts to include non-local correlations beyond the local DMFT correlations. The first such approach was the $1/d$ approach of Schiller and Ingersent, 1995 which includes all diagrams to next order ($1/d$) and results in a two-site impurity model. This way non-local correlations between neighboring sites are included. A systematic expansion of DMFT has also been proposed in the strong coupling limit by Stanescu and Kotliar, 2004, following the lines of Pairault *et al.*, 1998.

Particularly important and widely employed are cluster extensions of DMFT: the dynamical cluster approximation (DCA) by Hettler *et al.*, 1998 and the cluster DMFT by Lichtenstein and Katsnelson, 2000 and Kotliar *et al.*, 2001. These map a lattice model onto a cluster of sites embedded in a dynamical mean field. Thereby non-local correlations within the cluster are accounted for, and those to the outside (described by a generalized DMFT bath) are neglected. Impressive successes of these approaches are the description of pseudogap physics and unconventional superconductivity in the Hubbard model. Indeed, cluster extensions of DMFT became an integral part of the theory of high-temperature superconductivity, for more recent results and larger clusters see Gull *et al.*, 2013, Harland *et al.*, 2016, Sordi *et al.*, 2011 and Sakai *et al.*, 2012. Numerical limitations due to the exponential growth of the cluster Hilbert space restrict these cluster extensions to relatively small clusters of about 10×10 sites in practice, and hence to short-range correlations even in two dimensions ($2d$) and for a single orbital. Cluster extensions have been excellently reviewed by Maier *et al.*, 2005a. In this review we focus instead on the complementary, diagrammatic extensions of DMFT.

Motivated by identifying particularly important contributions missing in DMFT, first diagrammatic extensions supplemented the local DMFT self-energy by the non-local one of another approach. For example, in the GW +DMFT approach (Biermann *et al.*, 2003; Sun and Kotliar, 2002), this is the non-local screened exchange. Sadovskii *et al.*, 2005 on the other hand added spin-fluctuations contained in the spin-fermion model and Kitatani *et al.*, 2015 those of the fluctuation exchange approximation (FLEX).

Dynamical vertex approaches on the other hand generate both, local and non-local, electronic correlations from

a common, underlying entity: the local but frequency-dependent (i.e., dynamical) two-particle vertex. This development started with the dynamical vertex approximation (D Γ A), see Toschi *et al.*, 2007 and the closely related work by Kusunose, 2006. D Γ A assumes the locality of the n -particle irreducible vertex, recovering DMFT for $n = 1$ and generating a non-local self-energy and susceptibility corrections for $n = 2$. One can view this as a resummation of Feynman diagrams not in terms of orders in the interaction, but in terms of the locality of diagrams – an approach which reestablishes the exact solution for $n \rightarrow \infty$. In an independent development, Rubtsov *et al.*, 2008 introduced the dual fermion (DF) approach in which the lattice problem is expressed in terms of a local reference system and a coupling to the non-local degrees of freedom. A perturbation theory around this solvable reference system is obtained by decoupling the impurities by means of dual fields through a Hubbard Stratonovich transformation. The dual fermions interact through the $n \geq 2$ -particle vertex functions of the local reference system. In practice the three-particle and all higher-order vertices are neglected in both D Γ A and DF. Slezak *et al.*, 2009 devised a multi-scale approach where short-range correlations are treated on a DCA cluster and long-range correlations diagrammatically. These groundbreaking works have laid the foundation for further generalizations and developments of the methods and various applications, of which we provide a brief overview in the following:

The one-particle irreducible (1PI) approach by Rohringer *et al.*, 2013 is based on a functional in terms of the one-particle irreducible vertex; it inherits properties of both D Γ A and DF. The dynamical mean field theory to functional renormalization group (DMF 2 RG) approach by Taranto *et al.*, 2014 exploits the functional renormalization group (fRG) to generate the non-local diagrams beyond DMFT. The triply-irreducible local expansion (TRILEX) of Ayril and Parcollet, 2015 is based on the three-point fermion-boson vertex. The non-local expansion scheme of Li, 2015 is a framework for expanding around a local reference problem which includes DF and the cumulant expansion as special cases. Extensions to non-equilibrium (Muñoz *et al.*, 2013) and real-space formulations (Takemori *et al.*, 2016; Valli *et al.*, 2010) are also possible. All of these approaches are closely related and rely on the same concept of taking the local vertex and generating non-local interactions from it, as illustrated in Fig. 1 (b). They differ in the building blocks of the new perturbation expansion, in particular the vertex (e.g., irreducible or full), the type diagrams generated (e.g., ladder or parquet) and the details of the self-consistency schemes, cf. Table II on p. 47 for an overview. They allow us to describe the same kind of physics contained in weak coupling ladder diagrams [Fig. 1 (a)], but now strong DMFT correlations are included through the vertex [Fig. 1 (b)].

In a complementary development, Si and Smith, 1996 and Chitra and Kotliar, 2000 devised the extended DMFT (EDMFT), which describes the local correlations induced by non-local interactions, which can be actually mapped onto local bosonic degrees of freedom. The dual boson (DB) approach of Rubtsov *et al.*, 2012 also addresses non-local interactions, but it treats, in the spirit of the DF approach, single- and two-particle excitations on the same footing. DB explicitly includes long-range bosonic modes and hence goes much beyond EDMFT. In DFA the non-local interaction can also be taken into account, in the form of a bare non-local vertex which allows for realistic *ab-initio* DFA material calculations (Galler *et al.*, 2017; Toschi *et al.*, 2011), naturally including *GW*, DMFT, and non-local spin fluctuations beyond. It is the aim of this review to provide in Sec. III a comprehensive overview of the different approaches as well as to draw a clear picture of the physics they can describe.

In the following we mention a few highlights and applications and refer the reader to Section IV for a more comprehensive discussion. The physical results obtained using the diagrammatic extensions of DMFT are similar as for cluster extensions regarding short-range non-local correlations. However, the diagrammatic extensions also include long-range correlations, and hence allow us to address physical problems that were not accessible before. This is illustrated by Fig. 2 which shows the typical momentum resolution in momentum space for cluster and diagrammatic extensions of DMFT. The improved momentum resolution allowed Rohringer *et al.*, 2011 and Hirschmeier *et al.*, 2015 to calculate the critical exponents of the antiferromagnetic phase transition in the 3*d* Hubbard model in DFA and DF, respectively. Here the long-range correlations are of particular importance in the quantum critical region close to a second-order phase transition. As one may expect from universality, these critical exponents agree with those of the Heisenberg model. In contrast, the critical exponents of the Falicov-Kimball model as determined by Antipov *et al.*, 2014 are of the Ising universality class. Schäfer *et al.*, 2016b analyzed the quantum critical point in the Hubbard model which emerges when antiferromagnetism is suppressed by doping and find unusual critical exponents because of Kohn lines on the Fermi surface. The diagrammatic extensions of DMFT also show that spin fluctuations suppress the Néel temperature significantly in 3*d* (Katanin *et al.*, 2009; Otsuki *et al.*, 2014; Rohringer *et al.*, 2011). In 2*d*, the Mott-Hubbard transition is completely suppressed since the paramagnetic phase is always insulating at sufficiently low temperature (Schäfer *et al.*, 2015a). Pertinent steps have been taken also towards our understanding of high-temperature superconductivity: Kitatani *et al.*, 2015 and Otsuki *et al.*, 2014 studied superconducting instabilities and Gunnarsson *et al.*, 2015 did a diagnostics of the fluctuations responsible for the pseudogap. Further highlights are the renormal-

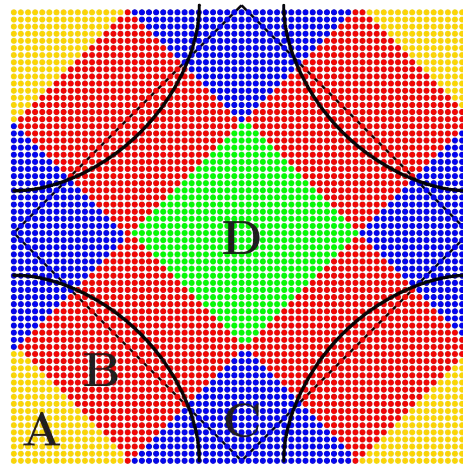


Figure 2 (Color online) Typical momentum-space discretization for diagrammatic (individual dots) and cluster extensions of DMFT (colored patches); Black lines show noninteracting Fermi surfaces for the square lattice with hopping parameters $t'/t = 0$ and $t'/t = -0.3$. Diagrammatic extension allow to resolve fine details along the Fermi surface.

ization of the plasmon dispersion by electronic correlations (van Loon *et al.*, 2014a), disorder-induced weak localization (Yang *et al.*, 2014), Lifshitz transitions in dipolar ultracold gases (van Loon *et al.*, 2016a) and the flat band formation (Fermi condensation) near Van Hove filling (Yudin *et al.*, 2014).

B. Outline

This review is organized along the following lines: We first focus, in Sec. II, on the two-particle vertex function as it is the building block of the diagrammatic approaches. In particular, Sec. II.A sets the stage and introduces the notation used throughout the review. We define the various vertex functions, discuss their symmetries and introduce the Bethe-Salpeter and parquet equations. Sec. II.B briefly recapitulates the DMFT, which serves as the starting point for the diagrammatic extensions. In Sec. II.C we discuss the physical contents of the two-particle vertex and the origin of its asymptotic behavior for large frequencies. Finally, Sec. II.D summarizes the various methods for calculating the local two-particle vertex numerically from the AIM.

In Sec. III we review the various methods developed in recent years for calculating non-local correlations beyond DMFT. Most of these have a two-particle vertex as a starting point. We start, in Sec. III.A, with the historically first vertex extension: the DFA approach. Its parquet and ladder variants are introduced in Sec. III.A.1 and Sec. III.A.2, respectively. Extensions to non-local interactions and multi-orbital models are discussed in Sec. III.A.3, before turning to the closely related func-

tional integral formalism of the quadruply-irreducible local expansion (QUADRILEX) in Sec. III.A.4. In Sec. III.B we present the DF approach, which performs a diagrammatic expansion around a local reference system in terms of dual fermions. We discuss in particular the DF diagrammatics, the choice of the local reference system, as well as scaling and convergence. The approach can be viewed as a particular diagrammatic resummation in the non-local expansion scheme discussed in Sec. III.B.1. We also discuss the generalizations of the approach and the idea of the related superperturbation theory in Sec. III.B.2. The 1PI approach can be considered as an intermediate approach in between DGA, which is based on the irreducible vertex, and DF, which is based on the reducible vertex. It inherits properties from both methods. The one-particle irreducible formalism is obtained through a Legendre transformation of the DF generating functional, as described in Sec. III.C. In Sec. III.D we present a sophisticated alternative to generate non-local correlations and vertices with the DMFT vertex as a starting point: the functional renormalization group (fRG). As we discuss in Sec. III.E, all these diagrammatic extensions can naturally be formulated using a cluster instead of a single DMFT site as a starting point. Sec. III.F is devoted to diagrammatic extensions of DMFT that are based on a perturbation in the bare interaction instead of the two-particle vertex. These approaches supplement the DMFT self-energy with a non-local one. Diagrammatic extensions of EDMFT are finally discussed in Sec. III.G: the EDMFT+GW approach in Sec. III.G.1, the dual boson approach in Sec. III.G.2 and TRILEX in Sec. III.G.3.

In Sec. IV we review the main results achieved hitherto with diagrammatic extensions of DMFT. The application to the Hubbard model in three down to zero dimensions in Sec. IV.A illustrates the physics these methods can describe and provides, at the same time, a unified picture for this fundamental model of electronic correlations. The application to the Kondo-lattice model in Sec. IV.A requires to account for the interplay between local Kondo physics and long-range antiferromagnetic fluctuations and therefore is an ideal playground for diagrammatic extensions. Applications to models for annealed and quenched disorder, i.e., the Falicov-Kimball model in Sec. IV.C and the Anderson-Hubbard model in Sec. IV.D, illustrate the versatility of diagrammatic extensions. Finally, Sec. IV.E discusses results for models and realistic material calculations with non-local interactions and multiple orbitals.

In Sec. V we provide an overview of open source codes that are available for solving the AIM, the computation of the two-particle vertex and for diagrammatic extensions of DMFT. Finally, in Sec. VI we close with a summary and outlook and with Table II providing a comparison of the various diagrammatic extensions.

II. DIAGRAMMATICS AT THE TWO PARTICLE LEVEL

A. Formalism and symmetries

Starting point for deriving the Feynman diagrammatic formalism at the one- and two-particle level is the general definition of the n -particle imaginary time Green's function:

$$G_{i_1 \dots i_{2n}}^{(n)}(\tau_1, \dots, \tau_{2n}) = (-1)^n \left\langle T_\tau \left[c_{i_1}(\tau_1) c_{i_2}^\dagger(\tau_2) c_{i_3}(\tau_3) \dots c_{i_{2n}}^\dagger(\tau_{2n}) \right] \right\rangle, \quad (1)$$

where even indices correspond to creation (c^\dagger) and odd indices to annihilation operators (c). Here $\langle \dots \rangle = \text{Tr}(e^{-\beta\mathcal{H}} \dots) / Z$ denotes the thermal average with $Z = \text{Tr}(e^{-\beta\mathcal{H}})$ being the partition function, $\beta = 1/T$ is the inverse temperature and T_τ denotes the time ordering operator. The indices $i_j \hat{=} (\mathbf{r}_j / \mathbf{k}_j, l_j, \sigma_j, \dots)$ encode the set of all degrees of freedom of the system, e.g., space coordinate (lattice site)/momentum, orbital, spin, etc. In the following we will consider mostly single-orbital systems.

From the general case, the usual one-particle Green's function in momentum space is derived as

$$G_{\mathbf{k}}(\tau) = G_{\mathbf{k}\sigma, \mathbf{k}\sigma}^{(1)}(\tau, 0) = - \left\langle T_\tau \left[c_{\mathbf{k}\sigma}(\tau) c_{\mathbf{k}\sigma}^\dagger(0) \right] \right\rangle$$

$$G_{\mathbf{k}\nu} = \int_0^\beta d\tau e^{i\nu\tau} G_{\mathbf{k}}(\tau), \quad (2)$$

where $\nu = (2n + 1)\pi/\beta$ with $n \in \mathbb{Z}$ is a fermionic Matsubara frequency (later $\omega = (2m)\pi/\beta$ denotes a bosonic Matsubara frequency). Whenever convenient, we will adopt the more compact four-vector notation $G_k \equiv G_{\mathbf{k}\nu}$ with the generalized fermionic $k \hat{=} (\nu, \mathbf{k})$ and bosonic momentum $q \hat{=} (\omega, \mathbf{q})$. For the sake of conciseness, we restrict ourselves here and in the following to the time- and lattice-translational invariant SU(2)-symmetric (paramagnetic) case. Consequently, the one-particle Green's function is diagonal in generalized momentum and spin space with $G_{\uparrow\uparrow} = G_{\downarrow\downarrow}$. From $G_{\mathbf{k}\nu}$ and its non-interacting counterpart $G_{0, \mathbf{k}\nu}$, the *one-particle irreducible* self-energy is calculated via the standard Dyson equation

$$\Sigma_{\mathbf{k}\nu} = [G_{0, \mathbf{k}\nu}]^{-1} - [G_{\mathbf{k}\nu}]^{-1}. \quad (3)$$

For the two-particle Green's function [$n=2$ in Eq. (1)] we can drop one momentum and time index due to time and lattice translational invariance and arrive at the compact form

$$G_{\sigma\sigma', \mathbf{k}\mathbf{k}'\mathbf{q}}^{(2)}(\tau_1, \tau_2, \tau_3) \equiv G_{\mathbf{k}\sigma, \mathbf{k}+\mathbf{q}\sigma, \mathbf{k}'+\mathbf{q}\sigma', \mathbf{k}'\sigma'}^{(2)}(\tau_1, \tau_2, \tau_3, 0)$$

$$G_{\sigma\sigma', \mathbf{k}\mathbf{k}'\mathbf{q}}^{(2), \nu\nu'\omega} = \int_0^\beta d\tau_1 d\tau_2 d\tau_3 e^{i\nu\tau_1} e^{-i(\nu+\omega)\tau_2} e^{i(\nu'+\omega)\tau_3}$$

$$\times G_{\sigma\sigma', \mathbf{k}\mathbf{k}'\mathbf{q}}^{(2)}(\tau_1, \tau_2, \tau_3). \quad (4)$$

The way how the frequencies are assigned to the Matsubara times and, hence, to the creation and annihilation operators in Eq. (1) is referred to as particle-hole notation. In this notation the two-particle Green's function can be viewed as scattering amplitude of an incoming particle and hole with total energy ω and total momentum \mathbf{q} , see red lines in Fig. 3 (a). It is particularly convenient for describing system where particle-hole (e.g., spin or charge) fluctuations dominate. Systems with strong particle-particle fluctuations on the other hand are easier described exploiting the so-called particle-particle representation of the two-particle Green's function that is illustrated in Fig. 3 (b). In this notation the two-particle Green's function can be interpreted as scattering amplitude between two particles with total energy and momentum $q_{pp} = q + k + k'$. Let us stress that the two-particle Green's function contains both (*ph* and *pp*) scattering processes independent of its representation. The choice of the representation corresponds only to selecting the most convenient “coordinate system” for the description of the problem (see, e.g., Gunnarsson *et al.*, 2015 and Bickers, 2004).

The two-particle Green's function depends on four spin indices corresponding to $2^4 = 16$ spin components. Due to the conservation of the total spin, 10 of them vanish and, from the remaining 6, the two components $\sigma(-\sigma)\sigma(-\sigma)$ can be expressed via $\sigma\sigma(-\sigma)(-\sigma)$ by means of the crossing symmetry (see last line in Table I). For the remaining four components $\sigma\sigma\sigma'\sigma'$ we have introduced the short-hand notation $\sigma\sigma\sigma'$ in Eq. (4). There are additional relations between these due to SU(2) symmetry (see second line in Table I). As these relations involve, however, shifts of frequency and momenta, it is more convenient to work with two ($\uparrow\uparrow$ and $\uparrow\downarrow$) components explicitly.

From the one- and two-particle Green's functions, the generalized susceptibilities are readily obtained as:

$$\begin{aligned}\chi_{\sigma\sigma',\mathbf{k}\mathbf{k}'\mathbf{q}}^{\nu\nu'\omega} &= G_{\sigma\sigma',\mathbf{k}\mathbf{k}'\mathbf{q}}^{(2),\nu\nu'\omega} - \beta G_{\mathbf{k}\nu} G_{\mathbf{k}'\nu'} \delta_{\omega 0} \delta_{\mathbf{q}0} \\ \chi_{c/s,\mathbf{k}\mathbf{k}'\mathbf{q}}^{\nu\nu'\omega} &= \chi_{\uparrow\uparrow,\mathbf{k}\mathbf{k}'\mathbf{q}}^{\nu\nu'\omega} \pm \chi_{\uparrow\downarrow,\mathbf{k}\mathbf{k}'\mathbf{q}}^{\nu\nu'\omega}.\end{aligned}\quad (5)$$

In the second line we have introduced the charge (*c*) and spin (*s*) components of the generalized susceptibility.¹ From these the corresponding physical susceptibilities (response functions) are computed in the particle-hole sector by performing the summation over all the

¹ These components have a definite spin *S* and projection S_z of the incoming particle-hole pair: The charge channel corresponds to $S = 0$, $S_z = 0$, and the spin channel to $S = 1$, $S_z = 0$. The components with $\uparrow\downarrow\downarrow\uparrow$ and $\downarrow\uparrow\uparrow\downarrow$ correspond to $S = 1$, $S_z = \pm 1$, and must be equal to $S = 1$, $S_z = 0$ due to SU(2). It is hence convenient to work with the two components (*c/s*) only. A similar decomposition into singlet and triplet channels applies for the particle-particle channel.

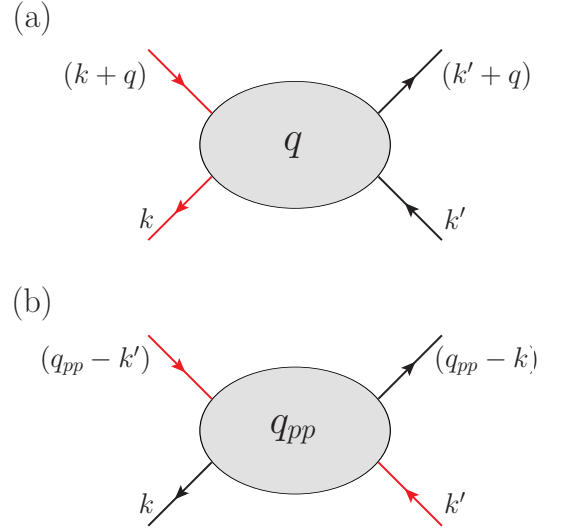


Figure 3 (Color online) Illustration of a two-particle Green's function from the (a) particle-hole and (b) particle-particle perspective, described by the corresponding frequency notations. The red arrows denote the particle and hole in (a) and the two particles in (b), which are considered as the “incoming” ones. The total frequency/momentum transferred to the system is then given by $q = (\mathbf{q}, \omega)$ and $q_{pp} = (\mathbf{q}_{pp}, \omega_{pp})$, respectively. Representation (b) can be obtained from (a) by a mere coordinate transformation in the space of the three frequencies/momenta, i.e., $q \rightarrow q_{pp} = q + k + k'$ ($k_{pp} = k$ and $k'_{pp} = k'$).

fermionic variables:

$$\chi_{r,\mathbf{q}}^{\omega} = \sum_{\substack{\nu\nu' \\ \mathbf{k}\mathbf{k}'}} \chi_{r,\mathbf{k}\mathbf{k}'\mathbf{q}}^{\nu\nu'\omega} \quad \text{with } r = c, s, \quad (6)$$

where a proper normalization of the momentum and frequency sums is implicitly assumed (i.e., $\sum_{\mathbf{k}} 1 = 1$ and $\sum_{\nu} \hat{=} \frac{1}{\beta} \sum_{\nu}$). An analogous definition holds for the physical particle-particle susceptibility where the corresponding summations have to be performed in particle-particle notation.

In order to classify the different two-particle processes diagrammatically, we can decompose the generalized susceptibility into two parts (see Fig. 4): (i) a product of two one-particle Green's functions corresponding to an independent propagation of the particle and the hole and (ii) vertex corrections to the susceptibility. The latter describes all the particle-hole scattering processes, which give rise to collective excitations. The corresponding equation, depicted diagrammatically in Fig. 4, reads:

$$\begin{aligned}\chi_{r,\mathbf{k}\mathbf{k}'\mathbf{q}}^{\nu\nu'\omega} &= -\beta \underbrace{G_{\mathbf{k}\nu} G_{(\mathbf{k}+\mathbf{q})(\nu+\omega)} \delta_{\nu\nu'} \delta_{\mathbf{k}\mathbf{k}'}}_{\chi_{0,\mathbf{k}\mathbf{k}'\mathbf{q}}^{\nu\nu'\omega}} \\ &\quad - G_{\mathbf{k}\nu} G_{(\mathbf{k}+\mathbf{q})(\nu+\omega)} F_{r,\mathbf{k}\mathbf{k}'\mathbf{q}}^{\nu\nu'\omega} G_{\mathbf{k}'\nu'} G_{(\mathbf{k}'+\mathbf{q})(\nu'+\omega)},\end{aligned}\quad (7)$$

with $r = c, s$ and the signs have been chosen in such a way that $F_{\uparrow\downarrow,\mathbf{k}\mathbf{k}'\mathbf{q}}^{\nu\nu'\omega} \rightarrow +U$ for $U \rightarrow 0$. $F_{r,\mathbf{k}\mathbf{k}'\mathbf{q}}^{\nu\nu'\omega}$ is the

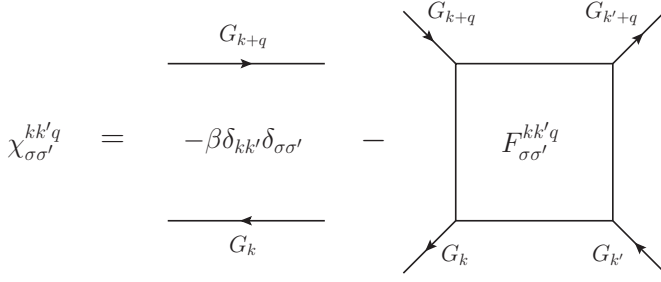


Figure 4 Decomposition of the generalized susceptibility into a disconnected and a connected part. The first part describes the independent propagation of the particle-hole pair in the interacting system, while the second originates from all possible scattering processes between them. For readability of the diagram we have adopted the four-vector notation.

two-particle vertex function, which contains all Feynman diagrams connecting all four external Green's functions. In the Fermi-liquid regime, F is proportional to the scattering amplitude between quasi-particles [Abrikosov et al. 1975](#).

A refined classification is obtained by categorizing the Feynman diagrams of F in terms of their *two-particle reducibility*. All Feynman diagrams contributing to F can be split into four topologically distinct classes. They are either fully two-particle irreducible, or reducible in one of three channels: particle-hole (ph), vertical particle-hole (\overline{ph}) or particle-particle channel (pp). For example, a diagram is said to be reducible in the particle-hole channel when it can be split into two parts by cutting two lines corresponding to a particle-hole pair, see Fig. 5. This decomposition is at the heart of the so-called *parquet* equations which have been first introduced by [Diatlov et al., 1957](#) (cf. [Bickers, 2004](#); [Bickers and White, 1991](#); [De Dominicis, 1962](#); [De Dominicis and Martin, 1964a](#); [Janiš, 2001](#); and [Janiš et al., 2017](#)). Denoting by $\Phi_{\ell,r,\mathbf{k}\mathbf{k}'\mathbf{q},\uparrow\downarrow}^{\nu\nu'\omega}$ the set of diagrams which are two-particle reducible (2PR) in channel ℓ and by $\Lambda_{r,\mathbf{k}\mathbf{k}'\mathbf{q}}^{\nu\nu'\omega}$ the set of all fully irreducible diagrams, we have the unique decomposition (cf. Fig. 5)

$$F_{r,\mathbf{k}\mathbf{k}'\mathbf{q}}^{\nu\nu'\omega} = \Lambda_{r,\mathbf{k}\mathbf{k}'\mathbf{q}}^{\nu\nu'\omega} + \Phi_{ph,r,\mathbf{k}\mathbf{k}'\mathbf{q}}^{\nu\nu'\omega} + \Phi_{\overline{ph},r,\mathbf{k}\mathbf{k}'\mathbf{q}}^{\nu\nu'\omega} + \Phi_{pp,r,\mathbf{k}\mathbf{k}'\mathbf{q}}^{\nu\nu'\omega}. \quad (8)$$

We want to stress that one has to clearly discriminate between the index ℓ which refers to a subset of diagrams for the full vertex with a certain topology (reducible or irreducible in a given channel) and the index r which represents just the spin arguments of the vertex [specifically the linear combination as in Eq. (5) so that without vertex corrections and a Hubbard interaction U : $F_d = U$, $F_s = -U$]. In the literature both are often referred to as “channels” although both concepts are completely different. In fact, the decomposition (8) holds independently of the considered spin combination r .

Alternatively, the contributions to F can be divided

into only two parts, i.e., those which are reducible and those which are irreducible in a given channel ℓ :

$$F_{r,\mathbf{k}\mathbf{k}'\mathbf{q}}^{\nu\nu'\omega} = \Gamma_{\ell,r,\mathbf{k}\mathbf{k}'\mathbf{q}}^{\nu\nu'\omega} + \Phi_{\ell,r,\mathbf{k}\mathbf{k}'\mathbf{q}}^{\nu\nu'\omega}. \quad (9)$$

This defines the vertex $\Gamma_{\ell,r,\mathbf{k}\mathbf{k}'\mathbf{q}}^{\nu\nu'\omega}$ which is two-particle irreducible in channel ℓ (see Fig. 5 for $\ell = ph$). They are related to the full vertex F through the *Bethe-Salpeter* equations (BSE)². For the $\ell = ph$ -channel ([Bickers, 2004](#); [Bickers and White, 1991](#)), the BSE explicitly reads

$$F_{r,\mathbf{k}\mathbf{k}'\mathbf{q}}^{\nu\nu'\omega} = \Gamma_{ph,r,\mathbf{k}\mathbf{k}'\mathbf{q}}^{\nu\nu'\omega} + \sum_{\mathbf{k}_1\nu_1} \Gamma_{ph,r,\mathbf{k}\mathbf{k}'\mathbf{q}}^{\nu\nu_1\omega} \times G_{\mathbf{k}_1\nu_1} G_{(\mathbf{k}_1+\mathbf{q})(\nu_1+\omega)} F_{r,\mathbf{k}_1\mathbf{k}'\mathbf{q}}^{\nu_1\nu'\omega}. \quad (10)$$

Note that due to SU(2) symmetry, the charge ($r = c$) and the spin ($r = s$) sectors do not couple. From a diagrammatic perspective the BSEs correspond to an infinite summation of ladder diagrams. Physically, they describe collective excitations in the different scattering channels while the parquet equation (8) provides for their mutual renormalization.

Eqs. (8) and (10) form a closed set of four equations for F , Γ_ℓ ($\ell = pp, ph, \overline{ph}$) and Λ , which can be solved self-consistently, provided one of these five quantities and the one-particle Green's function are known (for the case that Λ is given see left part of Fig. 6). As we usually do not know the exact vertex, we have to consider approximations. For instance the so-called parquet approximation assumes that the fully irreducible vertex is replaced by the constant bare interaction, i.e., $\Lambda^{kk'q} = U$ ([Bickers, 2004](#)); or in parquet DGA, $\Lambda^{kk'q}$ is approximated by its local counterpart ($\Lambda^{\nu\nu'\omega}$).

The above set of four parquet equations needs to be supplemented by the self-consistent calculation of the one-particle Green's function and self energy, see Fig. 6 (right). For obtaining these one-particle functions from the two-particle vertex, we exploit the relation between Green's functions of different particle number in the (Heisenberg) equation of motion. This leads to the Schwinger-Dyson equation, which connects the vertex F with the self-energy Σ , and reads for a Hubbard-like model with a local interaction U :

$$\Sigma_{\mathbf{k}\nu} = \frac{Un}{2} - U \sum_{\substack{\nu_1\nu_2 \\ \mathbf{k}_1\mathbf{k}_2}} F_{\uparrow\downarrow,\mathbf{k}\mathbf{k}'\mathbf{q}}^{\nu\nu_1\omega} G_{\mathbf{k}'\nu_1'} G_{(\mathbf{k}'+\mathbf{q})(\nu_1'+\omega)} \times G_{(\mathbf{k}+\mathbf{q})(\nu+\omega)}. \quad (11)$$

² The BSEs can be equivalently formulated for the generalized susceptibilities:

$$\chi_{r,\mathbf{k}\mathbf{k}'\mathbf{q}}^{\nu\nu'\omega} = \chi_{0,\mathbf{k}\mathbf{k}'\mathbf{q}}^{\nu\nu'\omega} - \sum_{\substack{\nu_1\nu_2 \\ \mathbf{k}_1\mathbf{k}_2}} \chi_{0,\mathbf{k}\mathbf{k}_1\mathbf{q}'}^{\nu\nu_1\omega} \Gamma_{\ell,r,\mathbf{k}_1\mathbf{k}_2\mathbf{q}}^{\nu_1\nu_2\omega} \chi_{r,\mathbf{k}_2\mathbf{k}'\mathbf{q}}^{\nu_2\nu'\omega},$$

where the bare bubble $\chi_{0,\mathbf{k}\mathbf{k}'\mathbf{q}}^{\nu\nu'\omega}$ has been defined in Eq. (7).

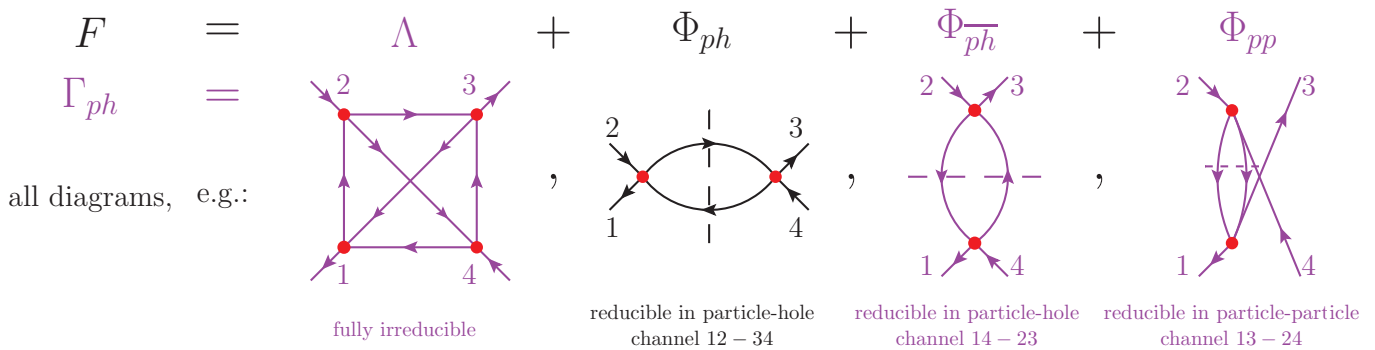


Figure 5 (Color online) Parquet decomposition of the one-particle irreducible vertex F into its two-particle fully irreducible contribution Λ and the three contributions Φ_ℓ reducible in the particle-hole- (ph), vertical particle-hole- \overline{ph} and particle-particle channel (pp). The latter can be separated into two parts by cutting two Green's functions as indicated by the dashed lines. For instance, for the $\ell = ph$ channel, the legs 12 and 34 are separated. The subset of diagrams marked in violet are part of the irreducible ph vertex $\Gamma_{\ell=ph}$ which contains all diagrams which cannot be separated in channel $\ell = ph$. Note that all diagrams in this figure are meant as so-called *skeleton* diagrams, i.e., all lines correspond to full interacting Green's functions.

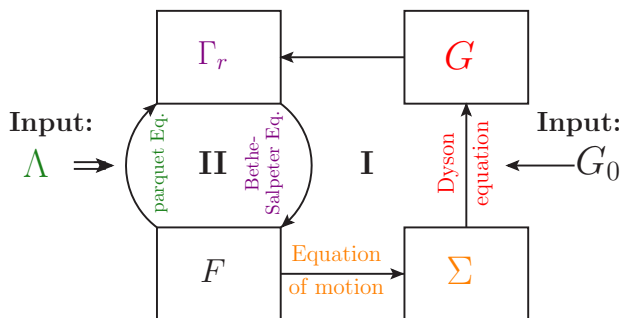


Figure 6 (Color online) Flow diagram for solving the parquet equations. Left: If the fully irreducible vertex Λ is given, the parquet Eq. (8) and the three BSE (10) for $\ell = ph, \overline{ph}, pp$ allow us to calculate the four unknowns F, Γ_ℓ . Right: As in the BSE (10) also the interacting Green's function G enters, we need to extend the self consistency loop by two additional unknowns [G and Σ] and equations [the equation of motion (11) and the Dyson Eq. (3)]. The latter has the non-interacting Green's function G_0 as input.

Here, n denotes the particle density of the system. For the generalization to multi orbitals and non-local interactions, see, for example, [Galler et al., 2017](#). Eq. (11) represents an exact relation between the two- and the one-particle correlation functions. Hence for a given Λ we have altogether five equations and five unknowns which can be calculated self-consistently as indicated in Fig. 6.

In diagrammatic extensions of DMFT discussed in Sec. III, the Schwinger-Dyson Eq. (11) is also often used when obtaining F via other (e.g. ladder) resummations of Feynman diagrams. The Schwinger-Dyson eq. also provides the basis for the fluctuation diagnostics method. By performing partial summations over \mathbf{k}' and ν' in Eq. (11), the physical origin of the spectral features in the self-energy can be identified ([Gunnarsson et al., 2015](#)).

The dependence of two-particle Green's- and vertex

functions on several indices makes their numerical calculations, post-processing and storage evidently much more challenging than that of the single-particle Green's functions. Hence exploiting all the symmetries of the system is vital to reduce the numerical and memory storage requirements. Various symmetry relations are summarized in Table I for Hubbard-type models. While the symmetry properties reported there are valid for the vertices F and Λ , they do not hold in general for the explicitly channel dependent quantities Φ_ℓ and Γ_ℓ since the symmetry relations will mix one channel with the others. For an exhaustive discussion of the specific symmetry properties of Φ_ℓ and Γ_ℓ we refer the reader to [Rohringer, 2013](#) and [Rohringer et al., 2012](#).

Starting with the next section, we will also consider local vertex functions, Green's functions and self-energies of an AIM problem. These quantities are frequency- but not momentum-dependent. In the following we distinguish such local vertices from the lattice vertices by dropping the momentum index, i.e., we write $F_r^{\nu\nu'\omega}$ for the local full vertex instead of $F_{r,\mathbf{k}\mathbf{k}'\mathbf{q}}^{\nu\nu'\omega}$ for the lattice quantity defined in Eq. (7), and the same holds for $\Gamma_r^{\nu\nu'\omega}$ and $\Lambda_r^{\nu\nu'\omega}$. For the one-particle Green's functions and self-energies we add a label "loc", i.e., G_ν^{loc} (Σ_ν^{loc}) for the local problem (i.e., the associated AIM, see Sec. II.B) instead of $G_{\mathbf{k}\nu}$ ($\Sigma_{\mathbf{k}\nu}$) for the lattice problem. As $G_{\mathbf{k}\nu}^{\text{loc}}$ we denote the lattice Green's function function that we obtained from the Dyson Eq. (3) with Σ_ν^{loc} of the local problem as input.

B. Synopsis of dynamical mean-field theory (DMFT)

For the sake of completeness, and for setting the stage for the diagrammatic extensions that follow, let us briefly outline the DMFT approach here. For more details of the method and of its the multi-orbital extensions, we refer

Symmetry	Symmetry relation
Complex conjugation	$(F_{\sigma\sigma'}^{kk'q})^* = F_{\sigma\sigma'}^{(-k')(-k)(-q)}$
SU(2) symmetry	$F_{\sigma\sigma'}^{kk'q} = F_{(-\sigma)(-\sigma')}^{kk'q} = F_{\sigma'\sigma}^{kk'q}$ $F_{\sigma\sigma}^{kk'q} = F_{\sigma(-\sigma)}^{kk'q} - F_{\sigma(-\sigma)}^{k(k+q)(k'-k)}$
Time reversal symmetry	$F_{\sigma\sigma'}^{kk'q} = F_{\sigma'\sigma}^{k'kq} \stackrel{\text{SU}(2)}{=} F_{\sigma\sigma'}^{k'kq}$
Particle-hole symmetry ($\mu = \frac{U}{2}$ only)	$(F_{\sigma\sigma'}^{kk'q})^* = F_{\sigma\sigma'}^{kk'q}$
SU(2) _P symmetry ($\mu = \frac{U}{2}$ only)	$F_{\sigma\sigma}^{kk'q} = F_{\sigma(-\sigma)}^{k(-k'-q)(k'-k)} - F_{\sigma(-\sigma)}^{k(-k'-q)q}$
Crossing symmetry	$F_{\sigma\sigma'\sigma'}^{kk'q} = -F_{\sigma\sigma\sigma'}^{k(k+q)(k'-k)}$ $\equiv -F_{\sigma\sigma'}^{k(k+q)(k'-k)}$

Table I Summary of the symmetry relations for the vertex function F for single-orbital Hubbard-type models [in four-vector notation $k \hat{=} (\nu, \mathbf{k})$]. U denotes the local interaction parameter and μ the chemical potential. For a more detailed discussion and an illustration of the crossing symmetry see Rohringer, 2013 and Galler *et al.*, 2017, respectively.

the reader to the reviews of Georges *et al.*, 1996 and Held, 2007. A series of lecture notes on the occasion of 25 years of DMFT can be found in Pavarini *et al.*, 2014.

For simplicity, we consider here the single-band Hubbard model with Hamiltonian

$$\mathcal{H} = \sum_{ij,\sigma} t_{ij} c_{i\sigma}^\dagger c_{j\sigma} + U \sum_i n_{i\uparrow} n_{i\downarrow}, \quad (12)$$

where t_{ij} denotes the hopping amplitude between lattice sites i and j , U the local Coulomb repulsion, and $\sigma \in \{\uparrow, \downarrow\}$ the spin; $n_{i\sigma} \equiv c_{i\sigma}^\dagger c_{i\sigma}$.

DMFT is a self-consistent theory on the one-particle level, which approximates the one-particle vertex Σ to be local. This local self-energy Σ_ν^{loc} and a local Green's function G_ν^{loc} are determined self-consistently.

In particular, the *first DMFT self-consistency equation* calculates the local Green's function from the local self-energy Σ_ν^{loc}

$$G_\nu^{\text{loc}} = \sum_{\mathbf{k}} G_{\mathbf{k}\nu}^{\text{loc}}, \quad (13)$$

where $G_{\mathbf{k}\nu}^{\text{loc}}$ is the DMFT lattice Green's function obtained from Σ_ν^{loc} via the Dyson Eq. (3) reformulated as

$$G_{\mathbf{k}\nu}^{\text{loc}} = [i\nu + \mu - \varepsilon_{\mathbf{k}} - \Sigma_\nu^{\text{loc}}]^{-1}. \quad (14)$$

Here, $\varepsilon_{\mathbf{k}}$ is the Fourier-transform of t_{ij} . This step allows us to calculate G_ν^{loc} from the local, i.e., \mathbf{k} -independent Σ_ν^{loc} . As we will see in Sec. III, the DMFT lattice Green's function $G_{\mathbf{k}\nu}^{\text{loc}}$ and the difference $G_{\mathbf{k}\nu}^{\text{loc}} - G_\nu^{\text{loc}}$ appear prominently in the context of diagrammatic extensions of DMFT.

The *second DMFT self-consistency equation* is to sum *all* skeleton Feynman diagrams in terms of the local U and G_ν^{loc} to obtain the local DMFT self-energy Σ_ν^{loc} again (cf. Fig. 9 (a) in Section III.A below). These two steps are iterated until self consistency.

In practice, this second step is achieved through the numerical solution of an Anderson impurity model (AIM)

$$\mathcal{H} = \sum_{\ell\sigma} \epsilon_\ell a_{\ell\sigma}^\dagger a_{\ell\sigma} + \sum_{\ell\sigma} V_\ell a_{\ell\sigma}^\dagger c_\sigma + \text{h.c.} \\ + U n_\uparrow n_\downarrow, \quad (15)$$

which has the same interaction U as the Hubbard model (12) but only on one site. This (c) site is coupled through the hybridization V_ℓ to a bath of conduction electrons $a_{\ell\sigma}^\dagger$ at energies ϵ_ℓ . If the interacting Green's function of the AIM is the same as G_ν^{loc} , it yields the same Feynman diagrammatic contribution to the self-energy as DMFT: all local terms. To achieve the latter (at self consistency) one first calculates the local non-interacting Green's function \mathcal{G}_ν of the auxiliary AIM (at the interacting site) via the Dyson equation for the AIM

$$(\mathcal{G}_\nu)^{-1} = (G_\nu^{\text{loc}})^{-1} + \Sigma_\nu^{\text{loc}} \quad (16)$$

$$= i\nu + \mu - \underbrace{\sum_{\ell} \frac{|V_{\mathbf{k}}|^2}{i\nu + \mu - \epsilon_\ell}}_{\equiv \Delta_\nu}; \quad (17)$$

which is directly related to a corresponding hybridization function Δ_ν . Then one solves the thus defined AIM for its Green function G_ν^{loc} and uses the AIM Dyson Eq. (16) again to obtain the AIM self-energy

$$\Sigma_\nu^{\text{loc}} = (\mathcal{G}_\nu)^{-1} - (G_\nu^{\text{loc}})^{-1}. \quad (18)$$

This closes the DMFT iteration loop and, at self consistency, Σ_ν^{loc} is the DMFT self-energy. The DMFT solution yields the local Σ_ν^{loc} , G_ν^{loc} and DMFT lattice Green's function $G_{\mathbf{k}\nu}^{\text{loc}}$. At self consistency we can also calculate local two-particle Green's and vertex functions as discussed in Sec. II.D below.

C. Physical contents of the local vertex

The physical meaning of the one-particle Green's function and its 1PI counterpart, the self-energy, is nowadays

standard textbook knowledge, see e.g. [Abrikosov et al., 1975](#) and [Mahan, 2000](#). Less information is available about the physical content of the *two-particle* Green's function and its 1PI and 2PI counterparts, the so-called vertex functions, whose definitions are given in Secs. [II.A](#). Yet, in recent years, the development of diagrammatic extensions of DMFT has triggered significant progress in this field.

In this section we discuss the frequency dependence of the local DMFT vertex functions for models with a constant bare interaction U and their microscopic interpretation. This requires the analysis of the frequency-structure of all possible Feynman diagrams ([Rohringer, 2013](#); [Rohringer et al., 2012](#); [Wentzell et al., 2016](#)). The dependence of a certain diagram on the three external frequencies (ν, ν', ω) is controlled by its topology, i.e., by the way how the particles/holes enter. If two particle line, or one particle and one hole line, are attached to the same bare vertex the entire diagram will depend only on the sum/difference of their frequencies. This can be seen, e.g., in Fig. [7](#) (a) which depends only on ω but not on ν and ν' . For a fixed ω it will, hence, remain constant for arbitrarily large values of ν and ν' .

On the contrary, if an external particle/hole is connected by the bare interaction to three internal lines, the corresponding diagram will explicitly depend on its frequency. This is illustrated in Fig. [7](#) (c) where the lower right-most part of the diagram (see orange circle) gives rise to the expression $\sum_{\nu_1 \nu_2} G_{\nu'+\nu_1}^{\text{loc}} G_{\nu_2+\nu_1}^{\text{loc}} G_{\nu_2}^{\text{loc}} \dots$ which, hence, explicitly depends on ν' and will decay for large values of ν' as $1/\nu'$.

Excluding the trivial situation when all four external lines enter at the same interaction vertex (which gives just the constant contribution U), the considerations above suggest the following three-fold classification of the diagrams of F :

(i) The first group includes all diagrams where both the incoming and outgoing particle-hole (or particle-particle) pair enter at the respective same bare interaction vertex, see Fig. [7](#) (a). Such diagrams depend only on the corresponding frequency differences between the particle and hole entering the diagram at the respective same bare vertex. In the case of Fig. [7](#) (a) this frequency is ω , which one can see from the fact that all internal frequency summations in Fig. [7](#) (a) only depend on ω but not on ν and ν' . Note that the diagram Fig. [7](#) (a) is reducible in the ph channel, it belongs to Φ_{ph} in Fig. [5](#). The two other possibilities of how two external legs can be pairwise attached to bare vertices are reducible in the $\bar{p}h$ and pp channel and only *one* depend on the (bosonic) frequency $\nu - \nu'$ and $\nu + \nu' + \omega$, respectively. In Fig. [8](#) (left), these diagrams are responsible for the constant background ($\omega = 0$), the main ($\nu - \nu' = 0$) and secondary ($\nu + \nu' + \omega = 0$) diagonal of the DMFT vertex F . From a physical perspective, diagrams of type (i) correspond to physical susceptibilities. For example, the contribution to F originating from the

sum all diagrams of type (a) in Fig. [7](#) corresponds to a ph (charge or spin) susceptibility ([Rohringer et al., 2013, 2012](#); [Wentzell et al., 2016](#)).

(ii) The second class includes all diagrams where only *one* pair of external lines is attached to the same bare vertex. Their contribution depends on *two* (one bosonic and one fermionic Matsubara) frequencies, for example Fig. [7](#)(b) depends on ω and ν' but not on ν . Such diagrammatic contributions remain constant along one-dimensional *lines* in the three-dimensional frequency space. For instance, for the fixed value $\omega = 0$ and $\nu' = \pi/\beta$ in the density plot of F [Fig. [8](#) (left)], such diagrams are responsible for the well defined “+”-shaped structure, i.e., the enhanced scattering rate along $\nu', \nu = \pi/\beta$. From a physical perspective, such “eye”-shaped diagrams are related³ to a fermion-boson coupling, as it appears, e.g., in ladder DGA ([Katanin et al., 2009](#); [Rohringer and Toschi, 2016](#)), DB ([van Loon et al., 2014b](#); [Rubtsov et al., 2012](#)) and TRILEX ([Aryal and Parcollet, 2015, 2016b](#)).

(iii) The third class consists of all diagrams where all four external lines enter at different bare vertices, see Fig. [7](#)(c). Their contribution to F depends on *all three* frequencies (as illustrated by the orange circle for the ν' dependence) and hence decay in *all* directions of frequency space. This is important for many-body algorithms based on local DMFT vertex functions, because diagrams of this type need to be considered for small frequencies only ([Wentzell et al., 2016](#)).

As diagrams of type (i) and (ii) in Fig. [7](#)(a) and (b) are two-particle reducible, all diagrams of the 2PI vertex Λ belong to class (iii). Hence, $\Lambda^{\nu\nu'\omega}$ decays in all three directions of frequency space except for a constant background U , cf. Fig. [8](#) (right). In other words, the asymptotic behavior of F originates from reducible diagrams only. Consequently, when considering 2PI diagrams in one channel (Γ_r), one “loses” all the asymptotic structures generated by the two-particle reducible diagrams in this channel, keeping only the high-frequency features from the reducible diagrams in the complementary channels (cf. Sec. [II.A](#)). This is nicely illustrated by comparing the DMFT data for F and Γ_c in Fig. [8](#) (upper panels), where the disappearance of the ph $\omega = 0$ structure corresponds to the vanishing background.

The simplification of the high-frequency asymptotics is a helpful factor in the numerical manipulation of the 2PI vertex functions. We should, however, note that at the same time the low-frequency structure of the (2PI) vertices can become very complicated—in certain parameter regimes. Specifically, as reported in recent DMFT

³ Precisely, the fermion-boson vertices are obtained by eliminating all internal susceptibilities, i.e., all internal subdiagrams of type (i), i.e., dividing these diagrams by $1 - U\chi^\omega$ ([Rohringer and Toschi, 2016](#)).

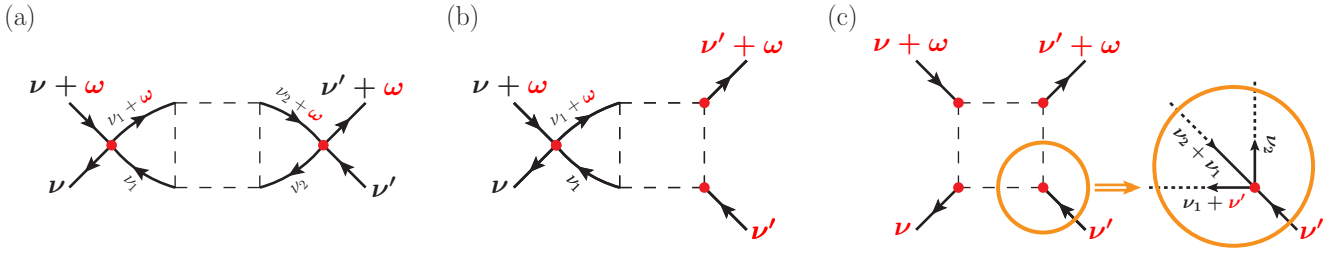


Figure 7 (Color online) Categorization of diagrams according to their frequency dependence. (a) Diagram where the left and right pairs of external lines are attached to the same two bare interaction vertices; (b) Diagram where only the left external lines are connected to the same bare vertex; (c) Diagram where all external lines enter at different bare vertices. The external frequencies, on which the diagram depends explicitly are marked in red.

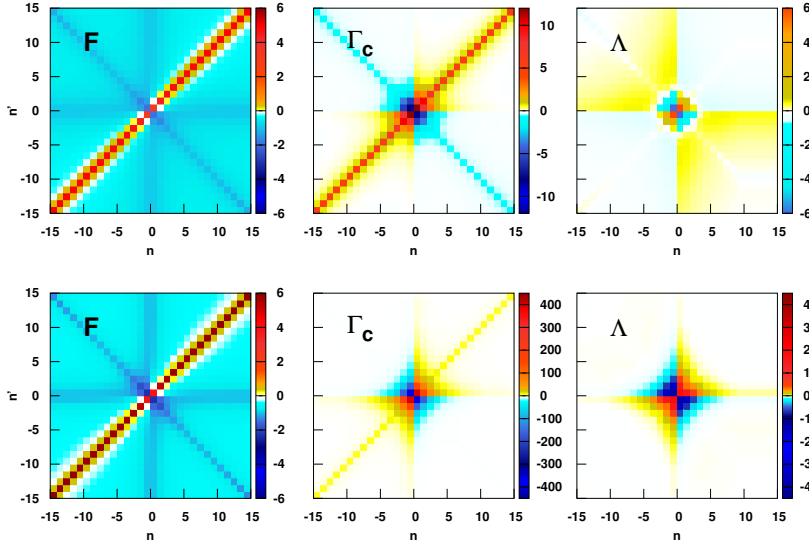


Figure 8 (Color online) DMFT results for the full local vertex ($F_c^{\nu\nu'(\omega=0)}-U$; left), the 2PI vertex in the ph charge channel ($\Gamma_c^{\nu\nu'(\omega=0)}-U$; middle), and the fully 2PI vertex ($\Lambda_c^{\nu\nu'(\omega=0)}-U$; right) at Matsubara frequencies $\nu^{(l)} = (2n^{(l)} + 1)\pi/\beta$. The calculations have been performed for the Hubbard model on a square lattice with nearest-neighbor hopping t at $T = 0.4t$, $U = 4.8t$ (lower panel) and $U = 5.08t$ (upper panel). The intensity (color bar) is given in units of $4t$. Adapted from Schäfer *et al.*, 2016a.

(and DCA) studies at the two-particle level (Gunnarsson *et al.*, 2016; Janiš and Pokorný, 2014; Ribic *et al.*, 2016b; Schäfer *et al.*, 2016a, 2013), Γ_c and Λ acquire strong low-frequency dependencies, and even become *divergent* in certain cases. This can be seen in the DMFT results of Fig. 8 (lower panel), computed for a U just before the divergence (note the large values for Γ_c and Λ in the color scale). Multiple divergence lines for Γ_c and Λ have been numerically observed in the DMFT phase-diagram of the Hubbard- and Falicov-Kimball models, also at moderate interactions. While the frequency-dependent structures of the full vertex F is now well understood, the physical and algorithmic implications of the multiple divergences of the 2PI vertex are not fully clarified yet, and are subject to an ongoing discussion and research (Gunnarsson *et al.*, 2016; Kozik *et al.*, 2015; Schäfer *et al.*, 2016a; Stan *et al.*, 2015).

D. Calculation of the local vertex

In recent years, we have witnessed a staggering increase in applications of two-particle Green's functions and a

correspondingly rapid development of efficient algorithms to compute them. To large extent this has been driven by the development of diagrammatic extensions of DMFT, as well as increased computational resources. Here we provide a summary of the different numerical methods for calculating the local vertex and related response functions and provide references for further reading.

The static ($\omega = 0$) component of the vertex has already been calculated in the early days of DMFT for obtaining susceptibilities (Jarrell, 1992). Pioneering attempts to compute the dynamical and momentum structure of a two-particle vertex were made by Tahvildar-Zadeh *et al.*, 1997 and Maier *et al.*, 2006 using quantum Monte Carlo methods. Kusunose, 2006 computed generalized susceptibilities using second-order iterated perturbation theory (IPT). More recently the vertex has also been obtained within functional renormalization group calculations (Kinza and Honerkamp, 2013). The most frequently used methods to calculate the vertex however are exact diagonalization (ED) and quantum Monte Carlo (QMC) based implementations, including the Hirsch-Fye and continuous-time (CTQMC) variants. These methods allow to control the error. We discuss them in the following

with a focus on the developments regarding the calculation of the two-particle vertex. A detailed review of CTQMC methods is beyond the scope of this article. We refer to the comprehensive review of [Gull *et al.*, 2011a](#). Open source implementations are publicly available for most methods nowadays. We provide an overview in [Sec. V](#).

Impurity solvers typically evaluate the two-particle Green's function, from which vertex functions are extracted as described in [Sec. II.A](#). Their generalization to n -particle correlation functions is, in principle, straightforward. Their computation however quickly exhausts available computation time and memory resources. While the Green's functions can be measured as a function of imaginary time, they are usually evaluated on Matsubara frequencies. The number of required sampling points in time scales as $\sim (\beta U)^3$, so that the storage size would often be impractical. In addition, the treatment of the various discontinuities arising from the anticommutation relations of the fermionic operators is cumbersome.

1. Exact Diagonalization (ED)

In ED, the two-particle Green's function (1) can be computed with a relatively simple algorithmic extension of the standard ED implementation used in the context of DMFT ([Georges *et al.*, 1996](#)). It is most conveniently evaluated by applying the Fourier transform (4) (from imaginary time to Matsubara frequencies) to the Lehmann representation ([Abrikosov *et al.*, 1975](#); [Mahan, 2000](#)). The two-particle Green's function can then be written as a sum over products of the matrix elements of the four creation and annihilation operators. The sums in the terms are weighted with a function that depends on the eigenvalues and the three external Matsubara frequencies, see appendices of [Toschi *et al.*, 2007](#) and [Hafermann *et al.*, 2009b](#). Because of the exponential increase of the Hilbert space and the required four-fold nested sum over the eigenstates, ED is essentially limited to single-orbital calculations and a maximal number of 5 sites (4 bath + 1 impurity site). Calculations can be sped up through parallelization, by using a lookup table for the exponential factors $\exp(-\beta E_i)$, by truncating the sums for terms in which the exponentials are negligible, and most importantly, by exploiting symmetries. The Lanczos algorithm ([Georges *et al.*, 1996](#)), which simplifies the calculation of the single-particle Green's function, cannot directly be applied to the two-particle Green's function. The reason is that transitions between two nearby states at arbitrarily high energies contribute; this might be circumvented, however, using the correction vector method ([Tanaka, 2016](#)).

2. Quantum Monte Carlo (QMC)

a. Hirsch-Fye and CT-AUX While ED and CTQMC are more commonly used nowadays, the Hirsch-Fye QMC algorithm ([Hirsch and Fye, 1986](#)) remains an efficient method to evaluate n -particle Green's functions. Here, observables are intrinsically affected by the Trotter decomposition error. Nevertheless, even the numerically delicate (diverging) 2PI vertex Λ can be extracted with sufficient accuracy in physically relevant parameter regimes of the single band Hubbard model in DMFT and DCA calculations ([Gunnarsson *et al.*, 2016](#); [Maier *et al.*, 2006](#)). In addition, working on a discrete-time grid avoids dealing with equal-time discontinuities which can arise in modern continuous-time algorithms.

At low temperatures, when controlling the Trotter error becomes impractical, a CTQMC algorithm may offer superior performance. For instance, the continuous-time auxiliary field (CT-AUX) algorithm ([Gull *et al.*, 2008](#)) is based on an auxiliary-field decoupling of the interaction vertices similar to the Hirsch-Fye algorithm, but samples a varying number of fields at arbitrary times. CT-AUX is particularly efficient for large cluster problems. The Fourier transform of the Green's function measurement to Matsubara frequencies can be sped up significantly using a non-equidistant fast Fourier transform (NFFT) algorithm ([Staar *et al.*, 2012](#)) when the perturbation order is sufficiently large ($\gtrsim 20$). This applies to other continuous-time methods as well.

b. CT-INT In the continuous-time expansion in the interaction (CT-INT), the measurement of 2-particle Green's functions amounts to performing a Monte Carlo average over ratios of determinants which differ by two rows and columns ([Gull *et al.*, 2011b](#); [Rubtsov *et al.*, 2005](#)) (instead on one for the single-particle function). Similar to Hirsch-Fye QMC and CT-AUX, the measurement for a particular correlation function can symbolically be obtained by enumerating all Wick contractions of the operators appearing in the definition of the correlation function and replacing them by configuration-dependent quantities $G_{\tau_1, \dots, \tau_N}(\tau, \tau')^{\sigma\sigma'}$. Here N denotes the CT-INT perturbation order, and τ_1, \dots, τ_N the continuous QMC times. The Wick contraction yields:

$$\begin{aligned} \langle T_\tau c_\sigma(\tau_1) c_\sigma^\dagger(\tau_2) c_{\sigma'}(\tau_3) c_{\sigma'}^\dagger(0) \rangle \rightarrow & \quad (19) \\ G_{\tau_1, \dots, \tau_N}^{\sigma\sigma}(\tau_1, \tau_2) G_{\tau_1, \dots, \tau_N}^{\sigma'\sigma'}(\tau_3, 0) & \\ - \delta_{\sigma\sigma'} G_{\tau_1, \dots, \tau_N}^{\sigma\sigma}(\tau_1, 0) G_{\tau_1, \dots, \tau_N}^{\sigma\sigma}(\tau_3, \tau_2). & \end{aligned}$$

By Fourier transform a measurement directly in frequency is straightforwardly obtained. The latter can be factorized into $G_{\tau_1, \dots, \tau_N}(\nu, \nu')^{\sigma\sigma'}$ factors to speed up the calculation. With N , N_ν , N_ω denoting the perturbation order, the number of fermionic and bosonic frequencies, respectively, the measurement scales as $\mathcal{O}(N^2 N_\nu^2) +$

$\mathcal{O}(N_\nu^2 N_\omega)$.

c. CT-HYB In the case of CTQMC with hybridization expansion (CT-HYB) (Werner *et al.*, 2006; Werner and Millis, 2006), the partition function is expanded in terms of the AIM hybridization function. Here, the Monte Carlo weight is a product of the determinant of hybridization functions and a trace over the atomic states. In the original implementation, the self-energies and vertex functions exhibit relatively large fluctuations at intermediate to high frequencies (Gull *et al.*, 2007; Hafermann *et al.*, 2012). This problem can be cured by expressing the self-energy as a ratio of two correlation functions G and F (improved estimator), a relation which follows from the equation of motion and corresponds to $F = \Sigma G$. This trick was first introduced in the numerical renormalization group (NRG) context (Bulla *et al.*, 2008, 1998). Improved estimators exist for the reducible vertex function as well (Hafermann *et al.*, 2012), including impurity models with spin-boson coupling (Otsuki, 2013), retarded interactions (Hafermann, 2014) and multi-orbital beyond density-density interactions (Gunacker *et al.*, 2016). Note also that in CT-HYB, the conventional approach to obtain the Green's function and vertex is "removing" hybridization lines. This procedure does not allow us to calculate all components of the multi-orbital vertex function, a limitation that was overcome by Gunacker *et al.*, 2015 using worm sampling.

3. Handling vertex asymptotics

A generic problem of the numerical treatment of vertex functions is the huge memory size required to store the three-frequency-dependent vertex. This limits the size of the frequency box where the vertex can be treated exactly. However, similar to single-particle quantities, the vertex approaches an asymptotic behavior at high frequencies. This behavior can be characterized by diagrams similar to the ones discussed in Sec. II.C and exploited to simplify calculations.

A pioneering work in this direction is Kuneš, 2011 who, for calculating the DMFT susceptibility more accurately, expressed the high frequency asymptotic behavior of the $\omega = 0$ vertex function irreducible in the particle-hole channel in terms of the local dynamical susceptibility. Starting from the diagrammatic considerations of Rohringer *et al.*, 2012, Li *et al.*, 2016 and Wentzell *et al.*, 2016 derived more general relations for the asymptotics of the three-frequency vertex based on the parquet equations, and proposed a parameterization scheme of the full high-frequency behavior of vertex functions based on a diagrammatic analysis. Kaufmann *et al.*, 2017 implemented the measurement of these asymptotics in CT-HYB. The asymptotic behavior of the vertex depends on

two frequencies and allows the calculation of the vertex in an arbitrarily large frequency box with reduced statistical noise, while taking a fraction of the numerical effort and storage required for the full three frequency dependent vertex. The latter however is still needed at low frequencies, where the vertex deviates from this asymptotics.

Alternatively, correlation functions can be represented in a Legendre polynomial basis (Boehnke *et al.*, 2011) to obtain a compact representation. For vertex functions it is advantageous to use a mixed representation where the bosonic frequency dependence is kept whereas the fermionic ones are projected onto the Legendre polynomial basis. Provided a sufficiently large cutoff N_l of polynomial coefficients, the Legendre representation allows the calculation of the vertex at arbitrarily high frequencies. The measurement scales as $\mathcal{O}(N^2 N_l^2 N_\omega)$. Shinaoka *et al.*, 2017b introduced an intermediate representation between the imaginary-time and real-frequency domains. It is based on sparse modeling of data in a basis that is derived from the singular value decomposition of the kernel relating the data in these domains (Otsuki *et al.*, 2017). Interestingly, it includes the Legendre representation as the high-temperature limit, but requires even less coefficients N_l , in particular at low temperatures. As for the Legendre basis, the transformation is unitary, so that the entire calculation can in principle be performed in this basis and only final results need to be transformed back to Matsubara representation.

III. METHODS

After discussing the diagrammatics and physics of the local vertex in the previous section, we are now ready to turn to the recently developed diagrammatic vertex extensions of DMFT (for an overview, see Sec. I.B and Table II in Sec. VI). These have a common underlying principle, which follows two steps:

- A local approximation is performed at the 2P-level, which corresponds to identifying the building block of the specific approach. This (highly non-perturbative!) building block is one of the local vertices discussed in the previous section.
- A diagrammatic approach is built around this local building block to include non-local correlations beyond DMFT into the self-energy and susceptibilities.

Out of this line fall digrammatic extensions of DMFT which simply combine the local DMFT with the non-local self-energy from another approach; such approaches are discussed in Sec. III.F.

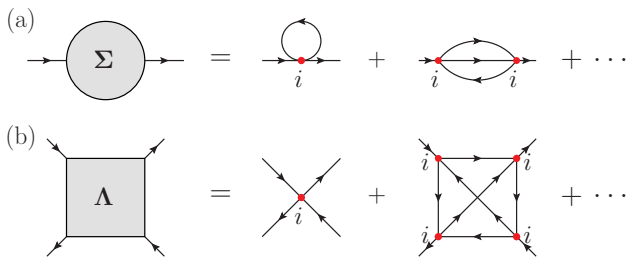


Figure 9 (Color online) (a) In DMFT the fully 1PI one-particle vertex, i.e., the self-energy Σ , is purely local. (b) In DGA instead the fully 2PI two-particle vertex Λ is approximated to be local (lines: interacting Green's function; dots: bare Hubbard interaction U ; i represents a site index of the lattice).

A. Dynamical vertex approximation (DGA)

The best way to understand the basic concepts of the dynamical vertex approximation (DGA) is to start by considering the diagrammatics of DMFT: DMFT assumes the *locality* of all (skeleton) diagrams for the self-energy, see Fig. 9 (a). The self-energy, however, is nothing but the one-particle (irreducible) vertex. Hence, a systematic generalization of DMFT is directly obtained by requiring the locality at the n -particle level: [Toschi et al., 2007](#) assume the fully n -particle irreducible (n PI) n -particle vertex to be *local*. Differently from DMFT, the self-energy or other vertices with less than n particles do acquire non-local contributions, as does the full n -particle vertex entering the susceptibility or generally the k PI n -particle vertex for $k < n$.

Taking the limit $n \rightarrow \infty$ (and a proper generalization of 2PI defined in Sec. II.A to n PI) corresponds to consider *all* diagrams for the Hubbard model or any other model with a local interaction. Therefore the exact solution is recovered for $n \rightarrow \infty$. In practice one is however restricted to DGA on the $n = 2$ particle level which is illustrated in Fig. 9 (b). This assumes the fully 2PI *two*-particle vertex Λ to be *local* (for the definitions see Sec. II.A).

Why a local Λ ? Assuming that a *local* Λ is a good approximation can be understood, first of all, from a Feynman diagrammatic perspective: The fully irreducible diagrams are topologically very compact, and hence the most local ones. Each Λ diagram generates many diagrams for the full vertex F . For example, the bare (local) interaction U (as part of Λ) generates via the parquet equations all Feynman diagrams of up to 3rd order in U as well as many higher order diagrams. The locality of Λ is also supported by numerical data in $d = 2$: Even in the parameter regions with strong non-local correlations in the self-energy Σ and the full vertex F , Λ is still local to a very good approximation in DCA ([Maier et al.,](#)

2006).

From a physical perspective, this numerical evidence of a purely local Λ can be attributed to the absence of any ladder diagrams, which are typically associated with collective (SDW, CDW, etc.) modes of the system. As these modes are responsible for strong non-local correlations, the momentum-dependence of Λ can be (and often is) particularly weak, consistent with the DGA assumption, even in situations where F is strongly momentum dependent.

Our understanding of non-local physics is also often based on ladder diagrams in terms of the bare U , e.g. the magnon self-energy ([Hertz and Edwards, 1973](#)), see Fig. 1. Hitherto, however, such approaches were restricted to weak coupling ([Vilk and Tremblay, 1997](#)). Taking a local Λ instead of U in DGA includes all the strong local DMFT correlations (quasiparticle renormalizations, Mott transitions etc.), but at the same time allows us to study non-local correlations and collective excitations over all length scales.

1. Parquet DGA

The locality assumption for Λ is the first step in the construction of the DGA. The second step, is to define the diagrams to be constructed from this local building block. For the DGA, this second step is naturally the application of the parquet equations ([Held, 2014; Toschi et al., 2007](#)), see Fig. 6 in Sec. II.A, which allow the calculation of the full vertex F , self-energy Σ etc. from Λ .

The algorithmic implementation of DGA is realized through the following steps, see Fig. 10 (left), which we will illustrate here by a comparison with the more common DMFT algorithm in Fig. 10 (middle): (i) First, we solve an AIM. In contrast to DMFT, where only the one-particle Green's function of the AIM is calculated, in DGA also the two-particle-Green's function of the AIM needs to be computed. (ii) Second, we extract from the AIM the irreducible building block of our theory. In DGA, this requires to invert the parquet equations of the AIM to compute the fully 2PI local vertex, i.e., the three frequency dependent $\Lambda^{\nu\nu'\omega}$. In DMFT this corresponds to calculating the AIM's local self-energy. (iii) Third, as mentioned above, in DGA we use the $\Lambda^{\nu\nu'\omega}$ of the AIM as input for the parquet equation (8) of the finite- d lattice system under consideration. The self-consistent solution of this equation together with the BSEs (10) and the Schwinger-Dyson Eq. (11) yields the *momentum*-dependent self-energy and correlation functions of the DGA. This step corresponds in DMFT to calculating the Green's function, through the lattice Dyson equation with the local DMFT self-energy as an input. (iv) Finally, if the local DGA Green's function differs from the input local Green's function, the initial AIM is accord-

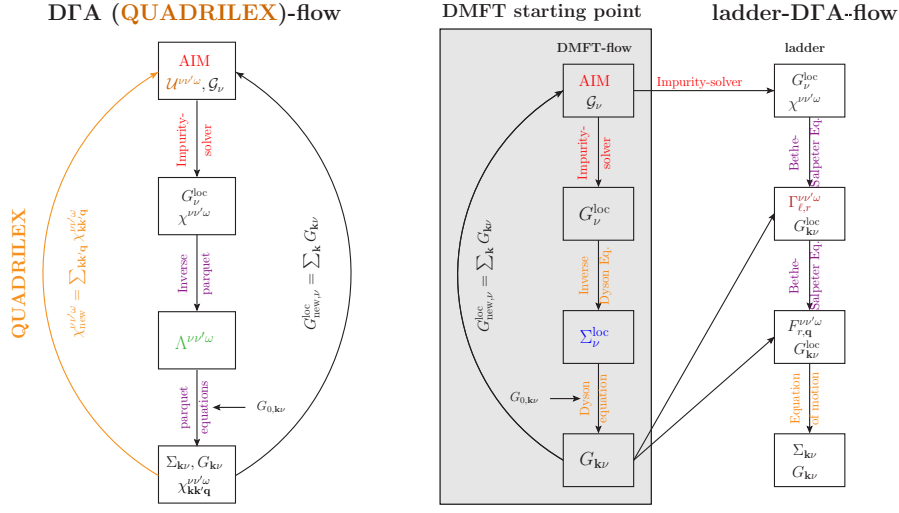


Figure 10 (Color online) Flow diagram for parquet DGA with or without the QUADRILEX self-consistency for the interaction (left), DMFT (middle), and ladder DGA (right).

ingly updated (yielding a new Λ). Steps (i) to (iv) are repeated until self-consistency, analogous to the DMFT self-consistency on the one-particle level.

The richer physical content of DGA is paid for by a higher numerical effort compared to DMFT. This applies in particular to steps (i) the calculation of the local vertex and (iii) solving the parquet plus BSE equations. For (i), one needs to perform an accurate numerical calculation of the two-particle Green’s function of the AIM with its full dependence on three frequencies (cf. Sec. II.D), whereas in the DMFT loop only the one-particle Green’s function is required. For (iii), we recall that a numerical solution of the parquet equations for lattice systems is highly demanding. Cutting-edge parquet algorithms have been developed (Li *et al.*, 2016; Tam *et al.*, 2013; Yang *et al.*, 2009) and first DGA parquet calculations have been presented for a benzene ring (Valli *et al.*, 2015b) and the 2D Hubbard model (Li *et al.*, 2016).

2. Ladder DGA

A full parquet solution of the DGA equations is still not feasible (i) in the proximity of (quantum) phase transitions which requires a fine \mathbf{k} grid or (ii) for *ab-initio* DGA (Galler *et al.*, 2017; Toschi *et al.*, 2011) calculations which require more orbitals. Hence, simplifications of the DGA scheme are often needed. Here, we will discuss the most commonly used approximation, the “ladder approximation”, and discuss its physical justification. This route has been followed by Kusunose, 2006, Toschi *et al.*, 2007, and Slezak *et al.*, 2009.

Starting from the parquet DGA [see Eq. (8)], we recall that the momentum dependence of its two-particle reducible terms $\Phi_{r, \ell, \mathbf{k}\mathbf{k}'\mathbf{q}}^{\nu\nu'\omega}$ is crucial for describing second-order phase transitions, e.g., (anti)ferromagnetism ($r = s$)

and charge density waves ($r = c$) in the particle-hole sector ($\ell = ph$ or \overline{ph}), or singlet ($r = \uparrow\downarrow$) superconductivity ($\ell = pp$). The proximity of such an instability is indicated by a strong enhancement of the momentum-dependent $\Phi_{\ell, r, \mathbf{k}\mathbf{k}'\mathbf{q}}^{\nu\nu'\omega}$ in the corresponding scattering channel(s) defined by ℓ and r . Hence, in all situations where the leading instability of the system is known *a priori*, one can consider a momentum-dependent $\Phi_{\ell, r, \mathbf{k}\mathbf{k}'\mathbf{q}}^{\nu\nu'\omega}$ *only* in the relevant channel, keeping in the other channels the local $\Phi_{\ell, r}$ ’s of DMFT only. This approximation reduces the parquet equations to the BSE and hence represents a “ladder approximation” of DGA.

In the following, we explicitly recapitulate the ladder-DGA equations (Rohringer, 2013; Toschi *et al.*, 2007) for one of the most relevant situations: If magnetic fluctuations dominate, we can restrict ourselves to the two ph -channels $\ell = ph, \overline{ph}$.⁴ This is also the implementation that has been employed in most DGA calculations hitherto (see Sec. IV); Kusunose, 2006 considered the $\ell = ph$ channel only.

As discussed above, by applying the ladder approximation to the two ph channels, i.e., ph and \overline{ph} , we assume both Λ and Φ_{pp} in Eq. (8) to be purely local. Hence, the expression for the full vertex entering in the equation of motion [Eq. (11)] for the DGA self-energy, reads

$$F_{\uparrow\downarrow, \mathbf{k}\mathbf{k}'\mathbf{q}}^{\nu\nu'\omega} = \Lambda_{\uparrow\downarrow}^{\nu\nu'\omega} + \Phi_{ph, \uparrow\downarrow, \mathbf{k}\mathbf{k}'\mathbf{q}}^{\nu\nu'\omega} + \Phi_{\overline{ph}, \uparrow\downarrow, \mathbf{k}\mathbf{k}'\mathbf{q}}^{\nu\nu'\omega} + \Phi_{pp, \uparrow\downarrow}^{\nu\nu'\omega}. \quad (20)$$

While the momentum dependence of Φ_{pp} has been neglected, it still needs to be calculated for Φ_{ph} and $\Phi_{\overline{ph}}$.

⁴ In principle, we could restrict ourselves also to the spin-sector $r = s$ neglecting non-local charge fluctuations $r = c$. However, such a simplification would break the crossing and SU(2) symmetry and, hence, we consider $r = c$ on the same footing as $r = s$.

This is possible through the BSE (10). Within a full parquet approach the corresponding irreducible vertices $\Gamma_{ph,r}$ and $\Gamma_{\bar{p}\bar{h},r}$ would be momentum dependent through mutual screening between the channels. In our ladder DGA approximation we do not consider such renormalization effects and, hence, assume $\Gamma_{ph,r}$ and $\Gamma_{\bar{p}\bar{h},r}$ to be purely local:

$$\begin{aligned} F_{\text{lad},r,\mathbf{q}}^{\nu\nu'\omega} &= \Gamma_r^{\nu\nu'\omega} + \Phi_{r,\mathbf{q}}^{\nu\nu'\omega} \\ &= \Gamma_{ph,r}^{\nu\nu'\omega} + \sum_{\bar{\mathbf{k}}\bar{\nu}} \Gamma_{ph,r}^{\nu\bar{\nu}\omega} G_{\bar{\mathbf{k}}\nu_1}^{\text{loc}} G_{(\bar{\mathbf{k}}+\mathbf{q})(\bar{\nu}+\omega)}^{\text{loc}} F_{\text{lad},r,\mathbf{q}}^{\bar{\nu}\nu'\omega}, \end{aligned} \quad (21)$$

where $r = c, s$ and $G_{\mathbf{k}\nu}^{\text{loc}} = [G_{0,\mathbf{k}\nu}^{-1} - \Sigma_{\nu}^{\text{loc}}]^{-1}$ is the DMFT Green's function of Eq. (14). An analogous equation holds for the $\bar{p}\bar{h}$ channel which is exactly equivalent to Eq. (21) for $r = s$ due to SU(2) and crossing symmetry, see Table I.

Eq. (21) is a great algorithmic simplification w.r.t. to a full parquet treatment because $F_{\text{lad},r,\mathbf{q}}^{\nu\nu'\omega}$ depends on the transferred momentum \mathbf{q} only, rather than on all three momenta in the parquet equation. Combining Eqs. (20) and (21), the final expression for the full vertex reads

$$\begin{aligned} F_{\uparrow\downarrow,\mathbf{k}\mathbf{k}'\mathbf{q}}^{\nu\nu'\omega} &= \frac{1}{2} \left(F_{\text{lad},c,\mathbf{q}}^{\nu\nu'\omega} - F_{\text{lad},s,\mathbf{q}}^{\nu\nu'\omega} \right) - F_{\text{lad},s,\mathbf{k}'-\mathbf{k}}^{\nu(\nu+\omega)(\nu'-\nu)} + \\ &\quad - \frac{1}{2} \left(F_c^{\nu\nu'\omega} - F_s^{\nu\nu'\omega} \right). \end{aligned} \quad (22)$$

Here the last, purely local terms provide a double counting corrections of local contributions (Rohringer, 2013; Toschi *et al.*, 2007). Inserting Eq. (22) for $F_{\uparrow\downarrow,\mathbf{k}\mathbf{k}'\mathbf{q}}^{\nu\nu'\omega}$ in the Schwinger-Dyson Eq. (11), we finally obtain the explicit expression for the ladder DGA self-energy:

$$\begin{aligned} \Sigma_{\mathbf{k}\nu} &= \frac{Un}{2} - U \sum_{\nu'\omega} \sum_{\mathbf{k}'\mathbf{q}} F_{\uparrow\downarrow,\mathbf{k}\mathbf{k}'\mathbf{q}}^{\nu\nu'\omega} \times \\ &\quad \times G_{\mathbf{k}'\nu'}^{\text{loc}} G_{(\mathbf{k}'+\mathbf{q})(\nu'+\omega)}^{\text{loc}} G_{(\mathbf{k}+\mathbf{q})(\nu+\omega)}^{\text{loc}}. \end{aligned} \quad (23)$$

The practical implementation of Eqs. (20)-(23) is illustrated by the flow diagram Fig. 10 (right), cf. Held *et al.*, 2008. The calculation steps are the following: (i) A complete DMFT self-consistency cycle is performed as outlined in Fig. 10 (middle). (ii) After DMFT convergence the local one- and two-particle Green's functions of the AIM are computed. (iii) The irreducible local vertices in the channel(s) under consideration, $\Gamma_{\ell,r}^{\nu\nu'\omega}$, are computed via the inversion of BSEs for the AIM. (iv) The irreducible local irreducible vertex functions $\Gamma_{\ell,r}^{\nu\nu'\omega}$ and the (momentum-dependent) DMFT Green's function $G_{\mathbf{k}\nu}^{\text{loc}}$ serve as an input for the lattice BSEs which, in turn, yield the ladder vertex $F_{\text{lad},r,\mathbf{q}}^{\nu\nu'\omega}$ and the full F via Eq. (22). (v) The self-energy is derived from the DMFT Green's function $G_{\mathbf{k}\nu}^{\text{loc}}$ and the vertex $F_{\text{lad},r,\mathbf{q}}^{\nu\nu'\omega}$ by means of the equation of motion, (23).

Moriyaesque λ correction The ladder DGA algorithm described above enormously reduces the numerical effort

w.r.t. the full parquet implementation. However, ladder DGA leads to violations of several sum rules for the susceptibilities which are obtained from the BSE (20), since mutual screening effects between different scattering channels are not taken into account. One example of such sum rule, which is not fulfilled within ladder DGA, is related to the total density of the system and reads:

$$\begin{aligned} \sum_{\omega\mathbf{q}} \chi_{\uparrow\uparrow,\mathbf{q}}^{\omega} &= \sum_{\omega\mathbf{q}} \frac{1}{2} (\chi_{c,\mathbf{q}}^{\omega} + \chi_{s,\mathbf{q}}^{\omega}) = \\ &= \langle n_{\uparrow} n_{\uparrow} \rangle - \langle n_{\uparrow} \rangle \langle n_{\uparrow} \rangle = \frac{n}{2} \left(1 - \frac{n}{2} \right). \end{aligned} \quad (24)$$

This relation guarantees automatically the correct $(1/\nu)$ high-frequency asymptotics of the self-energy in any scheme based on the equation of motion (11). A corresponding violation of Eq. (24) hence leads to an incorrect asymptotic behavior which can be indeed observed in ladder DGA (Katanin *et al.*, 2009; Toschi *et al.*, 2007).

To overcome this problem the ladder DGA susceptibilities obtained from Eq. (20) are supplemented by means of a Moriyasque λ correction. Considering the Ornstein-Zernike form of charge- and spin-modes at momentum \mathbf{Q}_r

$$\chi_{r,\mathbf{q}}^{\omega=0} = \frac{A}{(\mathbf{q} - \mathbf{Q}_r)^2 + \xi_r^{-2}}, \quad (25)$$

and following the Moriya theory of itinerant magnetism (Moriya, 1985) it is natural to apply a correction to $\chi_{r,\mathbf{q}}^{\omega}$ by modifying the correlations length ξ_r (i.e., the mass) of the propagator. This is consistent with the well-know fact that a mean-field theory such as DMFT overestimates the correlation length of the system. It accounts for non-local contributions to the particle-hole-irreducible vertices.

Since within the ladder DGA scheme the propagator $\chi_{r,\mathbf{q}}^{\omega}$ (without any correction and self consistency) corresponds exactly to the DMFT one, it is reasonable to reduce this overrated DMFT correlation length of the mode r , fixing it to a value such that condition (24) is fulfilled. In practice this is done by applying the transformation

$$(\chi_{r,\mathbf{q}}^{\omega})^{-1} \rightarrow (\chi_{r,\mathbf{q}}^{\omega})^{-1} + \lambda_r = (\chi_{r,\mathbf{q}}^{\lambda,\omega})^{-1}. \quad (26)$$

Rewriting the ladder DGA equation of motion in such a way that it explicitly contains the physical susceptibility and inserting the λ -corrected susceptibilities $\chi_{r,\mathbf{q}}^{\lambda,\omega}$ into it leads to the λ -corrected self-energy, see Katanin *et al.*, 2009 and Rohringer and Toschi, 2016. The relation of this procedure to the dual boson approach is discussed in Sec. III.G.2.

3. *Ab initio* DGA for materials calculations

Hitherto, we have considered a single-orbital and a local interaction U in the DGA approach. An exten-

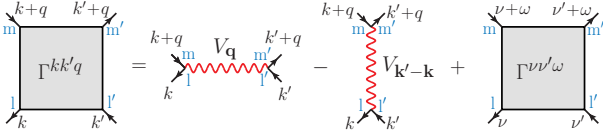


Figure 11 (Color online) In AbinitioDFA the irreducible vertex Γ in the particle-hole and transversal particle-hole channel is approximated by the bare *non-local* Coulomb interaction V^q and the *local* vertex Γ_{loc} which depends on orbitals ($l, m \dots$) and frequencies (ν, ν', ω) but not momenta (k, k', q) and includes the local Coulomb interaction U .

sion to non-local interactions and multiple orbitals has been developed and implemented by [Galler *et al.*, 2017](#), building upon earlier ideas put forward by [Toschi *et al.*, 2011](#). Because this way also *ab initio* material calculations are possible and have been performed for SrVO_3 , this variant is coined AbinitioDFA. As a full parquet DFA for multiple orbitals is beyond of what is feasible with present-day computational resources, the key quantity in AbinitioDFA is the irreducible vertex Γ in the particle-hole (and transversal particle-hole) channel just as in ladder DFA.

The key assumption of AbinitioDFA is to approximate Γ by the corresponding local vertex plus the non-local Coulomb interaction V^q , see Fig. 11:

$$\Gamma_{ph,\sigma\sigma',lmm'l'}^{kk'q} \equiv \Gamma_{ph,\sigma\sigma',lmm'l'}^{\nu\nu'\omega} + V_{\sigma\sigma',lmm'l'}^q - \delta_{\sigma\sigma'} V_{\sigma\sigma',mm'l'l'}^{\mathbf{k}'-\mathbf{k}}. \quad (27)$$

Here, l, m, m', l' denote the orbital indices; and $\Gamma_{ph,\sigma\sigma',lmm'l'}^{\nu\nu'\omega}$ includes the local bare interaction U plus all purely local vertex corrections. In calculations with strongly and weakly correlated, say d and p orbitals, one can also approximate the local vertex of the p orbital by U which allows calculations for more orbitals since the calculation of the local vertex remains a large numerical effort; or take the screening of an outer window of orbitals into account, which translates into an additional frequency dependence for U and $V_{\sigma\sigma',lmm'l'}^q$.

As in ladder DFA [Eqs. (21) and (20)], the full vertex is constructed from the vertex (27) using the BSE in the particle-hole and transversal particle-hole channel, with a reformulation in terms of F instead of Γ to avoid numerical obstacles associated with the divergences in Γ discussed in Sec. II.C.

The multi-orbital extension ([Galler *et al.*, 2017](#)) of the Schwinger Dyson Eq. (23) is employed to obtain Σ from the calculated F , following the ladder DFA scheme. This Schwinger Dyson Eq. has various U and V^q terms and is not restricted any longer to the $\uparrow\downarrow$ -spin combination of F .

What is still neglected in AbinitioDFA are non-local irreducible vertex corrections. But since from $\Gamma^{kk'q}$ in Eq. (27) the particle-hole ladder and the transversal particle-hole ladder diagrams are constructed, we still

retrieve a lot of correlations originating from V^q : (i) Inserting the V^q term of Fig. 11 and Eq. (27) into the particle-hole BSE ladder yields the RPA screening, and from this screened F the Schwinger Dyson eq. of motion assembles the GW self-energy. (ii) From the local $\Gamma^{\nu\nu'\omega}$ and local Green's function in the subsequent equations, the DMFT self-energy is recovered. Hence, AbinitioDFA is a unifying framework which naturally generate all GW diagrams and all DMFT diagrams. (iii) Beyond GW +DMFT, further non-local correlations are included: the non-local spin fluctuations of ladder DFA, the transversal particle-hole ladder in terms of V^q and mixed terms.

4. QUADRILEX: a functional integral perspective

The quadruply irreducible local expansion scheme (QUADRILEX) by [Aryal and Parcollet, 2016a](#) is closely related to the DFA. It is essentially an extension of DFA in two respects: (i) it provides the framework of a functional integral formalism and (ii) from this functional an additional self-consistency for the two particle vertex. This self-consistency enters in addition to the one for the one-particle Green's function considered in DFA before, see Fig. 10. As DFA, QUADRILEX is based on the 2PI vertex and builds Feynman diagrams around it.⁵

For constructing a functional integral, [Aryal and Parcollet, 2016a](#) employ an idea by [De Dominicis and Martin, 1964b](#): The standard [Baym and Kadanoff, 1961](#) functional depends on the interacting one-particle Green's function G and the bare interaction U . [De Dominicis and Martin, 1964b](#) proposed a Legendre transformation to a functional that depends on G and the two-particle Green's function $G^{(2)}$ instead. As a nontrivial term it contains the set of all 2PI energy diagrams: $\mathcal{K}_4[G, G^{(2)}]$ ([Aryal and Parcollet, 2016a](#); coined \mathcal{K}_2 in [De Dominicis and Martin, 1964b](#)). In the QUADRILEX formalism, [Aryal and Parcollet, 2016a](#) approximate this functional by its local counterpart

$$\mathcal{K}_4[G_{\mathbf{k}\nu}, G_{\sigma\sigma'}^{(2),\nu\nu'\omega}] \approx \mathcal{K}_4[G_{\nu}^{\text{loc}}, G_{\sigma\sigma'}^{(2),\nu\nu'\omega}]. \quad (28)$$

This naturally extends the DMFT, which corresponds to a Kadanoff-Baym functional that depends on G_{ν}^{loc} only, see [Janiš and Vollhardt, 1992](#). The 2PI vertex Λ can be obtained from the functional derivative of \mathcal{K}_4 w.r.t. $G^{(2)}$: $\Lambda = U - 2\delta\mathcal{K}_4/(\delta G^{(2)})$. The approximation $\mathcal{K}_4 = 0$ yields $\Lambda = U$ and generates the parquet approximation. Using the local approximation (28) instead yields –by

⁵ Note that in contrast to the notation of this review [Aryal and Parcollet, 2016a](#) denote this as the four-particle irreducible level since there are four (incoming and outgoing) legs associated to the two-particle (2PI in our notation) vertex—hence the name QUADRILEX.

construction— the same Λ as in DFA, namely all local 2PI diagrams. But the functional formalism also leads to an improved outer self-consistency, which now includes both the one-particle and the two-particle level on an equal footing.

This can be understood as follows: As in DMFT, the approximated functional (28) can be determined by an auxiliary impurity model. In order to match the local part of the lattice $G^{(2)}$ to the corresponding impurity quantity with its full frequency dependence, one has to introduce an adjustable, three-frequency-dependent interaction vertex $\mathcal{U}^{\nu\nu'\omega}$ into the impurity model in addition to the familiar Weiss field \mathcal{G} . $\mathcal{U}^{\nu\nu'\omega}$ allows for including the feedback of collective modes into the impurity model. The DFA can be understood as a special case of QUADRILEX with the additional approximation $\mathcal{U}^{\nu\nu'\omega} \approx U$. For the AIM in the *outer* self-consistency cycle Fig. 10 envisages this additional step in the self-consistency loop. For more details we refer the reader to [Ayril and Parcollet, 2016a](#).

The QUADRILEX scheme has not yet been implemented. Notwithstanding possible convergence issues of the self-consistency cycle or a possible sign problem incurred by the retarded interaction, the implementation might be feasible with today's technology—at least for a single orbital.

B. Dual fermion (DF) theory

It is a common wisdom that models of strongly correlated electrons, such as the Hubbard model, are difficult to treat at large scale and in the thermodynamic limit. The challenge however is not the interaction per se, but the fact that the hopping term and the interaction term are diagonal in different bases, namely in momentum- and lattice-space. In the physically most interesting regimes, both terms are generally of similar order, so that an expansion around the weak- or strong-coupling limit is not applicable. A powerful idea to approach the problem is to *separate* it into nontrivial subproblems that can be treated efficiently and (numerically) exactly and a coupling between them. The splitting is ideally done in a way that this coupling represents a small parameter of the theory, which can be treated perturbatively. The simplest example of such a theory is DMFT (see Sec. II.B). Here the lattice problem is decomposed into a collection of local Anderson impurity models (AIMs). In DMFT the coupling between impurities is neglected. As we will see in the following, DMFT can therefore be viewed as the lowest-order perturbative treatment of the coupling between the local impurity and non-local degrees of freedom of the system. A perturbative treatment of the coupling reintroduces non-local correlations.

From a formal perspective, an action-based formalism provides the most natural basis to achieve the a decou-

pling into local and non-local degrees of freedom. In the following we will discuss this for the Hubbard model, although the concept is more general and can be applied also to other models. See for example [Rubtsov, 2006](#) for an application to ϕ^4 theory and Sec. III.B.2. The action of the Hubbard model (12) is given by

$$\begin{aligned} \mathcal{S}[c^+, c] = & \sum_{\mathbf{k}\nu\sigma} [-i\nu + \varepsilon_{\mathbf{k}} - \mu] c_{\mathbf{k}\nu\sigma}^+ c_{\mathbf{k}\nu\sigma} \\ & + U \sum_i \int_0^\beta d\tau c_{i\uparrow}^+(\tau) c_{i\uparrow}(\tau) c_{i\downarrow}^+(\tau) c_{i\downarrow}(\tau), \end{aligned} \quad (29)$$

where $c_{i\sigma}^{(+)}(\tau)$ and $c_{\mathbf{k}\nu\sigma}^{(+)}$ are the fermionic Grassmann fields corresponding to the annihilation (creation) operators $\hat{c}_{i\sigma}^{(\dagger)}$ and $\hat{c}_{\mathbf{k}\sigma}^{(\dagger)}$, respectively. In the spirit of the above discussion we introduce a local reference action which is diagonal in lattice space:

$$\begin{aligned} \mathcal{S}_{\text{loc}}[c^+, c] = & \sum_{\nu\sigma} [-i\nu + \Delta_\nu - \mu] c_{\nu\sigma}^+ c_{\nu\sigma} \\ & + U \int_0^\beta d\tau c_\uparrow^+(\tau) c_\uparrow(\tau) c_\downarrow^+(\tau) c_\downarrow(\tau). \end{aligned} \quad (30)$$

The Gaussian part Δ_ν of the reference system is frequency- and in general site-dependent, but we limit our presentation to the homogenous case. The rationale behind introducing an AIM as the reference system is that we can compute its one- and two-particle Green's functions numerically exactly as described in Sec. II.D.

Keeping in mind the idea of a separation into solvable parts and a supposedly weak coupling between them, we express the lattice action Eq. (29) in terms of the local reference system Eq. (30) by formally adding and subtracting an arbitrary hybridization function Δ_ν :

$$\mathcal{S}[c^+, c] = \sum_i \mathcal{S}_{\text{loc}}[c_i^+, c_i] + \sum_{\mathbf{k}\nu\sigma} [\varepsilon_{\mathbf{k}} - \Delta_\nu] c_{\mathbf{k}\nu\sigma}^+ c_{\mathbf{k}\nu\sigma}. \quad (31)$$

The generating functional $W[\eta^+, \eta, \tilde{\eta}^+, \tilde{\eta}] = \log Z[\eta^+, \eta, \tilde{\eta}^+, \tilde{\eta}]$ for the action (31) reads:

$$\begin{aligned} Z[\eta^+, \eta, \tilde{\eta}^+, \tilde{\eta}] = & \int D[c^+, c] \exp \left[-\mathcal{S}_{\text{loc}}[c^+, c] \right. \\ & \left. - \sum_{\mathbf{k}\nu\sigma} [\varepsilon_{\mathbf{k}} - \Delta_\nu] C_{\mathbf{k}\nu\sigma}^+ C_{\mathbf{k}\nu\sigma} + \sum_{\mathbf{k}\nu\sigma} c_{\mathbf{k}\nu\sigma}^+ \eta_{\mathbf{k}\nu\sigma} + \eta_{\mathbf{k}\nu\sigma}^+ c_{\mathbf{k}\nu\sigma} \right], \end{aligned} \quad (32)$$

where $C_{\mathbf{k}\nu\sigma}^{(+)} = c_{\mathbf{k}\nu\sigma}^{(+)} + b_{\nu\sigma}^{-1} \tilde{\eta}_{\mathbf{k}\nu\sigma}^{(+)}$ and $\tilde{\eta}_{\mathbf{k}\nu\sigma}^{(+)}$ represent so-called dual source-fields which have been introduced to better reveal the connection between dual and physical fermion correlations functions. The coupling $b_{\nu\sigma}$ denotes a – for the moment arbitrary – function of spin and Matsubara frequencies. The derivatives of the functional (32) with respect to the source fields η^+, η yield the connected physical correlation functions of the system. For example, the single-particle Green's function is obtained as $G = \partial^2 W / \partial \eta^+ \partial \eta |_{\eta^{(+)} = \tilde{\eta}^{(+)} = 0}$.

The central step of the DF derivation is to *decouple* the reference system of impurities which are connected

through the term $\varepsilon_{\mathbf{k}} - \Delta_{\nu}$ by introducing new fields $\tilde{c}^{(+)}$ representing the so-called *dual fermions*. This is achieved through the Hubbard-Stratonovich transformation

$$e^{-[\varepsilon_{\mathbf{k}} - \Delta_{\nu}] C_{\mathbf{k}\nu\sigma}^+ C_{\mathbf{k}\nu\sigma}} = \frac{-1}{\prod_{\mathbf{k}\nu\sigma} b_{\nu\sigma}^2 [\varepsilon_{\mathbf{k}} - \Delta_{\nu}]^{-1}} \int D[\tilde{c}^+, \tilde{c}] e^{b_{\nu\sigma}^2 [\varepsilon_{\mathbf{k}} - \Delta_{\nu}]^{-1} \tilde{c}_{\mathbf{k}\nu\sigma}^+ \tilde{c}_{\mathbf{k}\nu\sigma} + b_{\nu\sigma} [c_{\mathbf{k}\nu\sigma}^+ \tilde{c}_{\mathbf{k}\nu\sigma} + \tilde{c}_{\mathbf{k}\nu\sigma}^+ c_{\mathbf{k}\nu\sigma}] + \tilde{\eta}_{\mathbf{k}\nu\sigma}^+ \tilde{c}_{\mathbf{k}\nu\sigma} + \tilde{c}_{\mathbf{k}\nu\sigma}^+ \tilde{\eta}_{\mathbf{k}\nu\sigma}}. \quad (33)$$

The label “dual” emphasizes that no approximation is made in this step, analogous to the transformation of a vector to the dual vector space. Note that we use here the Hubbard-Stratonovich transformation in a rather unconventional way, namely to decouple the *Gaussian* rather than the interacting part of the action.

When applying the transformation (33) to (32), the combination of the terms $e^{-S_{\text{loc}}[c^+, c]}$ and $e^{b_{\nu\sigma} [c_{\mathbf{k}\nu\sigma}^+ \tilde{c}_{\mathbf{k}\nu\sigma} + \tilde{c}_{\mathbf{k}\nu\sigma}^+ c_{\mathbf{k}\nu\sigma}]}$, integrated over the physical fields c^+ and c , yields the functional $W_{\text{loc}}[b\tilde{c}^+, b\tilde{c}] = \log Z_{\text{loc}}[b\tilde{c}^+, b\tilde{c}]$ which is diagonal in real space:

$$W_{\text{loc}}[b\tilde{c}^+, b\tilde{c}] = \ln \int D[c^+, c] \prod_i e^{-S_{\text{loc}}[c_i^+, c_i]} \times e^{\sum_{\nu\sigma} b_{\nu\sigma} [c_{i\nu\sigma}^+ \tilde{c}_{i\nu\sigma} + \tilde{c}_{i\nu\sigma}^+ c_{i\nu\sigma}]}. \quad (34)$$

We wish to arrive at a theory which contains dual (fermionic) variables only. We therefore expand W_{loc} in terms of the local coupling between dual and physical fermions and formally integrate out the latter. Due to the exponential containing S_{loc} , this integral corresponds to an average over the reference system. At expansion order $2n$ in the fields c^+ and c one therefore obtains the connected part of the n -particle impurity Green’s function. We use the freedom to choose $b_{\nu\sigma}$ to obtain a particularly convenient form of the result. Setting $b_{\nu\sigma} = (G_{\nu}^{\text{loc}})^{-1}$, where G_{ν}^{loc} is the single-particle impurity Green’s function, removes the external Green’s functions legs of the n -particle (connected) correlation functions. The local

generating functional can then be expressed in the form

$$W_{\text{loc}}[b\tilde{c}^+, b\tilde{c}] = \sum_i \left[\ln Z_{\text{loc}} - \sum_{\nu\sigma} (G_{\nu}^{\text{loc}})^{-1} \tilde{c}_{i\nu\sigma}^+ \tilde{c}_{i\nu\sigma} + V_{\text{eff}}[\tilde{c}_i^+, \tilde{c}_i] \right], \quad (35)$$

where we have defined the effective interaction between dual fermions:

$$V_{\text{eff}}[\tilde{c}_i^+, \tilde{c}_i] = \frac{1}{4} \sum_{\substack{\nu\nu'\omega \\ \sigma\sigma'}} (2 - \delta_{\sigma\sigma'}) F_{\sigma\sigma'}^{\nu\nu'\omega} \tilde{c}_{i\nu\sigma}^+ \tilde{c}_{i(\nu+\omega)\sigma} \tilde{c}_{i(\nu'+\omega)\sigma}^+ \tilde{c}_{i\nu'\sigma'} + \dots \quad (36)$$

The interaction contains the local n -particle *vertex* functions of the reference system. In particular, $F_{\sigma\sigma'}^{\nu\nu'\omega}$ is the two-particle vertex function. We have omitted three-particle and higher-order terms, as these are often neglected in practical calculations.

We define the dual action \tilde{S} through

$$\tilde{S}[\tilde{c}^+, \tilde{c}] = - \sum_{\mathbf{k}\nu\sigma} \tilde{G}_{0,\mathbf{k}\nu}^{-1} \tilde{c}_{\mathbf{k}\nu\sigma}^+ \tilde{c}_{\mathbf{k}\nu\sigma} + \sum_i V_{\text{eff}}[\tilde{c}_i^+, \tilde{c}_i], \quad (37)$$

and introduce the bare dual Green’s function

$$\tilde{G}_{0,\mathbf{k}\nu} = [(G_{\nu}^{\text{loc}})^{-1} + (\Delta_{\nu} - \varepsilon_{\mathbf{k}})]^{-1} - G_{\nu}^{\text{loc}}. \quad (38)$$

With these definitions, the final form of the generating functional in terms of dual fields is given by

$$W[\eta^+, \eta, \tilde{\eta}^+, \tilde{\eta}] = \ln \int D[\tilde{c}^+, \tilde{c}] e^{-\tilde{S}[\tilde{c}^+, \tilde{c}] - \sum_{\mathbf{k}\nu\sigma} [\varepsilon_{\mathbf{k}} - \Delta_{\nu}]^{-1} (G_{\nu}^{\text{loc}})^{-1} [\tilde{c}_{\mathbf{k}\nu\sigma}^+ \eta_{\mathbf{k}\nu\sigma} + \eta_{\mathbf{k}\nu\sigma}^+ \tilde{c}_{\mathbf{k}\nu\sigma}] + [\varepsilon_{\mathbf{k}} - \Delta_{\nu}]^{-1} \eta_{\mathbf{k}\nu\sigma}^+ \eta_{\mathbf{k}\nu\sigma} + \tilde{\eta}_{\mathbf{k}\nu\sigma}^+ \tilde{c}_{\mathbf{k}\nu\sigma} + \tilde{c}_{\mathbf{k}\nu\sigma}^+ \tilde{\eta}_{\mathbf{k}\nu\sigma}}. \quad (39)$$

From Eq. (39), the relation between the correlation functions for real and dual fields is easily derived: the single-particle propagator $\tilde{G}_{\mathbf{k}\nu} = -\langle \tilde{c}_{\mathbf{k}\nu\sigma}^+ \tilde{c}_{\mathbf{k}\nu\sigma} \rangle$ of the dual fields is obtained from a functional derivative with respect to $\tilde{\eta}^+$ and $\tilde{\eta}$ with the sources set to zero.

A closer look at the term in square brackets in Eq. (38)

reveals that it equals $G_{\mathbf{k}\nu}^{\text{loc}}$, the lattice Green’s function with the self-energy taken from the local reference problem, as also defined in the context of DMFT [Eq. (14)]. The bare dual Green’s function $\tilde{G}_{0,\mathbf{k}\nu} = G_{\mathbf{k}\nu}^{\text{loc}} - G_{\nu}^{\text{loc}}$ can be interpreted as its nonlocal part. A diagrammatic expansion in terms of the dual Green’s function clearly ac-

counts for non-local contributions, while the local ones are taken into account on the level of the impurity model. It is intuitively clear that double counting of local contributions is avoided with this construction. The derivative of $W[\eta^+, \eta, \tilde{\eta}^+, \tilde{\eta}]$ with respect to the sources η^+ and η yields, on the other hand, yields the physical Green's function $G_{\mathbf{k}\nu}$. Applying this functional derivative to Eq. (39) straightforwardly yields the relation

$$G_{\mathbf{k}\nu} = [\varepsilon_{\mathbf{k}} - \Delta_{\nu}]^{-1} (G_{\nu}^{\text{loc}})^{-1} \tilde{G}_{\mathbf{k}\nu} (G_{\nu}^{\text{loc}})^{-1} [\varepsilon_{\mathbf{k}} - \Delta_{\nu}]^{-1} - [\varepsilon_{\mathbf{k}} - \Delta_{\nu}]^{-1}, \quad (40)$$

which can be rewritten as a relation between the dual and the physical self-energy in the following form:

$$\Sigma_{\mathbf{k}\nu} = \Sigma_{\nu}^{\text{loc}} + \frac{\tilde{\Sigma}_{\mathbf{k}\nu}}{1 + G_{\nu}^{\text{loc}} \tilde{\Sigma}_{\mathbf{k}\nu}}. \quad (41)$$

Analogous relations between higher-order correlation functions are obtained similarly from higher-order derivatives, see Brener *et al.*, 2008 and Rubtsov *et al.*, 2009. Using these exact relations, any result obtained in dual space can be transformed back to the physical fermion space.

Because of the complicated form of the dual interaction V_{eff} , the benefits of the transformation to dual variables are not immediately obvious. The idea is that the bare dual propagator \tilde{G} and the bare dual interaction V_{eff} implicitly contain the local physics through the underlying AIM and represent a much better starting point for any kind of perturbative expansion than the original action.

Note that since the hybridization is arbitrary, DF provides an expansion around a generic AIM. In the particular case where Δ_{ν} equals its DMFT value, the DF approach represents a diagrammatic expansion around DMFT. In this case it is easy to see that inserting the corresponding $\tilde{G}_{0,\mathbf{k}\nu}$ into (40) indeed yields the DMFT Green's function. DMFT therefore corresponds to a system of non-interacting dual fermions and appears as the lowest order in the approach. It is believed that the DF series delivers a good practical convergence even in cases where standard Feynman diagrammatic techniques fail.

In practice, two approximations are performed for the action in Eq. (37): i) The dual interaction is terminated at some finite-order, typically only the local two-particle vertex function $F^{(4)} = F$ is taken into account. To which extent this is justified is an open question (Ribic *et al.*, 2016a). However, numerical results and scaling considerations (see below) suggest that contributions from higher-order vertices can often be neglected. ii) An approximation to the dual self-energy is constructed using Feynman diagrams.

a. Selection of diagrams The diagrammatic elements of the expansion are the dual propagators \tilde{G}_0 and the n -particle vertices of the local reference model, see Fig. 12.

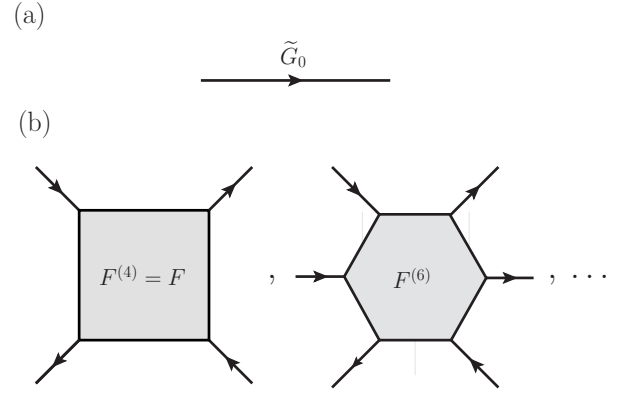


Figure 12 Diagrammatic elements of the DF approach: (a) the bare DF propagator \tilde{G}_0 [Eq. (38)] given by the purely *non-local* Green's function and (b) the DF interaction represented by the local connected n -particle vertex functions $F^{(2n)}$.

In practice, the dual self-energy is constructed from a subset of finite or infinite-order dual diagrams. Generic examples are shown in Fig. 13. Since the n -particle vertex functions in the dual interaction are fully antisymmetric by virtue of the fermionic anticommutation relations, the diagrammatic rules of the perturbation theory (Hafermann, 2010; Negele and Orland, 1998) are similar to those of Hugenholtz, 1957. Because the coupling b_{ν} introduced in Eq. (33) between physical and dual fermions is local and spin-diagonal, the choice of diagrams is very similar to regular perturbation theory and can be guided by the physics. The non-local expansion scheme discussed below shows that the DF approach is in fact an efficient scheme to resum certain classes of diagrams in lattice fermion space. Exact relations between dual and physical fermions further guarantee that the poles corresponding to two-particle excitations (and higher-order processes) are the same for dual and physical fermions (Brener *et al.*, 2008).

The leading-order diagram of the expansion is the local Hartree-Fock type diagram shown in Fig. 13 (a). This diagram gives a local contribution which can be eliminated by a specific choice of the hybridization function, see below. The next-leading diagram shown in Fig. 13 (b) defines the second-order DF approximation $\text{DF}^{(2)}$. Fig. 13 (c) is the leading diagram containing a three-particle vertex. $\text{DF}^{(2)}$ gives rise to a pseudogap-like behavior in the weak-to-intermediate coupling regime of the 2D Hubbard model in the symmetry broken phase (Rubtsov *et al.*, 2008). An important approximation is the ladder DF approximation (Hafermann *et al.*, 2009c), which sums generic ladder diagrams shown in Fig. 13 (d) to all orders. The ladder approximation describes antiferromagnetic fluctuations and the pseudogap in the paramagnetic phase and yields accurate results in practice over a wide parameter range (Gukelberger *et al.*, 2016). The particle-

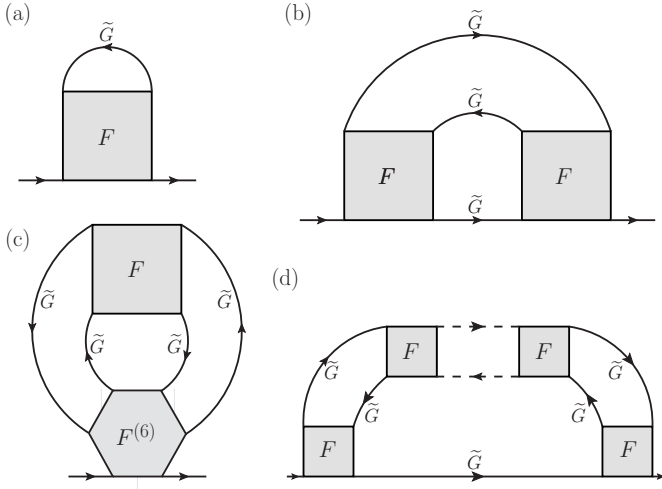


Figure 13 (a) DF Hartree-Fock and (b) second-order diagram constructed from the local two-particle vertex. (c) An example of a diagram containing a three-particle vertex. (d) Generic DF ladder diagram constructed from two-particle vertices.

hole ladder DF self-energy is given by

$$\begin{aligned} \tilde{\Sigma}_{\mathbf{k}\nu} = & - \sum_{k'qr} A_r F_r^{\nu\nu'\omega} \tilde{G}_{\mathbf{k}'\nu'} \tilde{G}_{(\mathbf{k}'+\mathbf{q})(\nu'+\omega)} \tilde{G}_{(\mathbf{k}+\mathbf{q})(\nu+\omega)} \\ & \times [F_{\text{lad},r,\mathbf{q}}^{\nu\nu'\omega} - \frac{1}{2} F_r^{\nu\nu'\omega}] \end{aligned} \quad (42)$$

Here, we have introduced the notations $A_c = 1/2$, $A_s = 3/2$ for $r = c, s$, where the factor 3 accounts for the spin degeneracy. The expression is obtained by incorporating ladder diagrams from the ph and $\bar{p}\bar{h}$ channels, cf. Sec. II.A, into the lattice vertex in the dual Schwinger-Dyson equation. Since here the interaction is fully antisymmetric, both channels give identical contributions. F_{lad} is the vertex in the ladder approximation as defined in Eq. (21). The latter can equivalently be obtained by solving a Bethe-Salpeter equation written in terms of F and \tilde{G} (Brener *et al.*, 2008).

Particle-particle fluctuations can be added straightforwardly. When it is known a priori in which channel the dominant instability occurs (magnetic, charge, superconducting) it is sufficient to construct ladder diagrams in this channel, whereas for competing instabilities one has to resort to parquet diagrams in dual space. To avoid a possible bias through the restriction to a certain subset of diagrams, Iskakov *et al.*, 2016 and Gukelberger *et al.*, 2016 developed a method to sample DF diagrams with the two-particle vertex using diagrammatic Monte Carlo, which shows good agreement with diagrammatic determinant Monte Carlo benchmarks.

b. Choice of hybridization function The hybridization function Δ_ν can be chosen arbitrarily, and DMFT may or

may not be the optimal starting point in the presence of strong nonlocal correlations. Since the underlying AIM can be solved numerically exactly, it is desirable to include a major part of the correlations into this reference system. The hybridization of the AIM is updated iteratively until it either fulfills the condition

$$\sum_{\mathbf{k}} G_{\mathbf{k}\nu} = G_\nu^{\text{loc}}, \quad (43)$$

with $G_{\mathbf{k}\nu}$ from Eq. (40), or the more commonly employed condition

$$\sum_{\mathbf{k}} \tilde{G}_{\mathbf{k}\nu} = 0. \quad (44)$$

The latter condition implies that non-local dual self-energy contributions that yield contributions to the local dual Green's function will effectively be absorbed into the impurity problem. Furthermore, the Hartree-diagram, Fig.13 (a) and all diagrams which contain a local loop vanish.

The effect of updating the impurity is particularly important in low dimensions, where DMFT and the exact solution can differ qualitatively. It is for example essential to capture the Mott phase in one and two dimensions, in the parameter region where DMFT yields a metallic solution. The insulating solution shown in Fig. 31 has been obtained from a metallic DMFT starting point using condition (44), while (43) yields a strongly renormalized metal in this regime. Note that the final hybridization in the former case is qualitatively different from the DMFT one, because the impurity model itself becomes insulating. When to apply which self-consistency condition has so far not been investigated systematically.

In practice, the conditions (43) or (44) are implemented in a self-consistent scheme as shown in Fig. 14: (i) First, the local self-energy Σ^{loc} and the local two-particle and possibly higher-order vertex functions ($F, F^{(6)}, \dots$) are extracted from an initial solution of the AIM. From the former, the bare dual propagator $\tilde{G}_{0,\mathbf{k}\nu}$ is constructed according to Eq. (38). Here, the bare dispersion $\varepsilon_{\mathbf{k}}$ or the non-interacting lattice Green's function $G_{0,\mathbf{k}\nu}$ enters the flow diagram. (ii) The dual self-energy $\tilde{\Sigma}_{\mathbf{k}\nu}$ is calculated by means of dual perturbation theory, which can include a self-consistent renormalization of the dual Green's function in the selected diagrams. (iii) From the dual self-energy the dual Green's function $\tilde{G}_{\mathbf{k}\nu}$ is obtained via the Dyson equation and finally the lattice Green's function $G_{\mathbf{k}\nu}$ via the transformation (40). (iv) The hybridization is updated using either $\tilde{G}_{\mathbf{k}\nu}$ or $G_{\mathbf{k}\nu}$ to fulfill the condition (43) or (44). This closes the self-consistency cycle.

c. Scaling considerations and convergence Since DF can be viewed as an expansion around DMFT, it is further instructive to consider the scaling from the perspective

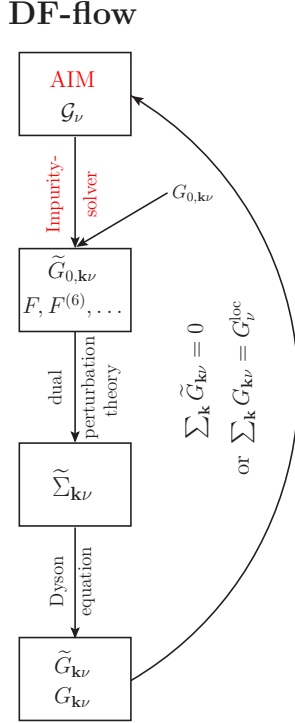


Figure 14 Flow diagram for DF calculations.

of an expansion in $1/d$. In large dimensions, the hopping scales as $t \sim \mathcal{O}(1/\sqrt{d})$ and hence the same holds for the purely non-local $\tilde{G} \sim \mathcal{O}(1/\sqrt{d})$. The leading second-order, ladder diagrams [Fig. 13 (d)] and parquet scale as $\mathcal{O}(1/\sqrt{d}^3)$ in real space. The diagram Fig. 13 (c) and other diagrams with higher-order vertices are of $\mathcal{O}(1/d^2)$.

The DF approach further converges quickly around both non-interacting and strong-coupling limits. It essentially inherits this property from DMFT. In the weak-coupling limit $U \rightarrow 0$ the vertex functions are small. In the atomic limit $\epsilon_{\mathbf{k}} \rightarrow 0$, the dual Green's function for $\Delta \equiv 0$ becomes the small parameter: $\tilde{G}_{\mathbf{k}\nu} \approx \epsilon_{\mathbf{k}}(G_\nu^{\text{loc}})^2$. For finite $\Delta \neq 0$ the leading eigenvalue of the ladder in dual space is significantly reduced compared to the one of physical fermions also at intermediate coupling, indicating faster convergence (Hafermann *et al.*, 2009c).

1. Non-local expansion scheme

The non-local expansion scheme (Li, 2015) is a general framework to construct approximations for strongly correlated systems that includes fluctuations at all length scales. Closely related to the DF approach, the action \mathcal{S} (29) of a model with local interaction is separated into an arbitrary local reference system \mathcal{S}^{loc} (not necessarily an impurity model) and a term containing a non-local hybridization $V_{ij,\nu} := [\mathcal{G}_\nu^{-1}]_{ij}$ (which equals the non-local

part of the bare propagator):

$$\mathcal{S}[c^+, c] = \sum_i \mathcal{S}^{\text{loc}}[c_i^+, c_i] + \sum_{i \neq j} \sum_{\nu\sigma} c_{i\nu\sigma}^+ V_{ij\nu} c_{j\nu\sigma} \quad (45)$$

Instead of introducing dual variables, the non-local expansion scheme is generated by expanding the lattice Green's function directly in the non-local hybridization:

$$G_{kl,\nu} = -\frac{1}{Z} \prod_{i=1}^N \int D[c_i^+, c_i] e^{-\mathcal{S}^{\text{loc}}[c_i^+, c_i]} \sum_{n=0}^{\infty} \frac{(-1)^n}{n!} \times \left[\sum_{i \neq j} \sum_{\nu'\sigma'} c_{i\nu'\sigma'}^+ V_{ij,\nu'} c_{j\nu'\sigma'} \right]^n c_{k\nu'\sigma'} c_{l\nu'\sigma'}^+ \quad (46)$$

The cumulant expansion (Metzner, 1991; Sarker, 1988) is obtained for $V_{ij} = t_{ij}$. Similar to DF, the path integral over the fermionic fields weighted with the exponential of the local action generates the local correlation functions of the local interacting system. The DF approach can be understood as a particular diagrammatic resummation scheme in the non-local expansion scheme: If we take the non-local hybridization V_{ij} as the Fourier transform of $-(\Delta_\nu - \epsilon_{\mathbf{k}})$, the actions (31) and (45) take the same form. The bare dual propagator then corresponds to the renormalized hybridization $\tilde{V}_{ij} = ([V^{-1} - G^{\text{loc}} \mathbb{1}]^{-1})_{ij}$ (note that Li, 2015 uses couplings $b_{\nu\sigma} = 1$). Using the resummation $G_{\mathbf{k}\nu} = \Lambda_{\mathbf{k}\nu} / (\mathbb{1} - V_{\mathbf{k}\nu} \Lambda_{\mathbf{k}\nu})$ where $\Lambda_{\mathbf{k}\nu}$ contains 1PI diagrams in terms of V , one can show that a DF approximation with given dual self-energy $\tilde{\Sigma}_{\mathbf{k}\nu}$ is equivalent to the non-local expansion scheme with $\Lambda_{\mathbf{k}\nu} = G_\nu^{\text{loc}} + \tilde{\Sigma}_{\mathbf{k}\nu}$. The scheme therefore provides further justification for the choice of diagrams based on physical considerations.

2. Generalizations and superperturbation theory

We have discussed the derivation of the DF approach for translationally invariant lattices. The method can straightforwardly be generalized to other scenarios. It can be derived in real space (Takemori, 2016) to address spatially inhomogeneous and finite systems, to disordered systems (Sec. IV.D) and the symmetry broken phase (Rubtsov *et al.*, 2009). Susceptibilities can be calculated to detect symmetry broken phases (Brener *et al.*, 2008; Li *et al.*, 2008). The formalism can be generalized straightforwardly also to the multiorbital case and to clusters, where the DF expansion is performed around a small cluster as the reference system (see Sec. III.E).

DF as a cluster solver DF can be employed as an approximate solver for large clusters occurring in the context of cluster extensions of DMFT (Maier *et al.*, 2005a). We note that this is conceptually different from expanding around a cluster reference system, which we discuss in Sec. III.E. Here, DF implementations often work

with a discretized grid and Fourier transforms and hence solve large but finite lattices with periodic boundary conditions. From this perspective, the DF cluster must be embedded into a mean-field for including the third length scale beyond the extension of the cluster (Yang *et al.*, 2013). Performing the DCA coarse-graining on the DF lattice significantly enhances the convergence with system size and facilitates reaching the thermodynamic limit.

Superperturbation theory While DF can be viewed as a diagrammatic extension of DMFT, the DF idea of performing a diagrammatic expansion around a reference problem that can be easily solved is more general. We refer to this kind of perturbation theory around a non-trivial – for example interacting – starting point as a superperturbation.

We have the freedom to expand around a local reference system (30) with a discrete hybridization $\Delta_\nu \rightarrow \Delta_\nu^{(N)} = \sum_{k=1}^N |V_k|^2 / (i\nu - \epsilon_k)$ and a small number N of bath sites, which can be solved with ED, see Sec. II.D. For $N = 0$ we obtain the strong-coupling expansion of the Hubbard model (Pairault *et al.*, 1998, 2000). For very small $N = 1, 2$ the DF perturbation also accounts for the local physics not captured in the simple reference system. The choice of the hybridization parameters is not unique (Jung, 2010). The solution however only takes seconds on a modern PC and allows for analytical continuation using Padé approximants (see Sec. IV.A).

The approach can also be applied as a solver for the local impurity problem (30) itself, taking an impurity with hybridization $\Delta_\nu^{(N)}$ as the reference (Hafermann *et al.*, 2009a). One can show analytically that a first-order approximation to the dual self-energy reproduces the strongly hybridized weak-coupling and the weakly hybridized strong-coupling limits. For $\Delta_\nu^{(N)} \equiv 0$ and in the limit of small hybridization Δ_ν , it reproduces the non-interacting limit and the result of a first-order expansion of the Green's function in the hybridization: $G_{12} \approx g_{12} + g_{12} \beta \text{Tr}[g \Delta] + \chi_{1234} \Delta_{43}$ (Dai *et al.*, 2005). The one- and two-particle Green's functions g_{12} and χ_{1234} of the reference system can be expressed in terms of the ED eigenvalues and matrix elements and can be analytically continued to the real axis (Jung *et al.*, 2011). The naive expansion exhibits a causality problem, which can however be cured (Jung, 2010) by introducing a renormalization parameter (Krivenko *et al.*, 2010).

Superperturbation theory can further be formulated on the Keldysh contour (Jung *et al.*, 2012), allowing for the non-equilibrium solution of the AIM. Jung *et al.*, 2012 studied the time evolution after switching on the hybridization of the AIM. Muñoz *et al.*, 2013 addressed the nonlinear conductance through a quantum dot. The authors developed a first-order DF expansion around the

symmetric, interacting SIAM as the reference system in terms of the level energy E_d of the dot up to order $\mathcal{O}(V^2)$ in the coupling V to the leads. The reference system was solved within renormalized perturbation theory around the strong coupling fixed point. Contrary to perturbation theory in U , which preserves current conservation only in the particle-hole symmetric AIM, the DF scheme is current-conserving beyond $\mathcal{O}(V^2)$. Merker *et al.*, 2013 found good agreement with numerical renormalization group calculations for the linear conductance.

C. One-particle irreducible (1PI) approach

In the DF theory the interaction V_{eff} [Eq. (36)] between the dual electrons is given by the local n -particle vertices F of the reference system. Except for the two-particle vertex, these vertices in general contain *one-particle reducible* contributions. There are two questions associated with the such terms in the DF approach: (i) Consider the second order diagram of DF in Fig. 13 (b), which contains only dual, i.e., nonlocal [see Eq. (38)] propagators \tilde{G} . A corresponding diagram where one of the three lines is the local Green's function G^{loc} is shown in Fig. 15. This diagram is included in DF at the level of the local *three-particle* particle vertex, which is typically neglected. It is not obvious why such diagrams should not contribute to the dual self-energy with the same order of magnitude as second-order and ladder diagrams. (ii) The inclusion of the local three-particle vertex within DF leads to seemingly spurious *one-particle reducible* contributions to the self-energy as depicted in Fig. 16. Such contributions are canceled by the transformation Eq. (41) from the dual to the physical fermions (Katanin, 2013). However, when three-particle local vertices are neglected, Eq. (40) *introduces* rather than removes such spurious contributions in the lattice Green's functions of the physical electrons.

The 1PI approach aims at eliminating all terms which stem from the one-particle reducible vertices in the perturbative expansion of the self-energy. We can switch from the one-particle reducible of DF to such a 1PI formalism by a Legendre transformation of the generating functional W_{loc} [Eqs. (34,35)] from the Grassmann field for the dual Fermions $\tilde{c}^{(+)}$ to new 1PI fields $\phi^{(+)}$:

$$\Gamma_{\text{loc}}[\phi^+, \phi] = W_{\text{loc}}[\tilde{c}^+, \tilde{c}] + \sum_{i\nu\sigma} [\tilde{c}_{i\nu\sigma}^+ \phi_{i\nu\sigma} + \phi_{i\nu\sigma}^+ \tilde{c}_{i\nu\sigma}],$$

$$\phi_{i\nu\sigma}^+ = \frac{\delta W_{\text{loc}}[\tilde{c}^+, \tilde{c}]}{\delta \tilde{c}_{i\nu\sigma}^+}, \quad \phi_{i\nu\sigma} = -\frac{\delta W_{\text{loc}}[\tilde{c}^+, \tilde{c}]}{\delta \tilde{c}_{i\nu\sigma}^+}. \quad (47)$$

The new functional Γ_{loc} generates the local 1PI vertex functions of the local problem, see Negele and Orland, 1998. From the very beginning this precludes the appearance of 1PI contributions in the three-particle and higher-order vertex functions. Replacing W_{loc} in the generating functional of the DF approach, Eq. (34), by Eq. (47) and

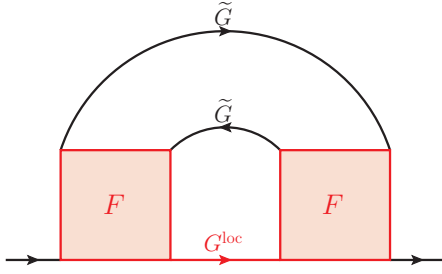


Figure 15 (Color online) First order DF diagram that includes the local three-particle vertex (red part of the diagram). We show the particular example of a three-particle vertex that is *one-particle reducible* (cutting the G^{loc} line separates the red part into two pieces). Such a vertex is included in DF but not in 1PI which is *one-particle irreducible*.

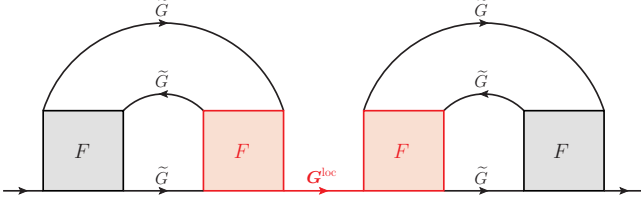


Figure 16 (Color online) Third order diagram for the dual self-energy including the local three-particle vertex (red). In terms of real electrons this contribution appears to be spurious as it corresponds to a one-particle reducible contribution to the self-energy.

$$\mathcal{S}_0^{\text{1PI}}[\phi^+, \phi, \psi^+, \psi] = - \sum_{k\sigma} \left\{ G_k^{-1} (\phi_{k\sigma}^+ \phi_{k\sigma} + \psi_{k\sigma}^+ \phi_{k\sigma} + \phi_{k\sigma}^+ \psi_{k\sigma}) + \left[G_k^{-1} - (G_\nu^{\text{loc}})^{-1} \right] \psi_{k\sigma}^+ \psi_{k\sigma} \right\}, \quad (48a)$$

$$\begin{aligned} \mathcal{S}_I^{\text{1PI}}[\phi^+, \phi, \psi^+, \psi] = & \frac{1}{4} \sum_{kk'q} \sum_{\sigma\sigma'} (2 - \delta_{\sigma\sigma'}) F_{\sigma\sigma'}^{\nu\nu'\omega} \left[\phi_{k\sigma}^+ \phi_{(k+q)\sigma} \phi_{(k'+q)\sigma'}^+ \phi_{k'\sigma'} + \right. \\ & \left. + 2\psi_{k\sigma}^+ \phi_{(k+q)\sigma} \phi_{(k'+q)\sigma'}^+ \phi_{k'\sigma'} + 2\phi_{k\sigma}^+ \phi_{(k+q)\sigma} \phi_{(k'+q)\sigma'}^+ \psi_{k'\sigma'} \right] + \sum_i \text{Tr} \ln M[\phi_i^+, \phi_i], \end{aligned} \quad (48b)$$

$$\mathcal{S}_s^{\text{1PI}}[\phi^+, \phi, \psi^+, \psi] = - \sum_{k\sigma} [(\phi_{k\sigma}^+ + \psi_{k\sigma}^+) \eta_{k\sigma} + \eta_{k\sigma}^+ (\phi_{k\sigma} + \psi_{k\sigma})], \quad (48c)$$

where the 4-vector notation has been adopted. $M[\phi_i^+, \phi_i]$ is the Jacobian of the transformation from the variables \tilde{c}^+, \tilde{c} to ϕ^+, ϕ . Additional fields ψ^+ and ψ have been introduced in Eqs. (48) that decouple three-particle interaction terms for ϕ^+ and ϕ by means of a Hubbard-Stratonovich transformation. The latter arise from the application of the Legendre transform (47) to the Gaussian term in the dual fields in Eq. (33) (for details see Rohringer *et al.*, 2013 and Rohringer, 2013). They describe the one-particle reducible contributions of the three-particle and higher-order vertices to the self-energy.

We can understand the $\phi^{(+)}$ and $\psi^{(+)}$ as different parts

expanding Γ_{loc} up to fourth order in ϕ_i^+ and ϕ_i one can show (Rohringer, 2013; Rohringer *et al.*, 2013) that one obtains the action $\mathcal{S}^{\text{1PI}} = \mathcal{S}_0^{\text{1PI}} + \mathcal{S}_I^{\text{1PI}} + \mathcal{S}_s^{\text{1PI}}$ of the 1PI approach with

of a bare 1PI propagator:

$$\mathbf{G}_{0,k} = \frac{1}{\beta} \begin{pmatrix} \langle \phi_{k\sigma}^+ \phi_{k\sigma} \rangle & \langle \phi_{k\sigma}^+ \psi_{k\sigma} \rangle \\ \langle \psi_{k\sigma}^+ \phi_{k\sigma} \rangle & \langle \psi_{k\sigma}^+ \psi_{k\sigma} \rangle \end{pmatrix} = \begin{pmatrix} G_{\mathbf{k}}^{\text{loc}} - G_\nu^{\text{loc}} & G_\nu^{\text{loc}} \\ G_\nu^{\text{loc}} & -G_\nu^{\text{loc}} \end{pmatrix}, \quad (49)$$

where $G_{\mathbf{k}}^{\text{loc}}$ is the lattice Green's function which including the local self-energy of the reference AIM model, see Eq. (14). The propagator for the $\phi^{(+)}$ fields, $\tilde{G}_{0,\mathbf{k}\nu} = G_{\mathbf{k}\nu}^{\text{loc}} - G_\nu^{\text{loc}}$, is purely non-local and equals the dual Green's function. The propagator for the $\psi^{(+)}$ fields, on the other hand, is given by the local Green's function G_ν^{loc} of the reference system. This diagrammatic element is *absent* in DF. The diagrammatic elements of Eqs. (48) and (49), which define the 1PI perturbation theory, are

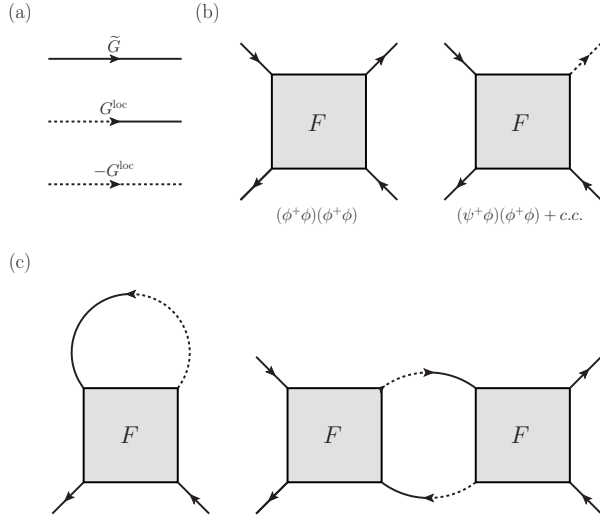


Figure 17 Diagrammatic elements of the 1PI approach: (a) The bare propagators Eq. (49); (b) The interaction terms which are given by the local vertex function F ; (c) Terms that stem from the Jacobian $M[\phi_i^+, \phi_i]$, providing for the cancellation of double-counted local contributions, for more details see (Rohringer, 2013). Solid and dashed lines correspond to ϕ and ψ fields, respectively.

illustrated graphically in Fig. 17.

Ladder Approximation in the 1PI approach Similarly to DFA and DF, we restrict our considerations to ladder diagrams for the 1PI action, assuming that they describe the most important physical processes. If we consider all possible bubble diagrams constructed from the diagrammatic elements depicted in Figs. 17 (a) and 17 (b), but omit contributions that are canceled by counter-terms of Fig. 17 (c) and terms that vanish because of the self-consistency condition (44), the 1PI self-energy is eventually obtained as (Rohringer, 2013; Rohringer et al., 2013):

$$\begin{aligned} \Sigma_{1\text{PI},k} = & \Sigma_{\nu}^{\text{loc}} - \sum_{qk'r} A_r \Gamma_r^{\nu\nu'\omega} \left[G_{k'}^{\text{loc}} G_{k'+q}^{\text{loc}} F_{\text{lad},r,\mathbf{q}}^{\nu'\nu\omega} \right. \\ & \left. - G_{\nu'}^{\text{loc}} G_{\nu'+\omega}^{\text{loc}} F_r^{\nu'\nu\omega} \right] G_{k+q}^{\text{loc}} \\ & + \frac{1}{2} \sum_{k'qr} A_r F_r^{\nu\nu'\omega} \tilde{G}_{k'} \tilde{G}_{k'+q} F_r^{\nu'\nu\omega} \tilde{G}_{k+q}. \end{aligned} \quad (50)$$

with $A_c = 1/2$, $A_s = 3/2$ for $r = c, s$ as in Eq. (42), and $F_{\text{lad},r,\mathbf{q}}^{\nu\nu'\omega}$ is the same BSE ladder vertex as in DFA [Eq. (21)]. The last line of Eq. (50) subtracts the term counted twice in the $\lambda = ph$ and $\lambda = \bar{p}\bar{h}$ ladder. Fig. 18 provides an overview of the diagrammatic differences between the ladder versions of DF, 1PI and DFA, by explicitly comparing the third order diagrams in F .

The high-frequency behavior of the 1PI ladder self-energy $\Sigma_{1\text{PI},k}$ exhibits the very same violation of the exact $1/i\nu$ -asymptotics as the corresponding ladder DFA

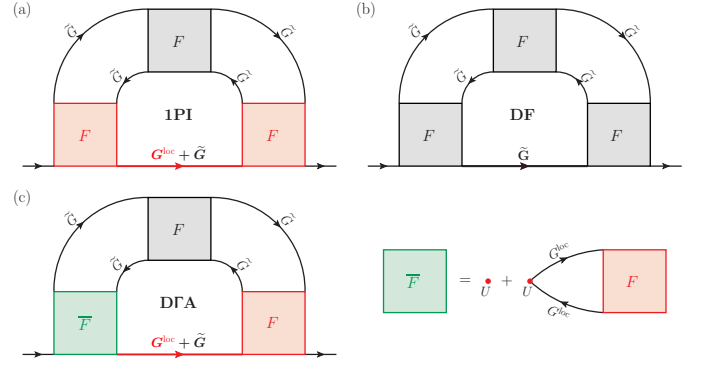


Figure 18 (Color online) Third order diagrams in terms of the local vertex F_{loc} for (a) 1PI, (b) DF, and (c) DFA. The red part marks contributions that are included on the two-particle vertex level in 1PI and DFA. In DF they require the inclusion of the one-particle reducible three-particle vertex, cf. Fig. 15.

self-energy. The problem requires the inclusion of the Moriya- λ correction, Eq. (26), as in DFA. For further details see Rohringer, 2013 and Rohringer et al., 2013.

D. DMFT plus functional renormalization group

The functional renormalization group (fRG) approach (for a review see Metzner et al., 2012) provides an alternative way for generating non-local correlations beyond DMFT — through the fRG flow between the local problem and the corresponding lattice problem. To generate such a flow, the DMF²RG approach of Taranto et al., 2014 considers the decomposition of the lattice action in the form (31), where the coupling to the local reference problem is controlled by the flow parameter Λ

$$\mathcal{S}_{\Lambda}[c^+, c] = \sum_i \mathcal{S}_{\text{loc}}[c_i^+, c_i] + \Lambda \sum_{\nu\mathbf{k}\sigma} (\varepsilon_{\mathbf{k}} - \Delta_{\nu}) c_{\nu\mathbf{k}\sigma}^+ c_{\nu\mathbf{k}\sigma}. \quad (51)$$

\mathcal{S}_{Λ} interpolates between the local DMFT action Eq. (30) for $\Lambda = 0$ and the full action of the model at hand Eq. (29) for $\Lambda = 1$. The action (51) can be used to construct the flow equations in the 1PI fRG approach for the Λ -dependent self-energy $\Sigma_{\Lambda,k}$ and the two-particle vertex $F_{\Lambda}^{kk'q}$. In schematic form, these flow equations read

$$\frac{d\Sigma_{\Lambda}}{d\Lambda} = F_{\Lambda} \circ S_{\Lambda}, \quad (52a)$$

$$\frac{dF_{\Lambda}}{d\Lambda} = F_{\Lambda} \circ (S_{\Lambda} \circ G_{\Lambda}) \circ F_{\Lambda}, \quad (52b)$$

where \circ denotes summation over intermediate momenta and frequencies according to the standard diagrammatic rules and

$$S_{\Lambda,k} = G_{\Lambda,k}^2 (\varepsilon_{\mathbf{k}} - \Delta_{\nu}) \quad (53)$$

is the so-called single-scale propagator with

$$G_{\Lambda,k} = [i\nu - \Lambda\varepsilon_{\mathbf{k}} - (1 - \Lambda)\Delta_{\nu}\Sigma_{\Lambda,k}]^{-1} \quad (54)$$

the flowing Green's function. As in conventional fRG calculations, in Eqs. (52a,b) we have truncated the infinite hierarchy of fRG equations by neglecting the three-particle vertices. The initial conditions for the differential equations (52) are determined through the local reference problem, $\Sigma_{\Lambda=0,k} = \Sigma_{\nu}^{\text{loc}}$ and $F_{\Lambda=0,r}^{kk'q} = F_r^{\nu\nu'\omega}$. By construction, the DMF²RG method is free from double counting: the local properties continuously evolve towards the corresponding lattice counterparts. Note that contrary to the dual fermion approach the method is formulated in terms of physical, and not dual fermions, although a similar method can also be applied in dual space (Katanin, 2015; Wentzell *et al.*, 2015).

Differently from the parquet DfA, the DMF²RG approach performs the summation of parquet-type diagrams via the solution of differential equations. At the same time it is based on the local 1PI vertex F instead of the more cumbersome 2PI vertex Λ (not to be confused with the flow parameter Λ). The vertex F collects non-local components through the fRG flow. In standard fRG, F grows fast with increasing interaction strength so that the truncations of the infinite hierarchy of fRG equations at the two-particle level is less justified. The hope is that with DMFT presenting a good correlated starting point, the actual fRG flow needs to cover less ground in DMF²RG than in standard fRG.

First DMF²RG calculations for the $2d$ Hubbard model at half-filling have been performed by Taranto *et al.*, 2014. From a numerical point of view, the bottleneck of the fRG flow in Eqs. (52) are memory restrictions, because the vertex functions that depend on three momenta and frequencies in different channels are intertwined. This is similar as for the parquet Eqs. (8,10) and can be mitigated by using vertex asymptotics (Wentzell *et al.*, 2016).

Recently, Katanin, 2016 proposed to employ the 2PI fRG approach to consider non-local corrections beyond EDMFT (see Sec. III.G). This generalization is especially useful for the treatment of non-local two-particle interactions in strongly correlated systems. Using this approach one can consider the evolution from the EDMFT local problem Eq. (60) to the lattice problem Eq. (59). The resulting equations are similar, but not identical to those in the DB γ approach of Stepanov *et al.*, 2016b: the 2PI approach includes the effect of the one-particle reducible six-point and higher-order vertices in the dual boson approach, cf. the discussion in Sec. III.C.

E. Extending vertex approaches to clusters

In the previous sections, we have reviewed extensions of DMFT that generate non-local correlations from a *local* vertex. All of these approaches can be generalized quite naturally by taking the vertex calculated on a small but finite cluster as the starting point. This has

the advantage that certain short-range correlations that are difficult to capture diagrammatically, such as the formation of a compound singlet by neighboring spins, can be treated numerically in a more rigorous way. At the same time, correlations on length scales that exceed numerically feasible cluster sizes are treated diagrammatically. Using DCA or cluster DMFT for a small cluster and DfA, DF, etc. for a large cluster, also offers the advantage that it is possible to study the convergence w.r.t. the size of the small and large cluster systematically.

Such cluster-based calculations have been pioneered by Slezak *et al.*, 2009 who proposed a multi-scale many-body approach. Correlations on short length-scales are incorporated by calculating the irreducible vertex $\Gamma_{ph,r}^{kk'q}$ on a small DCA cluster corresponding to a coarse \mathbf{k} -grid within QMC. Correlations on larger length scales are accounted for by solving the BSE equation for the approximate full vertex on a larger cluster, in analogy to the ladder DfA of Sec. III.A.2. The self energy is obtained through the Schwinger-Dyson equation. Correlations exceeding the larger cluster are accounted for on a mean-field level. As calculating the vertex on a cluster is a formidable numerical task, Slezak *et al.*, 2009 approximated $\Gamma_{ph,r}^{kk'q} \approx \Gamma_{ph,r}^{kk'0}$, neglecting the dependence on the bosonic momentum and frequency. They also considered a simplifying ansatz for the self-energy and more approximate solutions for the larger cluster. Further details of the approach, its validation and application to the $1d$ Hubbard model can be found in Slezak *et al.*, 2009.

In the cluster DF (CDF) approach by Hafermann *et al.*, 2008 the DF expansion is performed around the cellular DMFT (CDMFT) solution as the reference system. For the $1d$ Hubbard model, CDF is considerably closer than DF to the benchmark of density matrix renormalization group (DMRG) (Hafermann *et al.*, 2008). A disadvantage is that CDMFT breaks translational invariance of the lattice. Hafermann, 2010 showed that the dual corrections however tend to partially restore the translational invariance. Another consequence of broken translational invariance is that the two-particle vertex is a rank-4 tensor in the spatial indices. An alternative is to perform a diagrammatic expansion around a DCA cluster, by embedding the latter in a DF lattice. In this DFDCA approach by Yang *et al.*, 2011, the vertex function depends on only three cluster momenta and requires less memory. It is worthwhile to consider the scaling of the approach with the linear cluster size L_c . The dual Green's function acts as a small parameter, as it scales as $\tilde{G} \sim \mathcal{O}(1/L_c)$; the second-order DF self-energy diagram is of $\mathcal{O}(1/L_c^3)$ while the leading three-particle vertex diagram is of $\mathcal{O}(1/L_c^4)$, which again justifies neglecting it. The DFDCA results show that already the second-order correction beyond a small 2×2 cluster significantly reduces the Néel temperature. Higher-order diagrams included in a ladder or parquet approximation further re-

duce the critical temperature, while vertex corrections that are irreducible in the ladder channel tend to slightly increase it.

F. DMFT + non-local self-energy

In this Section, we review *DMFT + non-local self-energy* methods which supplement the local DMFT self-energy by non-local contributions obtained independently using another method, typically within perturbation theory in the bare interaction. This implies an explicit separation of the local and non-local parts of the self-energy. These methods have been proposed earlier and are generally simpler than the DMFT extensions described in the previous subsections, which incorporate non-local correlations, more systematically, on the basis of a local two particle vertex.

The idea to augment DMFT with a non-local self-energy was first introduced for the non-local electron interaction in the context of the *GW+DMFT* and *EDMFT+GW* approach (Biermann *et al.*, 2003; Sun and Kotliar, 2002). These supplement the local DMFT self-energy by the screened exchange diagram of *GW*, which offers an appealing route to realistic material calculations. We discuss *EDMFT+GW* together with other extensions of *EDMFT* in Sec. III.G; and refer the reader to Tomczak *et al.*, 2017 for a tutorial review of *GW+DMFT*.

For the Hubbard model, the summation of an infinite series of diagrams for the non-local self-energy was considered in *DMFT+ Σ_k* (Kuchinskii *et al.*, 2005, 2006; Sadovskii *et al.*, 2005), and *DMFT+FLEX* (Gukelberger *et al.*, 2015; Kitatani *et al.*, 2015). Like all DMFT + non-local self-energy methods, they are based on the separation

$$\Sigma_{\mathbf{k}\nu} = \Sigma_{\nu}^{\text{loc}} + \Sigma_{\mathbf{k}\nu}^{\text{nlc}}, \quad (55)$$

where Σ^{loc} includes contributions exclusively built from local propagators and $\Sigma_{\mathbf{k}\nu}^{\text{nlc}}$ represents the contribution of non-local correlations; it may or may not have its own local part.

The *DMFT+ Σ_k* method considers the interaction of electrons via bosonic excitations, which originate from the same fermionic system. *DMFT+ Σ_k* performs an approximate summation of an infinite number of Feynman diagrams (beyond the ladder approximation), which is based on the combinatorial rules for some specific form of the bosonic propagator, relating diagrams of the same order with the corresponding non-crossing diagrams. In particular, assuming that in two dimensions the (spin) static bosonic propagator has the form of a product of one-dimensional propagators,

$$S(\mathbf{Q} + \mathbf{q}) = \Delta^2 \frac{\xi^{-1}}{q_x^2 + \xi^{-2}} \frac{\xi^{-1}}{q_y^2 + \xi^{-2}}, \quad (56)$$

where \mathbf{Q} is the order parameter wave vector, Δ characterizes the strength of the electron-boson interaction, ξ corresponds to the correlation length and the relations $v_{\mathbf{k}}^x v_{\mathbf{k}+\mathbf{Q}}^x > 0$ and $v_{\mathbf{k}}^y v_{\mathbf{k}+\mathbf{Q}}^y > 0$ for the Fermi velocity components $\mathbf{v}_{\mathbf{k}} = (v_{\mathbf{k}}^x, v_{\mathbf{k}}^y)$ are fulfilled, one can show (Kuchinskii and Sadovskii, 1999; Schmalian *et al.*, 1999), that in the static approximation for the bosonic propagator all diagrams of the same order give equal contributions. At $\xi \rightarrow \infty$ the problem can then be mapped to one with a single Gaussian field, while at finite ξ recursion relations for the contribution of the diagrams of different orders can be obtained. In particular, the contribution of the orders $\geq n$ of the perturbation theory to the non-local self-energy are related through (Kuchinskii and Sadovskii, 1999; Sadovskii *et al.*, 2005)

$$\Sigma_{\mathbf{k}\nu}^{\text{nlc}(n)} = \frac{s_n}{\nu - \varepsilon_{\mathbf{k}}^{(n)} + i\nu v_{\mathbf{k}}^{(n)} \xi^{-1} - \Sigma_{\nu}^{\text{loc}} - \Sigma_{\mathbf{k}\nu}^{\text{nlc}(n+1)}}, \quad (57)$$

where s_n are the appropriate combinatorial factors, $\varepsilon_{\mathbf{k}}^{(n)} = \varepsilon_{\mathbf{k}}$, $v_{\mathbf{k}}^{(n)} = |v_{\mathbf{k}}^x| + |v_{\mathbf{k}}^y|$ for odd n , and $\varepsilon_{\mathbf{k}}^{(n)} = \varepsilon_{\mathbf{k}+\mathbf{Q}}$, $v_{\mathbf{k}}^{(n)} = |v_{\mathbf{k}+\mathbf{Q}}^x| + |v_{\mathbf{k}+\mathbf{Q}}^y|$ for even n . The physical non-local part of the self-energy is $\Sigma_{\mathbf{k}\nu}^{\text{nlc}} = \Sigma_{\mathbf{k}\nu}^{\text{nlc}(1)}$, i.e., the final self-energy of the recursion relation Eq. (57). Diagrams of sufficiently high order $N \gg 1$ can be neglected, which provides the initial condition $\Sigma_{\mathbf{k}\nu}^{\text{nlc}(N)} = 0$ for Eq. (57). The above mentioned inequalities $v_{\mathbf{k}}^{x,y} v_{\mathbf{k}+\mathbf{Q}}^{x,y} > 0$ may not be fulfilled for realistic dispersions; the corresponding recursion relations are then only approximate. For the more physical Ornstein-Zernike form of the bosonic propagator near a (quantum) phase transition,

$$S(\mathbf{Q} + \mathbf{q}) = \frac{\Delta^2}{q^2 + \xi^{-2}}, \quad (58)$$

the recursion relations (57) become approximate for any electronic dispersion, and in principle should be replaced by the corresponding integral equations (Katanin, 2005).

An alternative method to augment DMFT with a non-local self-energy is to sample diagrams of the perturbation series contributing to $\Sigma_{\mathbf{k}}^{\text{nlc}}$ using a bold diagrammatic Monte Carlo (BDMC) algorithm (Pollet *et al.*, 2011). The sampling procedure removes the potential bias incurred by choosing a certain class of diagrams in the perturbation theory. In *DMFT+BDMC* the diagrams are constructed in terms of dressed or “bold-line” propagators $G_{\mathbf{k}\nu}$ and bare interaction vertices. Since the propagators contain local self-energy insertions, only skeleton diagrams are sampled up to a given order. Double counting is avoided by requiring that at least two vertices with different site indices and hence at least one non-local propagator are accounted for in $\Sigma_{\mathbf{k}}^{\text{nlc}}$. An improvement of 10^4 in efficiency has been demonstrated for the Anderson localization problem in the non-perturbative regime. For the Hubbard model, however, it has been shown that bold-line diagrammatic series may converge to a wrong answer (Kozik *et al.*, 2015).

In approaches where the resulting $\Sigma_{\mathbf{k}}^{\text{nlloc}}$ has a non-zero local part as in DMFT+ Σ_k and DMFT+BDMC, an external self-consistency is assumed: the local Green's function calculated with the self-energy (55) is used to solve $\Sigma^{\text{loc}} = \Sigma[G^{\text{loc}}]$ —typically through the self-consistent solution of an Anderson impurity model—and the process is iterated until convergence is reached.

In the DMFT+FLEX method (Gukelberger *et al.*, 2015; Kitatani *et al.*, 2015) the summation of the standard ladder and bubble diagrams of the FLEX-type is performed to obtain $\Sigma_{\mathbf{k}\nu}^{\text{nlloc}}$; the local part of these diagrams is subtracted to avoid double counting. This corresponds to the lowest order approximation for the fermionic self-energy (with respect to fermion-boson coupling) in the DMFT+ Σ_k approach, but with the bosonic propagator determined microscopically as a sum of RPA diagrams. The considered set of diagrams is similar to the DGA approach of Sec. III.A below, except that DMFT+FLEX uses the bare vertex in these diagrams instead of a local two-particle irreducible vertex. Let us also note the work by Hage *et al.*, 2004, which supplements the DCA on a small cluster by the FLEX solution on a large cluster.

G. EDMFT++ theories

Many important effects regarding the physics of correlated systems are based on non-local interactions in solids and require a consistent description of collective excitations (plasmons, magnons, orbitons etc.), which can strongly affect the original electronic degrees of freedom. The aim of extended DMFT (EDMFT) (Chitra and Kotliar, 2001; Kajueter, 1996; Si and Smith, 1996; Smith and Si, 2000; Sun and Kotliar, 2002) is to include such non-local interactions and collective (bosonic) degrees of freedom into the DMFT framework. The central quantities of interest in EDMFT are the electronic self-energy and the polarization operator (bosonic self-energy). The latter includes non-local interaction effects and leads to a bosonic or frequency-dependent impurity problem. Akin to DMFT, the fermionic and bosonic self-energies remain purely local. This is often insufficient for describing fluctuations that are inherently non-local in character; for example, EDMFT fails to correctly describe plasmons (Hafermann *et al.*, 2014). Hence, there have been various attempts to include non-local corrections beyond EDMFT. We sum them up under the term EDMFT++ theories. In the following, we focus on diagrammatic EDMFT++ methods, which include the EDMFT+GW approach, the dual boson (DB) approach and the triply-irreducible local expansion (TRILEX). Before that, we recapitulate the EDMFT approach.

From first-principles constrained RPA (Aryasetiawan *et al.*, 2004), one can obtain a frequency dependent non-local interaction for the correlated subspace screened by

broad bands of conduction electrons. The simplest effective action for such an extended Hubbard model reads

$$S = - \sum_{\mathbf{k}\nu\sigma} G_{0,\mathbf{k}\nu}^{-1} c_{\mathbf{k}\nu\sigma}^+ c_{\mathbf{k}\nu\sigma} + \frac{1}{2} \sum_{\mathbf{q}\omega} U_{\mathbf{q}\omega} \rho_{\mathbf{q}\omega}^* \rho_{\mathbf{q}\omega}. \quad (59)$$

Here $G_{\mathbf{k}\nu}^0 = [i\nu + \mu - \varepsilon_{\mathbf{k}}]^{-1}$ is the bare lattice Green's function; the interaction $U_{\mathbf{q}\omega} = U_{\omega} + V_{\mathbf{q}\omega}$ consists of the on-site term U and non-local long-range Coulomb interaction V . For simplicity we consider only charge fluctuations given by the complex bosonic variable $\rho_{\mathbf{q}\omega} = \sum_{\mathbf{k}\nu\sigma} [c_{\mathbf{k}\nu\sigma}^+ c_{(\mathbf{k}+\mathbf{q})(\nu+\omega)\sigma} - \langle c_{\mathbf{k}\nu\sigma}^+ c_{\mathbf{k}\nu\sigma} \rangle \delta_{\omega 0} \delta_{\mathbf{q}0}]$.

In EDMFT, one introduces a local problem of the form

$$S_{\text{loc}} = - \sum_{\nu\sigma} c_{\nu\sigma}^+ [i\nu + \mu - \Delta_{\nu}] c_{\nu\sigma} + \frac{1}{2} \sum_{\omega} \mathcal{U}_{\omega} \rho_{\omega}^* \rho_{\omega}. \quad (60)$$

It can be solved using standard impurity solvers (see Sec. II.D) to obtain the local impurity Green's function G_{ν}^{loc} , susceptibility χ_{ω} and renormalized interaction \mathcal{W}_{ω} defined as follows

$$G_{\nu}^{\text{loc}} = - \langle c_{\nu} c_{\nu}^+ \rangle_{\text{loc}}, \quad (61)$$

$$\chi_{\omega} = - \langle \rho_{\omega} \rho_{\omega}^* \rangle_{\text{loc}}, \quad \mathcal{W}_{\omega} = \mathcal{U}_{\omega} + \mathcal{U}_{\omega} \chi_{\omega} \mathcal{U}_{\omega}. \quad (62)$$

Here the average is taken with respect to the local action (60). In addition to the fermionic hybridization Δ_{ν} , the impurity model contains a bosonic bath Λ_{ω} as part of the local bare interaction $\mathcal{U}_{\omega} = U_{\omega} + \Lambda_{\omega}$. The functions (61), (62) are determined self-consistently in EDMFT. To this end, we first relate G_{ν}^{loc} to a local self energy $\Sigma_{\nu}^{\text{loc}}$ and χ_{ω} to a local polarization operator $\Pi_{\omega}^{\text{loc}} \equiv (\chi_{\omega}^{-1} + \mathcal{U}_{\omega})^{-1}$. With these *local* (fermionic and bosonic) EDMFT self-energies, we calculate the lattice Green's function $G_{\mathbf{k}\nu}^{\text{loc}}$ [as in Eq. 14] and screened interaction $W_{\mathbf{q}\omega}^{\text{loc}}$ according to

$$(G_{\mathbf{k}\nu}^{\text{loc}})^{-1} = (G_{0,\mathbf{k}\nu})^{-1} - \Sigma_{\nu}^{\text{loc}}, \quad (63)$$

$$(W_{\mathbf{q}\omega}^{\text{loc}})^{-1} = (W_{0,\mathbf{q}\omega})^{-1} - \Pi_{\omega}^{\text{loc}}. \quad (64)$$

Here W_0 denotes the bare interaction, which is equal to $U_{\mathbf{q}\omega}$ or $V_{\mathbf{q}\omega}$ in the case of UV - or V -decoupling, respectively (Aryal *et al.*, 2013, 2012). Finally, the local impurity problem is specified through the self-consistency conditions

$$G_{\nu}^{\text{loc}} = \sum_{\mathbf{k}} G_{\mathbf{k}\nu}^{\text{loc}}, \quad \mathcal{W}_{\omega} = \sum_{\mathbf{q}} W_{\mathbf{q}\omega}^{\text{loc}}. \quad (65)$$

An appealing idea is supplementing the local EDMFT fermionic and bosonic self-energies with a non-local part that is obtained within perturbation theory, similar to diagrammatic extensions of DMFT. The separation into local and non-local contributions can be written in the form

$$\Sigma_{\mathbf{k}\nu} = \Sigma_{\nu}^{\text{loc}} + \Sigma_{\mathbf{k}\nu}^{\text{nlloc}}, \quad \Pi_{\mathbf{q}\omega} = \Pi_{\omega}^{\text{loc}} + \Pi_{\mathbf{q}\omega}^{\text{nlloc}}. \quad (66)$$

The goal of EDMFT++ theories is to approximate these nonlocal functions—with EDMFT as a starting point.

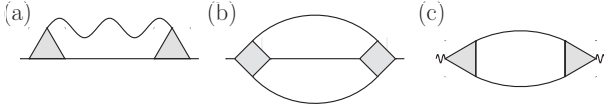


Figure 19 The lowest order non-local self-energy diagrams, treated by the EDMFT+GW method, describing (a) the interaction of the electron with the bosonic mode (wiggly line); (b) the inter-electron interaction; (c) correction to the polarization operator. The yellow (shaded) vertices are taken in the local approximation. Adapted from Ref. [Sun and Kotliar, 2002](#).

1. EDMFT+GW approach

In EDMFT+GW ([Aryal *et al.*, 2013, 2012](#); [Biermann *et al.*, 2003](#); [Hansmann *et al.*, 2013](#); [Huang *et al.*, 2014](#); [Sun and Kotliar, 2002](#); [Tomczak *et al.*, 2012a, 2014](#)), $\tilde{\Sigma}_{\mathbf{k}\nu}$ and $\tilde{\Pi}_{\mathbf{q}\omega}$ are given in terms of second-order diagrams (see Fig. 19). In practice the bare interaction is taken instead of the local vertex. The self-energy and polarization operator diagrams from the GW approximation ([Aryasetiawan and Gunnarsson, 1998](#); [Hedin, 1965, 1999](#)) are added to the dynamical mean-field solution treating non-local correlations. Double counting of the local impurity contributions is efficiently avoided by using only the non-local part of these diagrams. Since the local propagators are equal to those given through the local action (60) by virtue of the self-consistency conditions (65), it is possible to express the GW corrections solely in terms of non-local propagators. The nonlocal parts $\Sigma_{\mathbf{k}\nu}^{\text{nlloc}}$ and $\Pi_{\mathbf{q}\omega}^{\text{nlloc}}$ of the self-energies are correspondingly replaced by

$$\begin{aligned}\Sigma_{\mathbf{k}\nu}^{\text{GW}} &= - \sum_{\mathbf{q}\omega} \tilde{G}_{(\mathbf{k}-\mathbf{q})(\nu-\omega)} \tilde{W}_{\mathbf{q}\omega}, \\ \Pi_{\mathbf{q}\omega}^{\text{GW}} &= 2 \sum_{\mathbf{k}\nu} \tilde{G}_{(\mathbf{k}+\mathbf{q})(\nu+\omega)} \tilde{G}_{\mathbf{k}\nu}.\end{aligned}\quad (67)$$

Here the factor 2 in the second line of Eq. (67) accounts for the spin degeneracy, and the non-local propagators are explicitly given by

$$\tilde{G}_{\mathbf{k}\nu} = G_{\mathbf{k}\nu} - G_{\nu}^{\text{loc}}, \quad \tilde{W}_{\mathbf{q}\omega} = W_{\mathbf{q}\omega} - \mathcal{W}_{\omega}. \quad (68)$$

In this construction, the local interaction U is already been accounted for in the impurity problem. The bare non-local interaction $W_{0,\mathbf{q}\omega}$ enters Eq. (68) through $W_{\mathbf{q}\omega}^{-1} = W_{0,\mathbf{q}\omega}^{-1} - \Pi_{\mathbf{q}\omega}$. For instance, it can be taken in the form of V -decoupling ($W_{0,\mathbf{q}\omega} = V_{\mathbf{q}\omega}$), which leads to a simple separation of local and non-local contributions to the self-energy $\tilde{\Sigma}_{\mathbf{k}\nu}$. Unfortunately, this form of renormalized interaction leads to an overestimation of non-local correlation effects ([Aryal *et al.*, 2013, 2012](#)). On the other hand, the UV -decoupling ($W_{0,\mathbf{q}\omega} = U_{\omega} + V_{\mathbf{q}\omega}$) is more consistent with standard perturbation theory for the full Coulomb interaction, but leads to problems with separation of local and non-local parts of the diagrams ([Stepanov *et al.*, 2016a](#)). A simplified treatment of

the screening using Thomas-Fermi theory has been proposed by [van Roekeghem *et al.*, 2014](#). The form of the renormalized interaction and the way to avoid the double counting in general remain subject to discussion ([Gukelberger *et al.*, 2015](#)).

2. Dual boson (DB) approach

The dual boson (DB) scheme by [Rubtsov *et al.*, 2012](#) aims to treat the action (59) in a similar spirit as the DF approach. Analogously to the DF fields, dual bosonic fields and a corresponding bosonic bath are introduced. These fields decouple non-local interaction terms in models with long-range interactions; the bosonic bath provides an effective treatment of collective excitations.

In the following presentation of the DB method we exclude, for simplicity, exchange interactions and local spin degrees of freedom. They can be included with some care by introducing vector spin bosons ([Aryal and Parcollet, 2015](#)). Moreover, we consider only the single-band case, but a generalization of the formalism to several orbitals or bands is straightforward.

First, completely analogous to the representation Eq. (31) of the lattice action in DF, we rewrite (59) in terms of a local reference action \mathcal{S}_{loc} including a retarded interaction [Eq. (60)] and non-local correction terms:

$$\begin{aligned}\mathcal{S}[c^{\dagger}, c] &= \sum_i \mathcal{S}_{\text{loc}}[c_i^{\dagger}, c_i] + \sum_{\mathbf{k}\nu\sigma} [\varepsilon_{\mathbf{k}} - \Delta_{\nu}] c_{\mathbf{k}\nu\sigma}^{\dagger} c_{\mathbf{k}\nu\sigma} \\ &\quad + \frac{1}{2} \sum_{\mathbf{q}\omega} [U_{\mathbf{q}\omega} - \mathcal{U}_{\omega}] \rho_{\mathbf{q}\omega}^* \rho_{\mathbf{q}\omega}.\end{aligned}\quad (69)$$

The local bare interaction is given by the sum of the local part of the possibly frequency-dependent bare interaction of the lattice model (U_{ω}) and the bosonic bath (Λ_{ω}), i.e., $\mathcal{U}_{\omega} = U_{\omega} + \Lambda_{\omega}$.⁶

In the next step, we decouple the local and non-local degrees of freedom in \mathcal{S} (69) by means of a fermionic (for $\sum_{\mathbf{k}\nu\sigma} [\varepsilon_{\mathbf{k}} - \Delta_{\nu}] c_{\mathbf{k}\nu\sigma}^{\dagger} c_{\mathbf{k}\nu\sigma}$) and a bosonic (for $\frac{1}{2} \sum_{\mathbf{q}\omega} [U_{\mathbf{q}\omega} - \mathcal{U}_{\omega}] \rho_{\mathbf{q}\omega}^* \rho_{\mathbf{q}\omega}$) Hubbard-Stratonovich transformation. The fermionic one is exactly the same as for the DF theory in Eq. (33) which introduces the dual fermionic variables \tilde{c}^{\dagger} and \tilde{c} . The decoupling of the bosonic degrees of freedom is done via the transform

$$\begin{aligned}e^{-\frac{1}{2} [U_{\mathbf{q}\omega} - \mathcal{U}_{\omega}] \rho_{\mathbf{q}\omega}^* \rho_{\mathbf{q}\omega}} &= -\alpha_{\omega}^2 ([U_{\mathbf{q}\omega} - \mathcal{U}_{\omega}]/2)^{-1} \\ &\quad \times \int D[\tilde{\rho}^*, \tilde{\rho}] e^{\alpha_{\omega}^2 ([U_{\mathbf{q}\omega} - \mathcal{U}_{\omega}]/2)^{-1} \tilde{\rho}_{\mathbf{q}\omega}^* \tilde{\rho}_{\mathbf{q}\omega} + \alpha_{\omega} [\rho_{\mathbf{q}\omega}^* \tilde{\rho}_{\mathbf{q}\omega} + \tilde{\rho}_{\mathbf{q}\omega}^* \rho_{\mathbf{q}\omega}]},\end{aligned}\quad (70)$$

⁶ Considering that the full interaction of the lattice system is given by $U_{\mathbf{q}\omega} = U_{\omega} + V_{\mathbf{q}\omega}$ one has $\mathcal{U}_{\omega} - U_{\mathbf{q}\omega} = \Lambda_{\omega} - V_{\mathbf{q}\omega}$, which shows that the method is independent of the selected decoupling scheme (U or UV) ([van Loon *et al.*, 2014b](#)).

where the integration measure $D[\tilde{\rho}^*, \tilde{\rho}] \equiv D\tilde{\rho}^* D\tilde{\rho}/\pi$ includes the normalization factor $1/\pi$, and α_ω is a (for the moment arbitrary) function of ω [cf. $b_{\nu\sigma}$ in DF in Eq. (33)]. The sign in front of $[\mathcal{U}_\omega - U_{\mathbf{q}\omega}]$ within the integral has to be properly chosen in order to guarantee the convergence of the integral (Rubtsov *et al.*, 2012). Alternatively one can employ a decoupling introducing a real field (van Loon *et al.*, 2014b).

The DB action can be written in the form

$$\begin{aligned} \tilde{S}[\tilde{c}^+, \tilde{c}, \tilde{\rho}^*, \tilde{\rho}] = & - \sum_{\mathbf{k}\nu} \tilde{G}_{0,\mathbf{k}\nu}^{-1} \tilde{c}_{\mathbf{k}\nu\sigma}^+ \tilde{c}_{\mathbf{k}\nu\sigma} - \frac{1}{2} \sum_{\mathbf{q}\omega} \tilde{W}_{0,\mathbf{q}\omega}^{-1} \tilde{\rho}_{\mathbf{q}\omega}^* \tilde{\rho}_{\mathbf{q}\omega} \\ & + \sum_i V_{\text{eff}}[\tilde{c}_i^+, \tilde{c}_i, \tilde{\rho}_i^*, \tilde{\rho}_i], \end{aligned} \quad (71)$$

where, similarly to Eq. (68), the bare dual fermion and boson propagators are given by

$$\tilde{G}_{0,\mathbf{k}\nu} = [(G_\nu^{\text{loc}})^{-1} + \Delta_\nu - \varepsilon_{\mathbf{k}}]^{-1} - G_\nu^{\text{loc}} = G_{\mathbf{k}\nu}^{\text{loc}} - G_\nu^{\text{loc}}, \quad (72)$$

$$\tilde{W}_{0,\mathbf{q}\omega} = \alpha_\omega^{-1} [[U_{\mathbf{q}\omega} - \mathcal{U}_\omega]^{-1} - \chi_\omega]^{-1} \alpha_\omega^{-1} = W_{\mathbf{q}\omega}^{\text{loc}} - \mathcal{W}_\omega^{\text{loc}}. \quad (73)$$

For convenience, we choose $\alpha_\omega = \mathcal{W}_\omega/\mathcal{U}_\omega = (1 + \mathcal{U}_\omega\chi_\omega)$ as the local renormalization factor.

The explicit form of the dual interaction V_{eff} is obtained analogously to DF by expanding the c^+ , c -dependent part of the partition function into a series and integrating out these degrees of freedom (ρ^* , ρ are built from c^+ , c). In addition to purely fermionic vertex functions, the result contains also fermion-boson vertices. The corresponding lowest order terms in V_{eff} are given by

$$\begin{aligned} V_{\text{eff}}[\tilde{c}^+, \tilde{c}, \tilde{\rho}^*] = & \sum_{\nu\nu'\omega} \gamma^{\nu\omega} \tilde{c}_{\nu+\omega}^+ \tilde{c}_\nu \tilde{\rho}_\omega^* + \gamma^{\nu'\omega} \tilde{c}_\nu^+ \tilde{c}_{\nu+\omega} \tilde{\rho}_\omega \\ & + \frac{1}{4} \sum_{\nu\nu'\omega} F^{\nu\nu'\omega} \tilde{c}_\nu^+ \tilde{c}_{\nu+\omega} \tilde{c}_{\nu'+\omega}^+ \tilde{c}_{\nu'}. \end{aligned} \quad (74)$$

The spin dependence, which is the same as in Eq. (36), is suppressed for the sake of clarity. The three-point fermion-boson vertex $\gamma^{\nu\omega}$ can be expressed as in TRILEX [Sec.III.G.3] in terms of the original variables of the impurity reference system as (Aryal and Parcollet, 2016a; Rohringer and Toschi, 2016)

$$\gamma^{\nu\omega} = G_\nu^{-1} G_{\nu+\omega}^{-1} \alpha_\omega^{-1} \langle c_\nu c_{\nu+\omega}^+ \rho_\omega \rangle, \quad (75)$$

and the four-point vertex function $F^{\nu\nu'\omega}$ is the same as in the DF theory [Eq. (36)]. Further, the renormalized dual propagators, i.e., the dual Green's function $\tilde{G}_{\mathbf{k}\nu} = -\langle \tilde{c}_{\mathbf{k}\nu} \tilde{c}_{\mathbf{k}\nu}^+ \rangle$ and the screened dual interaction $\tilde{W}_{\mathbf{q}\omega} = -\langle \tilde{\rho}_{\mathbf{q}\omega} \tilde{\rho}_{\mathbf{q}\omega}^* \rangle$, as well as the dual self-energy $\tilde{\Sigma}_{\mathbf{k}\nu}$ and polarization operator $\tilde{\Pi}_{\mathbf{q}\omega}$, can be constructed from these building blocks diagrammatically (van Loon *et al.*, 2014b; Rubtsov *et al.*, 2012; Stepanov *et al.*, 2016b), see

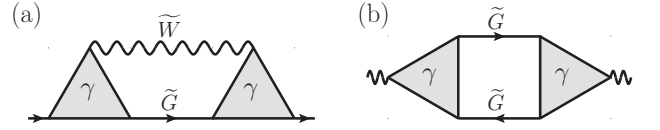


Figure 20 Second-order diagrams contributing to the non-local (a) fermionic and (b) bosonic DB self-energy, i.e., to $\tilde{\Sigma}_{\mathbf{k}\nu\sigma}$ and $\tilde{\Pi}_{\mathbf{q}\omega}$, respectively.

Fig. 20. The free dual boson propagators correspond to the EDMFT approximation. The physical Green's function $G_{\mathbf{k}\nu}$ and the renormalized interaction $W_{\mathbf{q}\omega}$ of the original model can be expressed in terms of the dual quantities as follows:

$$G_{\mathbf{k}\nu}^{-1} = (G_{\mathbf{k}\nu}^{\text{loc}})^{-1} - \tilde{\Sigma}_{\mathbf{k}\nu} (1 + G_\nu^{\text{loc}} \tilde{\Sigma}_{\mathbf{k}\nu})^{-1}, \quad (76)$$

$$W_{\mathbf{q}\omega}^{-1} = (W_{\mathbf{q}\omega}^{\text{loc}})^{-1} - \tilde{\Pi}_{\mathbf{q}\omega} (1 + \mathcal{W}_\omega^{\text{loc}} \tilde{\Pi}_{\mathbf{q}\omega})^{-1}. \quad (77)$$

The fermionic and bosonic bath can be taken from a converged EDMFT calculation or can be determined self-consistently within DB theory. The latter is possible by via the EDMFT self-consistency conditions (65) but also other conditions are discussed (Stepanov *et al.*, 2016b). The dual polarization operator $\tilde{\Pi}_{\mathbf{q}\omega}$ can, e.g., be chosen as the sum of ladder diagrams (Hafermann *et al.*, 2014; van Loon *et al.*, 2014a,b; Stepanov *et al.*, 2016b):

$$\tilde{\Pi}_{\mathbf{q}\omega} = \sum_{\nu\nu'} \gamma^{(\nu+\omega)-\omega} \tilde{\chi}_{\mathbf{q}}^{\nu\omega} \left[I + F^{\nu\nu'\omega} \tilde{\chi}_{\mathbf{q}}^{\nu'\omega} \right]_{\nu\nu'}^{-1} \gamma^{\nu'\omega}, \quad (78)$$

where $\tilde{\chi}_{\mathbf{q}}^{\nu\omega} = \sum_{\mathbf{k}} \tilde{G}_{\mathbf{k}}(\nu) \tilde{G}_{\mathbf{k}+\mathbf{q}}(\nu + \omega)$.

Using ladder diagrams within the DB approach (Hafermann *et al.*, 2014; van Loon *et al.*, 2014a,b), one obtains the following physical (lattice) susceptibility for the extended Hubbard model (see Stepanov *et al.*, 2016b who used X instead of χ):

$$\chi_{\mathbf{q}\omega} = \frac{1}{1/\Pi_{\mathbf{q}\omega}^{(1)} + \Lambda_\omega - V_{\mathbf{q}\omega}}, \quad (79)$$

where $\Pi_{\mathbf{q}\omega}^{(1)} = (\chi_\omega + \chi_\omega \tilde{\Pi}_{\mathbf{q}\omega} \chi_\omega)$. This physical susceptibility fulfills the important property of charge conservation, $\lim_{\mathbf{q} \rightarrow \mathbf{0}} \chi_{\mathbf{q}\omega \neq 0} = 0$, see Hafermann *et al.*, 2014, Stepanov *et al.*, 2016b.

Eq. (79) also allows us to make a close connection to the Moriya λ -correction in ladder DfA [Sec. III.A.2]. When the interaction is local and non-local effects from the self-energy on the internal fermionic lines are neglected, Hafermann *et al.*, 2014 showed that $\Pi_{\mathbf{q}\omega}^{(1)}$ is equivalent to the DMFT susceptibility. Hence with $V_{\mathbf{q}\omega} = 0$, the ladder DB susceptibility (79) equals that of ladder DfA if the DfA Moriya λ -correction is taken frequency dependent and equal to the DB Λ_ω .

Let us also note that the Λ_ω in the susceptibility (79) allows us to restore a property that is broken in DMFT

(with $\Lambda_\omega = 0$), namely that the double occupation calculated from the susceptibility of the impurity problem equals that calculated from the susceptibility of the lattice problem. The DB double occupancy is closer to DCA benchmarks than either DMFT result (van Loon *et al.*, 2016b). The momentum dependence of the polarization operator introduced in DB is important for a thermodynamically consistent response of the charge response (van Loon *et al.*, 2015a). More applications of the dual boson approach are discussed in Sec. IV.E.

3. TRILEX approach

The physical motivation for the triply irreducible local expansion (TRILEX) scheme by Ayril and Parcollet, 2015, 2016a is to include both Mott and spin-fluctuation physics (long-range bosonic modes), which are thought to be essential ingredients to describe high-temperature superconductivity (Dagotto, 1994). It is based on a similar functional construction as QUADILEX [Sec. III.A.4], but now based on the functional \mathcal{K}_3 , which contains all 3/2-particle irreducible diagrams (De Dominicis and Martin, 1964a), corresponding to three Green's function legs. The TRILEX approximation restricts these diagrams to the local ones, i.e., approximates \mathcal{K}_3 by its local counterpart (Ayril and Parcollet, 2016a)

$$\mathcal{K}_3[G_{\mathbf{k}\nu}, W_{\mathbf{q}\omega}, \chi_{\mathbf{k}\mathbf{q}}^{\nu\omega}] \approx \mathcal{K}_3[G_\nu, W_\omega, \chi^{\nu\omega}]. \quad (80)$$

In addition to G and W , \mathcal{K}_3 is also a functional of the three-point electron-boson correlation function χ , which should not be confused with the local susceptibility. As in EDMFT, the functional (80) can be obtained from a self-consistently determined quantum impurity model which now includes a dynamical electron-boson coupling $\lambda_{\nu\omega}$ related to χ .

In the general framework, the fermionic and bosonic self-energies are given by the Hedin, 1965 equations

$$\begin{aligned} \Sigma_{\mathbf{k}\nu} &= - \sum_{\mathbf{q}\omega} G_{(\mathbf{k}-\mathbf{q})(\nu-\omega)} W_{\mathbf{q}\omega} \gamma_{\mathbf{k}\mathbf{q}}^{\nu\omega} = \text{diagram with wavy line and red triangle}, \\ \Pi_{\mathbf{q}\omega} &= 2 \sum_{\mathbf{k}\nu} G_{(\mathbf{k}+\mathbf{q})(\nu+\omega)} G_{\mathbf{k}\nu} \gamma_{\mathbf{k}\mathbf{q}}^{\nu\omega} = \text{diagram with two wavy lines and red triangle}, \end{aligned} \quad (81)$$

where $\gamma_{\mathbf{k}\mathbf{q}}^{\nu\omega}$ is the exact three-point lattice vertex. Ayril and Parcollet, 2015 approximate this quantity by its local counterpart: $\gamma_{\mathbf{k}\mathbf{q}}^{\nu\omega} \approx \gamma^{\nu\omega}$. This vertex is computationally easier to handle than most diagrammatic extensions discussed in this review, because $\gamma^{\nu\omega}$ depends on only two instead of three independent frequencies. TRILEX has some similarity to EDMFT+ GW , but the non-local GW diagrams are now additionally dressed by $\gamma^{\nu\omega}$.

The application of the formalism to a purely fermionic model such as the Hubbard model requires the introduction of bosonic fields. To this end, the Coulomb interac-

tion is (arbitrarily) decomposed into one or more channels (charge and spin in x, y, z direction). By construction, the method interpolates for the charge channel between the GW approximation at weak coupling and the atomic limit at strong coupling. It yields Fermi arcs, spin fluctuations, and a reduction of the mean-field critical temperature (to what extent depends on the chosen decoupling), but overestimates the critical U of the Mott transition (Ayril and Parcollet, 2016a).

One may speculate that TRILEX underestimates spatial correlations because a local approximation to the three-leg vertex is more restrictive. Indeed, DFA has been formulated also in form of a three leg vertex similar to Eq. (81), see Katanin *et al.*, 2009. But in DFA $\gamma_{\mathbf{k}\mathbf{q}}^{\nu\omega}$ is obtained from the BSE ladder [Eq. (21)] constructed from the local two-particle (four leg) vertex $\Gamma_{ph,r}^{\nu\nu'\omega}$ and is \mathbf{q} -dependent (non-local).

There are also apparent similarities between the TRILEX and DB approaches. Both introduce bosonic modes. But while in TRILEX the local three-leg vertex of the impurity model enters the calculation and the two-particle polarization is included through Eq. (81), in DB the local four-leg susceptibility directly enters the calculation. One can reshuffle the DB diagrams into a form with a three-leg vertex as in Eq. (81). This DB three-leg vertex then includes the non-local \tilde{W} and \tilde{G} of DB and is again non-local.

IV. APPLICATIONS AND RESULTS

A. Hubbard Model

The Hubbard model is arguably the most fundamental model for strongly correlated electrons. Let us recall its Hamiltonian, Eq. (12):

$$\mathcal{H} = \sum_{ij,\sigma} t_{ij} c_{i\sigma}^\dagger c_{j\sigma} + U \sum_i n_{i\uparrow} n_{i\downarrow}, \quad (82)$$

with hopping amplitude t_{ij} and local Coulomb repulsion U . The model provides the basic physical description of the Mott-Hubbard metal-insulator transitions (MIT) in bulk 3d systems (Gebhard, 1997; Imada *et al.*, 1998) as well as of ferro- (Mielke and Tasaki, 1993; Vollhardt *et al.*, 1998) and antiferromagnetism (Jarrell, 1992). In 2d, the Hubbard model (82) is believed to capture the low-energy physics of the superconducting cuprates (Dagotto, 1994; Scalapino, 2012). Therefore the cases of 3d and 2d are of particular interest. Despite its formal simplicity, an exact solution is known only in 1d through the Bethe ansatz (Lieb and Wu, 1968) and through DMFT in the limit of infinite dimensions (Georges *et al.*, 1996; Metzner and Vollhardt, 1989).

In this section, we summarize the unified picture of the Hubbard model physics in finite dimensions as it

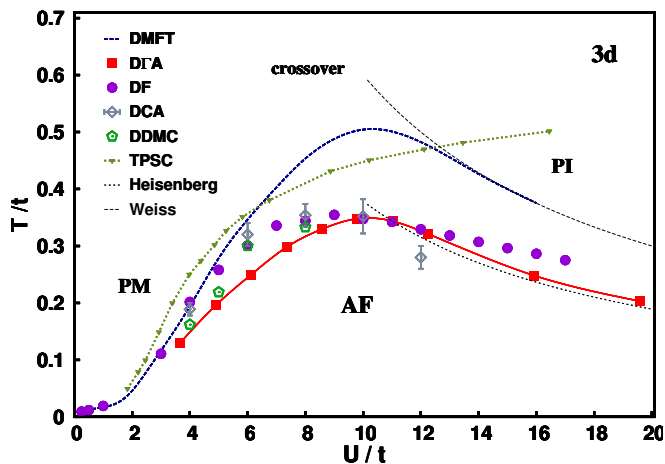


Figure 21 (Color online) Phase-diagram of the half-filled Hubbard model in $3d$ with nearest neighbor hopping ($t_{ij} = -t$), as obtained by various methods, see text.

emerges from the applications of diagrammatic extensions of DMFT; we compare the results to those of other methods, wherever available. Given that the starting point of diagrammatic extensions is a DMFT solution, we first consider the $3d$ system, which can be regarded as “closer” to the physics of $d = \infty$. We then subsequently lower the dimension so that deviations from DMFT become progressively larger.

1. Three dimensions

The magnetic phase diagram of the unfrustrated $3d$ Hubbard model at half filling, obtained by several approaches, is shown in Fig. 21. At high T , the model shows a crossover from a paramagnetic metal (PM) at weak coupling to a paramagnetic insulator (PI) at strong coupling. As the temperature is lowered, the model undergoes a second-order transition to an AF state, see [Georges *et al.*, 1996](#) and [Kent *et al.*, 2005](#) for the DMFT phase diagram. Non-local corrections beyond DMFT have been analyzed using DGA ([Rohringer *et al.*, 2011](#)) and DF ([Hirschmeier *et al.*, 2015](#)) in the ladder approximation. The two approaches yield a rather coherent picture of the underlying physics, both for the magnetic transition and its critical properties.

In particular, DGA and DF correctly predict a sizable reduction of the Néel temperature T_N w.r.t. DMFT in Fig. 21, which is a direct consequence of non-local spin fluctuations. The ratio of the reduction is, as expected, smaller at weak-coupling ([Schauerte and van Dongen, 2002](#)), and larger (more than 30%) at intermediate to strong coupling. Notably, T_N from DGA correctly approaches the behavior of the Heisenberg model ([Sandvik, 1998a](#)) in the strong coupling limit. This is a significant improvement over DMFT which approaches the

Weiss mean-field theory of the Heisenberg model ([Takahashi, 1977](#)) in this limit. It also improves over the two-particle selfconsistent theory (TPSC) ([Vilk and Tremblay, 1997](#)) which reaches a plateau for T_N at large U . Moreover, in the most interesting regime of intermediate coupling $8t \lesssim U \lesssim 12t$, both methods agree remarkably well with the DCA results by [Kent *et al.*, 2005](#) and diagrammatic determinant Monte Carlo (DDMC) by [Kozik *et al.*, 2013](#) – in spite of the intrinsic differences between these methods. Minor quantitative deviations between DF and DGA are only observed in the weak- and strong-coupling limits. At weak coupling, DGA has a smaller T_N than DF, DCA ([Kent *et al.*, 2005](#)), TPSC ([Daré and Albinet, 2000](#)) and perturbation theory ([Schauerte and van Dongen, 2002](#)). On the other hand, it yields a result that is closer to latest DDMC by [Kozik *et al.*, 2013](#) which prevents a final judgment regarding the accuracy of the different approximations in this parameter regime. In the opposite limit, DF overestimates T_N ([Hirschmeier *et al.*, 2015](#)). We suspect that this result is not intrinsic to the method, but either due to the hybridization not being computed self-consistently, or because the vertex function was computed at a single bosonic frequency. The latter approximation is sufficient to investigate critical behavior, but it can affect non-universal quantities such as T_N .

Diagrammatic extensions faithfully reproduce the universal critical behavior of the $3d$ Hubbard model ([Hirschmeier *et al.*, 2015](#); [Rohringer *et al.*, 2011](#)). Results for the critical exponents γ and ν governing the T -dependence of the diverging susceptibility (χ_{AF}) and correlation length (ξ), respectively, are shown in Fig. 22. They differ significantly from the mean-field exponents obtained within the DMFT description. Within the present numerical precision, the DF and DGA critical exponents are compatible with the universality class of the $3d$ Heisenberg model ([Holm and Janke, 1993](#)) and with the scaling relation $\gamma/\nu = 2 - \eta$ (the exponent η is small and could not yet be precisely extracted). This result is expected, as the Hubbard model maps onto the Heisenberg model in the strong coupling regime, and the dimension and symmetry of the AF order parameter suggest the same universality class.

Let us emphasize that the diagrammatic extensions of DMFT are able to describe the critical behavior because they accurately capture spatial fluctuations over large length scales. The effects of these fluctuations show up also in other quantities such as spectral functions ([Fuchs *et al.*, 2011](#); [Katanin *et al.*, 2009](#); [Rohringer and Toschi, 2016](#); [Rohringer *et al.*, 2011](#)) as well as in thermodynamic ([Rohringer and Toschi, 2016](#)) and transport properties ([Gull *et al.*, 2011b](#)). This can be seen, e.g., in the T -dependence of the electronic scattering rate, defined as $\gamma_{\mathbf{k}} = -\text{Im} \Sigma(\mathbf{k}, \omega = 0)$. Fig. 23 shows results for $\gamma_{\mathbf{k}}$ in DMFT and DGA ([Rohringer and Toschi, 2016](#)) for an intermediate U value. In DMFT the scattering rate de-

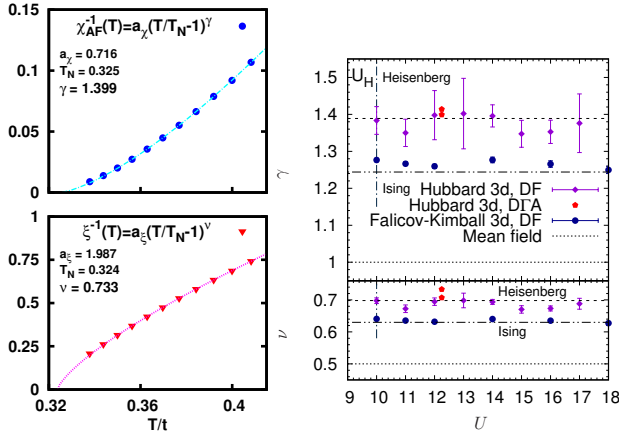


Figure 22 (Color online) Left panels: DGA inverse AF susceptibility χ_{AF}^{-1} (top) and inverse correlation length ξ^{-1} (bottom) for the 3d Hubbard model at half-filling and $U \approx 12.2t$. The corresponding critical exponents γ and ν are obtained by the fit shown (adapted from Rohringer *et al.*, 2011). Right panel: Critical exponents obtained within DF at different U compared to the DGA result from the left panels, and a second fit to estimate the error. DF results for the Falicov-Kimball model and the mean-field critical exponents are shown for comparison (adapted from Hirschmeier *et al.*, 2015).

creases monotonously with decreasing T , as expected for a Fermi liquid. Instead the DGA results show a non-monotonous behavior of $\gamma_{\mathbf{k}}$ with a minimum of the scattering rate at intermediate T . That is, as the phase transition is approached, $\gamma_{\mathbf{k}}$ increases due to the enhanced scattering at non-local spin fluctuations. An analogous behavior is predicted at weak-coupling by TPSC (Vilk and Tremblay, 1997) with the significant difference that $\gamma_{\mathbf{k}}$ diverges (logarithmically) at T_N while in DGA such a singularity is cut-off by the local quasi-particle scattering rate of DMFT (Rohringer and Toschi, 2016). This demonstrates that the inclusion of DMFT physics qualitatively modifies the results obtained by perturbative

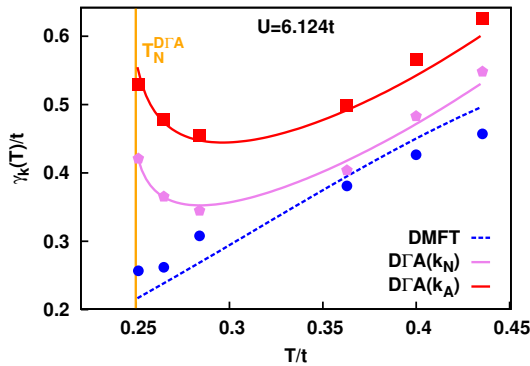


Figure 23 (Color online) Scattering rates $\gamma_{\mathbf{k}}$ at the nodal $\mathbf{k}_N = (\pi/2, \pi/2, \pi/2)$ and antinodal $\mathbf{k}_A = (0, \pi/2, \pi)$ points in the 3d Hubbard model as obtained by DGA. Adapted from Rohringer and Toschi, 2016.

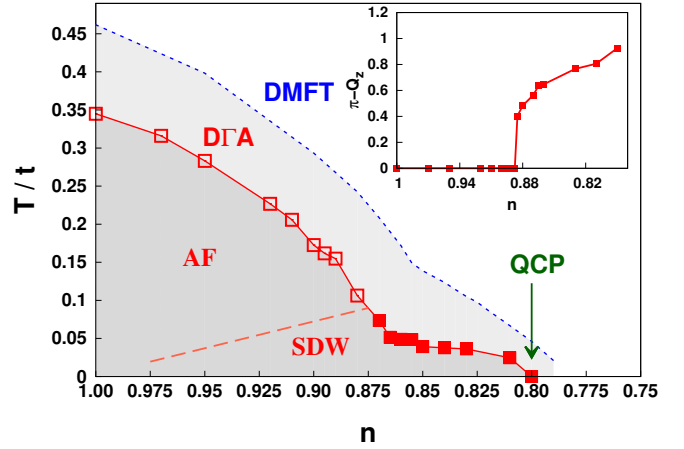


Figure 24 (Color online) Magnetic phase diagram of the 3d Hubbard model as a function of filling n and T at fixed $U = 9.78t$. DGA shows a transition from commensurate (open squares, AF) to incommensurate ordering (filled square, SDW) as well as the emergence of a quantum critical point at $n \sim 0.8$. Inset: Degree of incommensurability vs. n . Adapted from Schäfer *et al.*, 2016b.

approaches even at weak-coupling.

Motivated by the ability to describe the non-trivial physics of the finite- T magnetic transition in the particle-hole symmetric case, first calculations away from half filling have been recently performed in 3d within DGA by Schäfer *et al.*, 2016b. Beyond the extension of the magnetic phase-diagram in 3d, the main interest here lies in the occurrence of a quantum critical point (QCP), see Fig. 24. By progressively decreasing the electronic density n at a fixed $U \simeq 10t$, one finds that: (i) T_N is progressively reduced; (ii) the AF pattern becomes incommensurate with an ordering vector $\mathbf{Q} = (\pi, \pi, \pi - Q_z)$; and (iii) a QCP eventually emerges at about 20% of hole-doping. The DGA and analytical calculations in Schäfer *et al.*, 2016b further show how the corresponding quantum critical properties are driven by Fermi-surface features (specifically by lines of Kohn points in the present case). These properties yield quite different exponents and scaling relations ($\nu = 1, \gamma = 0.5$) compared to those predicted by conventional Hertz-Millis-Moriya theory (where $\nu = 0.75, \gamma = 1.5$, see e.g. von Löhneysen *et al.*, 2007).

2. Two dimensions: square lattice at half filling

The two-dimensional case poses a stringent test on diagrammatic extensions of DMFT, for two reasons: As a consequence of the theorem by Mermin and Wagner, 1966, continuous symmetries cannot be spontaneously broken in 2d at a finite temperature in systems with short-range interaction. This means that (i) diagrammatic extensions have to account for fluctuations at all

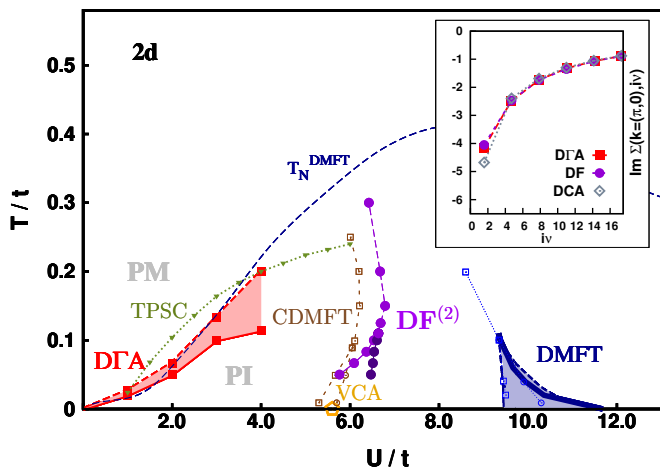


Figure 25 (Color online) Phase diagram of the square lattice $2d$ Hubbard model at half-filling as obtained by various methods, see text. The finite DMFT Néel temperature is also given for reference (blue line). Inset: Comparison of the self-energy at the antinodal point for $U/t=8$, $T/t=0.5$; from LeBlanc *et al.*, 2015

length scales, because they are essential for the proof of the theorem, and (ii) the physics of the DMFT starting point is qualitatively incorrect because it predicts a finite temperature mean-field transition to the AF ordered state.

Cluster calculations struggle to account for long-range fluctuations and are hampered by the sign problem away from half filling. Diagrammatic extensions therefore provide a valuable complementary viewpoint, and fulfill the Mermin-Wagner theorem (Katanin *et al.*, 2009). These methods have mainly been applied to the square and frustrated triangular lattices. Because these give rise to rather different physics, we review them separately.

Metal-insulator transition The occurrence of a MIT in the phase-diagram of the $2d$ Hubbard model, together with its physical interpretation, has been intensely debated in the literature since the 70's (Anderson, 1997; Avella *et al.*, 2001; Castellani *et al.*, 1979; Vekić and White, 1993; Mancini, 2000; Montorsi, 1992; Moukouri *et al.*, 2000; Vilks and Tremblay, 1996, 1997). There is general consensus about the AF-ordering of the ground state, which smoothly evolves from a nesting-driven (Slater) to a superexchange-driven (Heisenberg) AF-insulator with increasing U . In the Heisenberg limit, we have effective spin degrees of freedom coupled by the exchange interaction $J = 4t^2/U$ governing the low-energy physics. In the view of Anderson, 1997, the $2d$ Hubbard physics would always be similar to $1d$ and, thus, intrinsically non-perturbative, with a gap present for all $U > 0$: Localized moments would form at sufficiently low-temperatures, open a spectral gap, and, finally order at $T = 0$.

We discuss the phase diagram shown in Fig. 25 in view

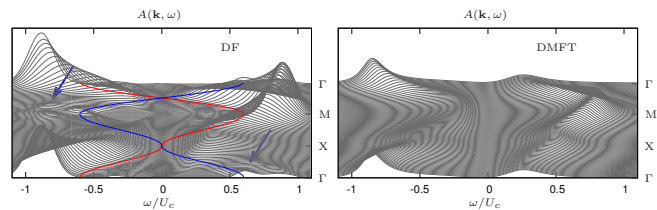


Figure 26 (Color online) Spectral function $A(\mathbf{k}, \omega)$ in $DF^{(2)}$ (left) and DMFT (right) at $T = 0.22$ for $U = 7$ and $U = 10$, respectively. The frequency has been rescaled by the respective critical U_c , which is finite $U_c = 6.64t$ for $DF^{(2)}$ and $U_c = 9.35t$ for DMFT. Colored lines show the bare dispersion $\varepsilon_{\mathbf{k}}$ (red) and $\varepsilon_{\mathbf{k}+\mathbf{Q}} = -\varepsilon_{\mathbf{k}}$ (blue) with $\mathbf{Q} = (\pi, \pi)$, which corresponds to a folding of the band at the effective magnetic zone boundary. The structures marked by arrows arise from dynamical short-range antiferromagnetic correlations captured in $DF^{(2)}$. From Brener *et al.*, 2008.

of this background, starting from the purely local description of DMFT, and adding the effect of non-local correlations over progressively larger length scales. In DMFT, by enforcing the PM solution, one finds the well-known first-order Mott MIT (with associated coexistence region, see Georges *et al.*, 1996), ending with a second-order critical endpoint at $U_c \simeq 10t$ (taken from Blümer, 2002 and Park *et al.*, 2008). The low- T Mott PI is characterized by independent spin-1/2 magnetic moments with a high residual entropy of $\log 2$ per site. As a result the transition line in Fig. 25 has a negative slope.

When short-range (AF) correlations between the moments are included, as in CDMFT (Park *et al.*, 2008),⁷ VCA (Schäfer *et al.*, 2015a), or second-order DF ($DF^{(2)}$; Hafermann, 2010), several changes are observed in Fig. 25: (i) U_c is considerably reduced, (ii) the width of the coexistence region shrinks, and (iii) the entropy of the PI phase is strongly reduced, so that the slope of the transition line is reversed.

If also long-range AF fluctuations are included as in ladder DFA, extrapolated lattice QMC (Schäfer *et al.*, 2015a), ladder DF (Hafermann, 2016) and TPSC (Vilks and Tremblay, 1996, 1997), the MIT is shifted to very small U values, compatible with $U_c = 0$ for $T \rightarrow 0$ (red-colored region in Fig. 25).

Physical observables and interpretation While at high T and large U the results for the one-particle self-energy (and spectral function) of DFA and DF are very similar to those of cluster methods (DCA), see inset of Fig. 25 (LeBlanc *et al.*, 2015), a more detailed discussion

⁷ Cf. further CMDFT (Fratino *et al.*, 2017) and DCA calculations (Merino and Gunnarsson, 2014; Moukouri and Jarrell, 2001; Werner, 2013) which are not shown in Fig. 25 and indicate a reduction of U_c with increasing cluster size.

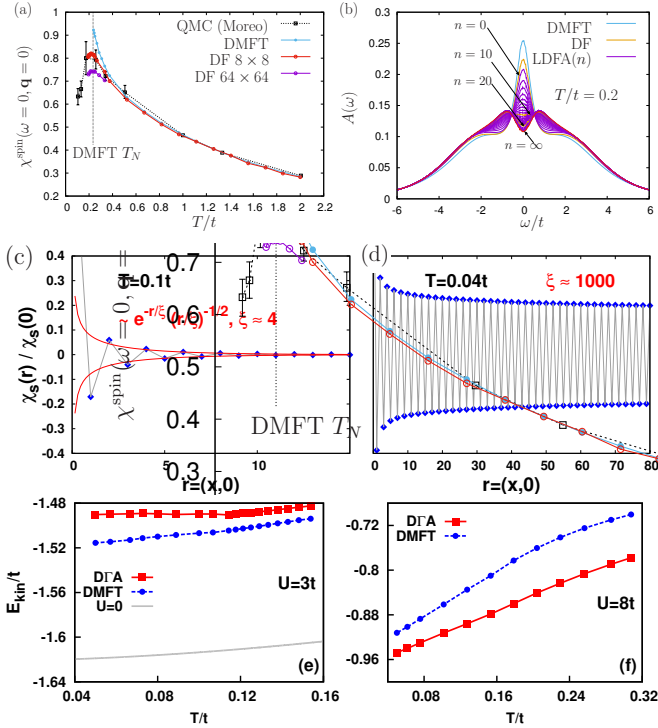


Figure 27 (Color online) (a) T -dependence of the ferromagnetic susceptibility for $U = 4t$ in DMFT, lattice QMC (Moreo, 1993) for an 8×8 lattice, and ladder DF for an 8×8 and 64×64 lattice. (b) Ladder DF local spectrum $A(\omega)$ at $T/t = 0.2$ including ladder diagrams up to order $n + 2$ in the vertex F ($n = 0$ corresponds to $\text{DF}^{(2)}$) (Hafermann, 2010). (c,d) Real space spin-susceptibility χ_s computed in ladder DGA for $U = 2t$ in the PM ($T = 0.1t$, c) and in the PI phase ($T = 0.04t$, d). (e,f) Kinetic energy of the $2d$ Hubbard model at (e) $U = 3t$ and (f) $U/t = 8$ (Rohringer and Toschi, 2016).

is necessary at low temperatures. In particular, we start by noting that in second-order $\text{DF}^{(2)}$, the diagrammatic contributions decay rapidly in real space. Fig. 26 shows the second-order $\text{DF}^{(2)}$ results for the spectral function which demonstrates how short-range correlations affect this quantity compared to DMFT: At relatively large U -values, just above the Mott transition point, broad spectral structures appear in the vicinity of the Γ -point. Brener *et al.*, 2008 attribute these “shadow bands” (akin to the red and blue dispersion in Fig. 26) to short-ranged dynamical AF correlations.

In the weak-coupling regime, complementary ladder DF and DGA results allow us to draw a clear-cut picture. First we observe that the T -dependence of the uniform magnetic susceptibility computed in ladder DF in Fig. 27 (a) displays a downturn in the vicinity of T_N^{DMFT} (Hafermann, 2016; LeBlanc *et al.*, 2017). This temperature approximately marks the onset of the PI phase, below which AF fluctuations become particularly strong and a pseudogap develops (Rost *et al.*, 2012), as can also be seen in Fig. 27 (b). The downturn is absent in DMFT and DCA (LeBlanc *et al.*, 2017) but well matches

lattice QMC results (Moreo, 1993), which shows that extended AF fluctuations govern the physics in this regime and reduce the FM susceptibility. As is evident from Fig. 27 (b), only high-order diagrams ($n \gg 2$) in the ladder expansion can describe such long-range fluctuations. By contrast, the second-order calculation does not include long-range correlations: there is no pseudogap in $\text{DF}^{(2)}$ in Fig. 27 (b), there are only very weak finite size effects in the susceptibility (Brener *et al.*, 2008; Li *et al.*, 2008), and U_c of the MIT is finite. The importance of long-range AF fluctuations also in the intermediate coupling regime is confirmed by extracting the magnon dispersion from ladder DF, which matches available inelastic neutron scattering data for La_2CuO_4 (LeBlanc *et al.*, 2017).

The DGA results for the spin-susceptibility in real-space confirm this picture, see Fig. 27 (c,d): In the weak-coupling regime it shows the typical AF oscillation pattern. At high temperatures in the PM phase (c), it decays over a short length scale ξ of a few lattice spacings ($\xi \simeq 4$). The onset of PI behavior is instead associated with a huge increase of ξ to about $\xi \simeq 1000$ (d). We thus conclude that the weaker the coupling, the larger the length scale of the AF fluctuations that is needed to open the spectral gap. Consistent with the TPSC approach by Vilk and Tremblay, 1996, 1997, the PI behavior for small U emerges in the low-temperature regime, where ξ (Rohringer and Toschi, 2016; Schäfer *et al.*, 2015a) and the susceptibility (Otsuki *et al.*, 2014) grow exponentially with $1/T$, as required by the Mermin-Wagner theorem.

Fig. 27 (f) shows that at strong coupling $U = 8t$ antiferromagnetic fluctuations in DGA lead to a kinetic energy gain in comparison with the PM DMFT solution. This is in agreement with the Heisenberg picture where it corresponds to a gain of superexchange energy. By contrast, at weak coupling $U = 3t$ as in Fig. 27 (e), the DGA kinetic energy is smaller (in absolute value) than the DMFT one. Here, we have, however, a gain of potential energy due to antiferromagnetic fluctuations, as in a Slater antiferromagnet (Rohringer and Toschi, 2016). This demonstrates that in the paramagnetic phase the AF fluctuations evolve gradually from Slater to Heisenberg paramagnons with increasing U , reflecting the properties of the underlying ground state.

Pseudogaps and the formation of Fermi-arcs, i.e., the destruction of quasi-particles near the antinodal region, has been reproduced by various flavors of diagrammatic extensions, including ladder DF (Rubtsov *et al.*, 2009), DGA (Katanin *et al.*, 2009), DMF^2RG (Taranto *et al.*, 2014) and TRILEX (Aryal and Parcollet, 2015).

Fig. 28 shows the self-energy as well as the momentum-resolved spectral functions in the pseudogap regime. Fig. 28 (c)-(e) reveals that the Fermi surface is fully gapped both in variational DF (Jung, 2010) and lattice QMC extrapolated to the thermodynamic limit; for related pseudogaps in $\text{DMFT} + \Sigma_k$ see Nekrasov *et al.*, 2008,

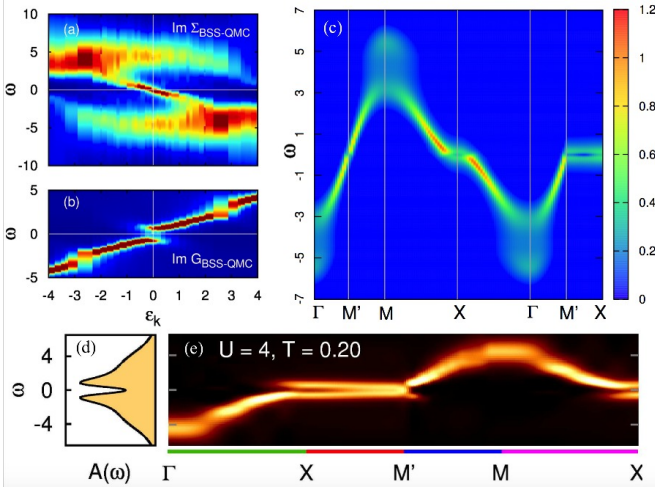


Figure 28 (Color online) (a) Self-energy and (b) Green's function vs. energy-momentum dispersion ϵ_k as obtained within lattice QMC (from Pudleiner *et al.*, 2016). (c) Momentum resolved spectral function within variational DF (from Jung, 2010) and (e) lattice QMC (from Rost *et al.*, 2012) along the high-symmetry lines of the Brillouin zone. (d) A pseudogap is visible in QMC at the Fermi surface; the DF spectral function also exhibits a waterfall. All panels are for the 2D Hubbard model at $U = 4t$, $T \approx 0.2t$, and half filling.

2011 for DGA see Katanin *et al.*, 2009 and Rohringer and Toschi, 2016. The opening of the pseudogap is reflected in a transition from a z shape to an inverse z -shape structure in the self-energy, see Fig. 28 (a) and Pudleiner *et al.*, 2016. It is also connected to zeros in the Green function (Sakai *et al.*, 2009). The lattice QMC calculations of Fig. 28 (a) and DGA also show that, except for the pseudogap itself, the (k_x, k_y) dependence of the self-energy can be expressed by a single parameter: the energy-momentum dispersion $\varepsilon_{(k_x, k_y)}$.

Taken together, DGA and DF are compatible in the regimes of their applicability, with lattice QMC, TPSC and cluster extensions of DMFT and yield the following physics: With decreasing T , a pseudogap opens due to AF fluctuations first in the anti-nodal and then in the nodal direction (Schäfer *et al.*, 2016c) marking the MIT of Fig. 25. For the square lattice with perfect nesting this happens at arbitrarily small interaction U .

3. Two dimensions: square lattice off half-filling

At finite doping, studies of superconductivity in the Hubbard model are of primary interest. In this respect, the arguably biggest success of cluster DMFT and DCA calculations has been the observation of superconductivity (Capone and Kotliar, 2006; Gull *et al.*, 2013; Lichtenstein and Katsnelson, 2000; Maier *et al.*, 2005b) which helped establishing the presence of superconductivity in the Hubbard model. Superconductivity requires a frame-

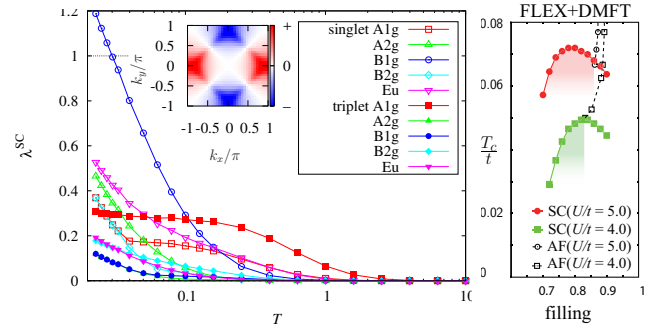


Figure 29 (Color online) Left: Temperature dependence of the leading eigenvalue in the particle-particle channel for the hole-doped 2d Hubbard model in DF at $U/t = 8$ and 14% hole doping, separated into contributions for given symmetry. The eigenvalue associated with singlet B_{1g} symmetry crosses 1, implying a transition to the superconducting state. The inset shows the momentum dependence of the eigenfunction $\phi_{\mathbf{k}}(\omega_0)$ corresponding to this eigenvalue at $T = 0.1$, with apparent d -wave symmetry. From Otsuki *et al.*, 2014. Right: Superconducting and antiferromagnetic critical temperature vs. electron filling in FLEX+DMFT. From Kitatani *et al.*, 2015.

work which captures both strong local dynamical correlations and spatial fluctuations, as offered by diagrammatic extensions of DMFT. In DF, the effective pairing interaction has been constructed similarly as in FLEX, namely by inserting the ladder diagrams of the horizontal and vertical particle-hole channels (see Sec. III.B) into the irreducible particle-particle vertex $\Gamma_{pp,\alpha,\mathbf{k}\mathbf{k}'\mathbf{q}}^{\nu\nu'\omega}$ (Hafermann *et al.*, 2009b; Otsuki *et al.*, 2014). The former incorporates the charge, as well as the longitudinal and transverse spin fluctuations that are expected to be predominant at moderate hole-doping (Gunnarsson *et al.*, 2015, 2016). The transition temperature is found by computing the leading eigenvalue of a linearized Eliashberg-like equation,

$$\sum_{\mathbf{k}\omega} \Gamma_{pp,r,\mathbf{k}\mathbf{k}'\mathbf{q}=0}^{\nu\nu'\omega=0} \tilde{G}_{(-\mathbf{k}')(-\omega)} \tilde{G}_{\mathbf{k}'\omega} \phi_{\mathbf{k}'\omega} = \phi_{\mathbf{k}\omega}, \quad (83)$$

where $r = s, t$ stands for the singlet and triplet channels. Results classified according to the different symmetries are shown in Fig. 29 (left). The order parameter of the leading instability has d -wave symmetry, as illustrated through the corresponding eigenfunction $\phi_{\mathbf{k}}$ which is essentially the gap function. Superconductivity is observed for hole doping $\delta \leq 0.18$ for $U/t = 8$. The transition temperature $T_c \lesssim 0.05t$ at 10% hole doping is compatible with the value $0.0518t$ reported by Staar *et al.*, 2013 for $U/t = 7$. In the DF calculation, superconductivity might however not be realized for doping levels $\lesssim 15\%$ due to the presence of phase separation observed in the same study at higher T . There is also no superconducting dome structure with a downturn towards half-filling in DF.

Such a dome has been reported by [Kitatani *et al.*, 2015](#), see Fig. 29 (right), where DMFT has been supplemented by non-local correlations using FLEX (and *GW*) to calculate the vertex. The leading eigenvalue in the particle-particle channel was computed via Eq. (83) as above. While FLEX+DMFT yields a superconducting dome, it however overestimates the non-local self-energy and the critical temperature.

Hidden order in the form of a staggered flux state (of *d*-density wave) is among several candidates for the origin of the pseudogap ([Chakravarty *et al.*, 2001](#)). DF calculations show that the density wave with *d*-wave symmetry dominates over density waves with other symmetries at lower *T*. However, the susceptibility shows no divergence at the accessible temperatures. The *d*-density wave state also appears to be shadowed by the superconducting state, since its extrapolated T_c is lower ([Otsuki *et al.*, 2014](#)).

4. Two dimensions: triangular lattice

Frustrated strongly correlated electron systems such as the Hubbard model on a triangular lattice are characterized by macroscopically degenerate ground states that lead to strong quantum fluctuations and a multitude of instabilities. Such systems hence exhibit very rich phase diagrams comprising of Mott-insulating, superconducting or resonating valence bond (RVB) states, commensurate or incommensurate SDW or non-collinear magnetic order. Important experimental realizations are (i) the stacked triangular CoO_2 layers in quasi two-dimensional sodium cobaltate Na_xCoO_2 , (ii) the organic salt $\kappa\text{-(BEDT-TTF)}_2\text{Cu}_2(\text{CN})_3$ where two BEDT-TTF molecules form spin $S = 1/2$ dimers which in turn constitute a triangular lattice, (iii) adatoms on a Si (111) surface, and (iv) bilayers of transition metal oxide heterostructures grown in the (111) direction. Diagrammatic extensions of DMFT are particularly suited in this context, because spatial correlations are highly relevant in the presence of frustration. Moreover, diagrammatic approaches are not affected by the sign-problem which, in the presence of frustration, strongly hampers QMC simulations or cluster extensions of DMFT that employ QMC as a solver.

As regards the *Mott transition*, [Lee *et al.*, 2008](#) showed that, compared to DMFT, the critical U of the Mott transition is reduced down to $U_c \sim 7t$ in $\text{DF}^{(2)}$, which agrees with DCA results ([Lee *et al.*, 2008](#)). This is analogous to the effect described in Sec. IV.A.2 for the square lattice. The difference is that here, there is no perfect nesting for the triangular lattice so that U_c stays finite and even large because of the high frustration.

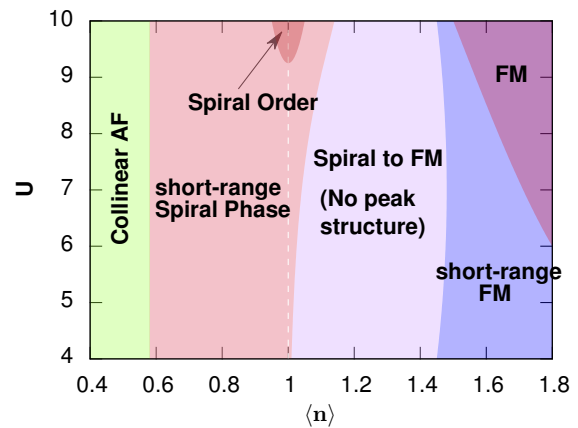


Figure 30 (Color online) Magnetic phase diagram of the doped triangular-lattice Hubbard model at fixed temperature $T = 0.1t$, as obtained within DF. Long-range spiral and FM magnetic order is found at sufficiently large values of U ; collinear AF at low electron fillings $\langle n \rangle$. From by [Li *et al.*, 2014](#).

Magnetism According to results from different many-body methods, the triangular lattice Hubbard model favors the 120° Néel state at large $U/t \sim 10$ ([Ohashi *et al.*, 2008](#); [Yoshioka *et al.*, 2009](#)), and this is also the case in the $\text{DF}^{(2)}$ calculation by [Lee *et al.*, 2008](#) as well in the $\text{DF}^{(2)}$ expansion around a DCA-like three-site cluster by [Antipov *et al.*, 2011](#). The rich magnetic phase diagram obtained by [Li *et al.*, 2014](#) is shown in Fig. 30. While the observation of finite temperature transitions is likely an artifact of the extrapolation method for the inverse susceptibility, one can interpret the finite transition temperature as an upper bound for a quasi-2d system of layers coupled in the third dimension. Close to half filling and at large U , spiral order is found which includes the 120° Néel state at half-filling. Interestingly, the frustration pushes the critical U for ordering above the aforementioned U_c for the MIT so that a non-magnetic insulating phase is realized at half-filling, possibly a spin-liquid state.

The spiral ordering is quickly destroyed upon doping, but short-range order marked by a peak in the static susceptibility at the corresponding wave vector survives. For electron doping ($\langle n \rangle > 1$) the spiral correlations make way for FM short-range- and at large U also long-range ordering. Quite asymmetrically, on the hole doped side ($\langle n \rangle < 1$) the susceptibility peaks at wave vector $\mathbf{Q} = (\pi, \pi)$ corresponding to a collinear AF. [Laubach *et al.*, 2015](#) tuned the lattice from triangular to square by changing a “vertical” bond hopping t' , and find in DF an evolution from the 120° AF order of the half-filled triangular lattice to the $\mathbf{Q} = (\pi, \pi)$ collinear AF order on the square lattice, in agreement with VCA.

[Li *et al.*, 2011](#) reported $\text{DF}^{(2)}$ results for the $\text{Sn/Si}(111)\sqrt{3} \times \sqrt{3}R30^\circ$ surface system which can be mapped onto

a triangular lattice Hubbard model with a band structure calculated within LDA. For this system, additional frustration due to next-nearest neighbor hopping however suppresses the 120° AF in favor of the collinear AF. [Hansmann *et al.*, 2013](#) used $GW+DMFT$ instead and emphasized the importance of long-range Coulomb interactions and charge ordering.

Energy and entropy [Antipov *et al.*, 2011](#) showed that spatial correlations significantly lower the energy of the spin-liquid state at half-filling, while leaving the energy of the Néel state essentially unaffected. As for the entropy, [Li *et al.*, 2014](#) reported that it increases with U at fixed T , and ascribe this counter-intuitive trend (which is in contrast to that for the unfrustrated square lattice) to a significant increase in the spin entropy due to localization. This opens a new possibility for adiabatic cooling in cold atom experiments by tuning U . Note that the highest entropy occurs at a filling $\langle n \rangle \approx 1.35$ which coincides with the optimal filling for superconductivity in sodium cobaltate, and signals the competition between the localized spin and the charge degrees of freedom. The high entropy can be related to the Seebeck coefficient through Kelvin’s formula and might be an important contribution to the large thermopower of $\text{Na}_x\text{CoO}_2 \cdot 1.3\text{H}_2\text{O}$ at $\langle n \rangle \sim 1.5$ ([Terasaki *et al.*, 1997](#)). Another factor favoring a large thermopower is the enhancement of the electron-hole asymmetry due to local electronic correlations which was found by [Wissgott *et al.*, 2011, 2010](#) using density functional theory (DFT+DMFT).

[Wilhelm *et al.*, 2015](#) also use the DFT bandstructure of the relevant a_{1g} orbital as a starting point, and find a spin-polaron peak in DF near van Hove filling – possibly explaining a weak absorption feature observed in optics experiments of nearly-ferromagnetic $\text{Na}_{0.7}\text{CoO}_2$ by [Wang *et al.*, 2004](#). The spin-polaron excitation at Γ has been traced back to the binding of quasiparticles with an FM paramagnon ([Boehnke and Lechermann, 2012](#)) originating from the spin-channel of ladder DF. The interplay of many-particle scattering incorporated through the DF self-energy and nesting also leads to a band flattening near van-Hove singularities as reported by [Yudin *et al.*, 2014](#): In analogy to a Bose-Einstein condensate, this highly degenerate fermionic state is referred to as “Fermi condensation”, and possibly signals an instability at lower T .

5. One and zero dimensions

One and zero dimensional systems are arguably the most challenging for diagrammatic approaches that start from DMFT, which as we recall is exact for $d = \infty$. In $1d$ the Fermi surface degenerates to two points. As a result of nesting, the ladder diagram series typically di-

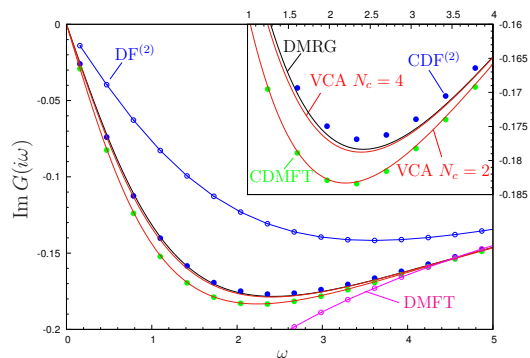


Figure 31 (Color online) Local Green’s function of the $1d$ Hubbard model obtained within $DF^{(2)}$ and two-site cluster $CDF^{(2)}$, in comparison to numerically exact DMRG, CDMFT and zero temperature variational cluster approach (VCA) calculations as well as DMFT. Adapted from [Hafermann *et al.*, 2008](#).

verges in several channels, so that ladder approximations cannot be applied. The $1d$ Hubbard model can nevertheless be studied using finite order diagrams as e.g. in $DF^{(2)}$ ([Hafermann *et al.*, 2008](#)) or the parquet equations ([Valli *et al.*, 2015b](#)). A proper description of the insulating state, which is the known ground state for all $U > 0$, requires a fully self-consistent calculation, in which the hybridization function changes from metallic character in DMFT to insulating in DF.

Fig. 31 shows such $DF^{(2)}$ calculations based on a single-site DMFT that capture the insulating state. The second-order diagrams however do not include the non-perturbative singlet correlations needed for an accurate description of the $1d$ physics. Hence, we see in Fig. 31 significant deviations from the numerically exact density matrix renormalization group (DMRG).

An alternative route followed by [Slezak *et al.*, 2009](#) and [Hafermann *et al.*, 2008](#) is to use a cluster instead of a DMFT solution as a starting point as discussed in Sec. III E. Already the expansion around a two-site cellular DMFT (CDMFT) solution captures crucial aspects of the $1d$ dimer physics and yields quantitative agreement with the DMRG benchmarks in Fig. 31. Whether spin-charge separation is captured by such diagrammatic extensions is an open question.

An equally challenging issue is the treatment of non-local correlations in $0d$ (molecular-like) systems. Progress towards the understanding of spatial correlations in finite, discrete systems has been recently achieved by means of a comparison ([Valli *et al.*, 2012, 2015b](#)) between nanoscopic (or real-space) DMFT, nanoscopic DfA ([Valli *et al.*, 2010](#)) and the exact solution of small correlated molecules (up to 10 sites). In Fig. 32 we show the results of the first parquet DfA calculation, performed for a ring molecule of 8-correlated equivalent sites (see inset of Fig. 32; it can also be considered as a

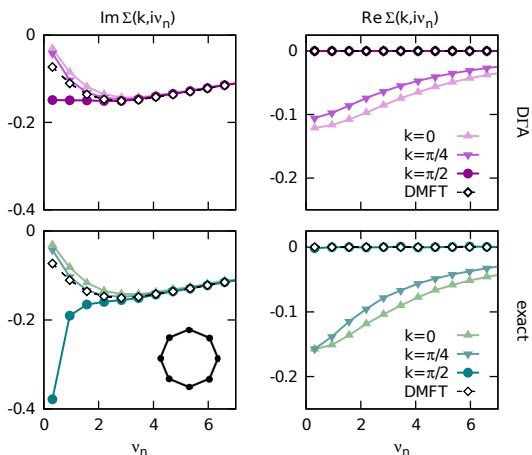


Figure 32 (Color online) Imaginary (left) and real part (right) of the self-energy vs. Matsubara frequency ν_n for an 8-site Hubbard nano-ring (see bottom left inset) with nearest neighbor hopping t and local interaction $U/t = 2$ at $T/t = 0.1$ at half-filling. Parquet DFA (upper panels), the exact solution (lower panels) and DMFT (both panels) are compared. From Valli *et al.*, 2015b.

1d Hubbard model with periodic boundary conditions). The comparison with DMFT shows that a substantial, though not complete part of the strong non-local correlations characterizing the exact solution of this 0d system is actually captured by the parquet DFA calculation. The improvement with respect to the parquet approximation solution and, thus, the importance of including the full frequency dependence of the 2PI vertex function, depend strongly on the parameter regime considered. It remains to be investigated whether the realization of an external self-consistency cycle in DFA (see Sec. III.A.4) can close the remaining gap to the exact solution. The systematic analysis of Valli *et al.*, 2012, 2015b further identified situations where a DMFT calculation is reliable. This can be used as a guide for the study of more complex systems, such as quantum points contacts with ~ 100 atoms (Florens, 2007; Jacob *et al.*, 2010; Valli *et al.*, 2010) or transition metal oxide nanoclusters (Das *et al.*, 2011; Valli *et al.*, 2015a).

B. Heavy fermions and Kondo lattice model

Heavy fermion systems are intermetallic compounds in which strongly correlated and localized electrons in partially filled f -shells of a rare earth or actinide element coexist with weakly correlated electrons of much broader bands provided by the other elements or orbitals. At elevated temperatures the f -electron magnetic moments are weakly coupled to a Fermi sea formed by s , p or d electrons. At low temperatures however, localized moments and conduction electrons can form new entities below the

Kondo temperature T_K , and magnetic order or unconventional superconductivity may be realized along with quantum critical points. The local Kondo physics as well as magnetic ordering is already contained in DMFT, but without spatial correlations that become important at the critical point and that are the realm of diagrammatic extensions of DMFT.

Let us consider the spin 1/2 Kondo-lattice model (KLM),

$$\mathcal{H} = \sum_{ij,\sigma} t_{ij} c_{i\sigma}^\dagger c_{j\sigma} + J \sum_i \mathbf{S}_i \cdot \mathbf{s}_i, \quad (84)$$

(also known as the s - d model) which is a minimal model for heavy fermion physics. Here, \mathbf{S}_i are the local and $\mathbf{s}_i = (1/2) \sum_{\sigma\sigma'} c_{i\sigma}^\dagger \boldsymbol{\sigma}_{\sigma\sigma'} c_{i\sigma'}$ the conduction electron spins, respectively.

The DMFT solution of this model reproduces the qualitatively different behavior at high and low temperatures. At low temperature, significantly smaller than T_K , a well defined hybridization gap opens. Reducing J , Otsuki *et al.*, 2009 find a quantum phase transition from this Kondo insulator to an AF-ordered state at $J_c \simeq 2.18$. If the conduction band is doped away from half filling, the formation of heavy quasiparticles leads to a large Fermi surface, which shows that the local moments in fact contribute to the Fermi surface volume (Otsuki *et al.*, 2009).

The KLM has been studied using the DF method at first by Sweep *et al.*, 2013. The corresponding implementation is essentially the same as for the Hubbard model, the only difference being the interaction term of the underlying impurity model. Sweep *et al.*, 2013 employed a weak-coupling CTQMC impurity solver using two bands for the localized and conduction electrons. Their rough estimate of the critical exchange interaction J_c in DF (at relatively high temperatures) yielded already a significant ($\sim 50\%$) reduction of J_c with respect to DMFT, induced by non-local fluctuations.

In a more recent ladder DF study, Otsuki, 2015 employ an interaction-expansion type CTQMC algorithm specifically devised for the Coqblin-Schrieffer model, and addressed the competition between d and p -wave superconductivity in the 2D KLM. On the square lattice and for a half-filled conduction electron band, the perfect nesting of the Fermi surface favors an AF ordering of the localized magnetic moments through the Ruderman-Kittel-Kasuya-Yoshida (RKKY) interaction. Hence similar to the 2D Hubbard model in Sec. IV.A.2, it is natural to ask which type of superconductivity emerges in heavy fermion materials near the AF quantum critical point.

Fig. 33 (a) shows the leading AF eigenvalue which has a critical behavior $1 - \lambda_{\text{AFM}} \propto e^{-\Delta/T}$ and a strong size dependence for $J \leq 1.2$. This indicates an AF ground state. For sufficiently large J , AF is suppressed due to the Kondo effect and the leading eigenvalue approaches a constant at low T , see right panel of Fig. 33 (a). The

estimated position of the quantum critical point, $J_c^{\text{DF}} = 1.35 \pm 0.05$, is close to the lattice QMC value of [Assaad, 1999](#), see Fig. 33 (b). This is another example of the quantitative accuracy of results obtained by means of diagrammatic methods.

[Otsuki, 2015](#) determined the superconducting transition temperature by an eigenvalue analysis as described in Sec. IV.A.2. The eigenvalues corresponding to eigenfunctions of B_{1g} (d -wave) and E_u (p -wave symmetry) are nearly degenerate in a wide doping range. While d -wave superconductivity is realized for $J \lesssim 0.9$, it is replaced by p -wave superconductivity as the leading instability for $J \gtrsim 0.9$. In both cases, AF fluctuations are likely to be the origin of the pairing. Remarkably, the crossover from d -wave to p -wave pairing correlates with the crossover from a small to the large Fermi surface. For weak coupling, d -wave pairing is favorable, because the regions of high-intensity of the eigenfunction coincide with the van-Hove points. As the hybridization band is formed and a large Fermi surface develops, low-energy excitations appear around $\mathbf{k} = (\pi/2, \pi/2)$ and p -wave symmetry emerges as a consequence of the scattering between them. The p -wave superconductivity is hence a consequence of the formation of heavy quasiparticles, which distinguishes the KLM from the Hubbard model.

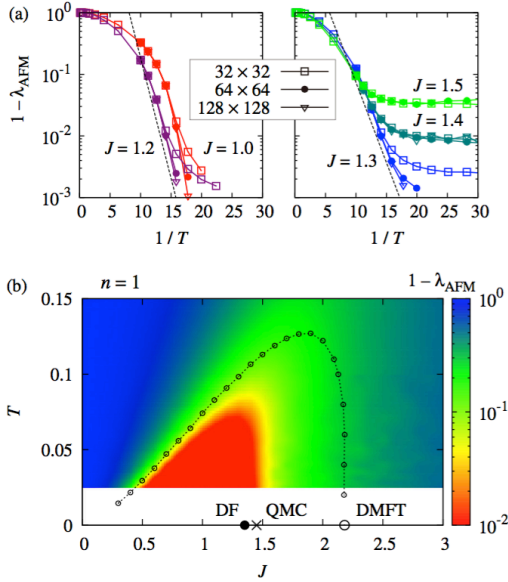


Figure 33 (Color online) (a) Critical scaling and lattice size dependence of the leading eigenvalue λ_{AFM} for the KLM in DF theory, indicating the presence of an AF ground state (left panel) while for $J > J_c$ (right panel) the Kondo effect suppresses AF fluctuations. (b) Critical region defined by $1 - \lambda_{\text{AFM}} \lesssim 10^{-2}$ exhibiting a dome shape similar to the DMFT phase boundary, albeit significantly shrunk. From [Otsuki, 2015](#).

C. Falicov-Kimball model

In the Falicov-Kimball (FK) model mobile electrons interact with localized ones via a Hubbard-type interaction U . This way it describes (annealed) disorder and represents one of the simplest systems where correlation effects can be observed. The Hamiltonian for the spinless FK model reads:

$$\mathcal{H} = \sum_k \varepsilon_k c_k^\dagger c_k + \sum_i \varepsilon_f f_i^\dagger f_i + \sum_i U c_i^\dagger c_i f_i^\dagger f_i, \quad (85)$$

where U is the interaction strength, ε_k the dispersion relation for the mobile (c) electrons and ε_f the local potential of the immobile (f) electrons; i labels the lattice sites.

The simple nature of the FK model compared to the Hubbard model is seen from Hamiltonian (85): every local f -electron occupation operator $w_i = f_i^\dagger f_i$ commutes with the Hamiltonian, providing an extensive number of conserved degrees of freedom. This has a number of important consequences. First, a set of mathematically rigorous results, including the existence of a phase transition to the f - c checkerboard-ordered phase of the Ising universality class in the particle-hole symmetric model has been established ([Brandt and Schmidt, 1986](#); [Kennedy and Lieb, 1986](#)). Second, the model is amenable to a sign-problem free Monte-Carlo sampling ([Antipov et al., 2016](#); [Maška and Czajka, 2006, 2005](#); [Žonda et al., 2009](#)), providing exact predictions for finite-size systems. Finally, the “impurity problem” solved in DMFT is exactly solvable both in equilibrium ([Brandt and Mielsch, 1989](#)) and non-equilibrium ([Eckstein and Kollar, 2008](#); [Eckstein et al., 2009](#)). DMFT has been used to study, among others, thermodynamics and spectral functions ([Brandt and Mielsch, 1989, 1990, 1991](#)), phase separation upon doping ([Freericks and Lemański, 2000](#)), dynamical properties including a discontinuity at zero-frequency ([Freericks and Miller, 2000](#)), and the absence of thermalization ([Eckstein and Kollar, 2008](#); [Eckstein et al., 2009](#)). The majority of these results is summarized in the excellent review by [Freericks and Zlatić, 2003](#).

The combination of these factors makes the FK model an ideal test-bed for computational approaches to strongly correlated systems, including cluster-extensions ([Hettler et al., 2000, 1998](#); [Maier et al., 2005a](#)) and, of particular importance here, diagrammatic extensions of DMFT. The latter profit from the fact that the interacting single- and multi-particle Green’s functions of the DMFT impurity problem can be obtained analytically. The local single-particle propagator reads

$$G_\nu^{\text{loc}} = w\mathcal{G}_\nu + (1 - w) [\mathcal{G}_\nu^{-1} - U]^{-1}, \quad (86)$$

where $\mathcal{G}_\nu = [i\nu + \mu - \Delta_\nu]^{-1}$ is the noninteracting Green’s function of the DMFT impurity problem, which can be calculated self-consistently together with the lattice Dyson equation and the f -electron occupation w .

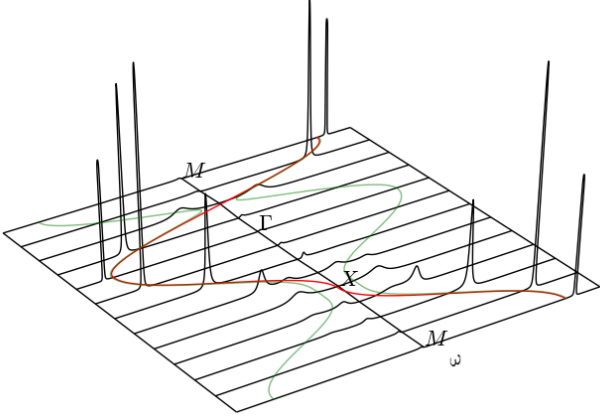


Figure 34 (Color online) Spectral functions of the FK model along a path through the Brillouin zone and as a function of the real frequency ω at $U = 1t$ and $T = 0.07t$, which can be compared to the corresponding result for the Hubbard model, Fig. 26. The red line is the bare dispersion and the green line that of a CDW checkerboard phase with a doubling of the unit cell. From Ribic *et al.*, 2016b.

The DMFT susceptibility and the local irreducible vertex in the particle-hole channel can be calculated as well (Freericks and Zlatić, 2003). This corresponds to the following full vertex

$$F^{\nu\nu'\omega} = \beta(\delta_{\omega 0} - \delta_{\nu\nu'}) a_{\nu'} a_{\nu+\omega} \quad (87)$$

where $a_\nu = (\Sigma_\nu^{\text{loc}} - U)\Sigma_\nu^{\text{loc}}/(\sqrt{w(1-w)}U)$, see Ribic *et al.*, 2016b.

Using these simplifications a set of further results for the analytical properties regarding the correlation functions of the FK model has been obtained: Antipov *et al.*, 2014 calculated the antisymmetrized three-particle vertex $F^{(6),\nu\nu'\nu''} = w(1-w)(2w-1)U^3 A_\nu A_{\nu'} A_{\nu''}$ which is zero at particle-hole symmetry. Ribic *et al.*, 2016a extended this to the full n -particle vertex for an arbitrary number of particles n , and estimated the error of truncating the DF theory at the $n = 2$ particle level. Diagrams emerging from the 3-particle vertex in DF theory may yield contributions of the same magnitude. Shvaika, 2000 and Ribic *et al.*, 2016b also calculated the exact two-particle reducible, irreducible in ph and pp channel, and the fully irreducible vertex of the FK model. Schäfer *et al.*, 2016a identified the applicability of perturbation theory by studying divergences of the DMFT vertex functions; below a single energy scale $\nu^*(U)$, the low-energy spectral properties of the model have a non-perturbative nature. Related results have also been reported by Janiš and Pokorný, 2014 and Ribic *et al.*, 2016b.

The application of two-particle methods has demonstrated important physical aspects of the model. Using 1PI and DF Ribic *et al.*, 2016b have shown how non-local correlations emerge as precursors to the charge density

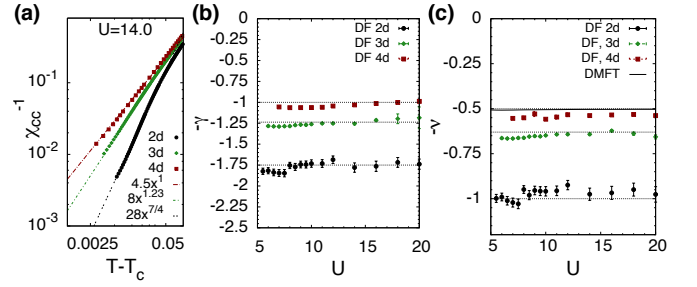


Figure 35 (Color online) (a) Inverse static c -electron charge susceptibility in $d = 2, 3, 4$ as a function of $T - T_c$ at $U = 14t$. The slope of the double logarithmic plot yields the critical exponent γ shown in (b) for different values of $U > 5t$. Lines in (b) indicate the prediction for Ising universality class. Error bars represent the regression errors. (c) Corresponding exponent ν for the correlation length vs. predictions for the Ising model (dashed lines) and DMFT results (solid line) as a function of U . From Antipov *et al.*, 2014.

wave (CDW) transition. These precursors lead to a more insulating solution and a four-peak structure in the \mathbf{k} -resolved spectral function in parts of the Brillouin zone as seen in Fig. 34. These peaks have been interpreted as a mixture of the DMFT metal-insulator transition caused by local correlations and non-local checkerboard CDW correlations. Yang *et al.*, 2014 have analyzed the interaction-driven crossover into the Mott phase and related it to the CDW correlations.

Antipov *et al.*, 2014 have studied the critical properties of the charge-ordering transition using the DF method. The inverse charge susceptibility of the c -electrons of the FK model in Fig. 35 shows different power-laws (i.e., different critical exponents) at the phase transition for different dimensions d . These critical exponents are also different from those for the Hubbard model, see Fig. 22. But as for the Hubbard model in three dimensions, the critical exponents γ (susceptibility, Fig. 35b), ν (correlation length, Fig. 35c), and anomalous dimension exponent $\eta = 2/\nu - \gamma$, extracted for $U > 5$ agree with the expected exact values, i.e., in this case the values for the Ising universality class. These results show that the diagrammatic extensions of DMFT can provide microscopic details of strongly correlated systems and at the same time correctly capture their critical properties.

The interest in the FK model has reappeared at different times. From the initial proposals of describing metal-insulator transitions in f -electron systems (Falicov and Kimball, 1969; Ramirez *et al.*, 1970) and testing various methods for strongly correlated electron systems, the recent interest is fueled by the progress in manufacturing artificial cold-atom systems and various manifestations of Anderson localization. In particular, multiband systems with large mass imbalance recently became available (Greif *et al.*, 2015; Jotzu *et al.*, 2015). Monte-Carlo simulations by Liu and Wang, 2015 indicate an Ising-type AF ordering in case of a mass-imbalance between the two

spin species; Philipp *et al.*, 2016 conclude that there is a Kondo effect for an arbitrary small hopping of the more localized electrons. In other words, the mass imbalanced Hubbard model resembles the FK model regarding the symmetry of the ordering parameter, but the Hubbard model regarding the MIT. At the same time, the existence of Anderson localization in the absence of explicit disorder has been recently shown by Antipov *et al.*, 2016.

D. Models of Disorder

Out of the many possible non-local effects, disorder plays a special role in condensed matter physics as it is ubiquitous in electronic materials. A spatially random potential reduces the extent of electronic wave functions to a localization length ξ_l , changing the motion of charge carriers and increasing the resistivity of the system. When ξ_l becomes smaller than the linear system size L the disorder renders an otherwise metallic system insulating (Anderson, 1958; Thouless, 1974), a phenomenon known as Anderson transition.

On the technical side, disorder or at least a local disorder potential is closely related to the FK model of the previous section. The difference is that here the disorder distribution is externally given (quenched disorder) whereas in the FK model the localized electrons are thermodynamically distributed (annealed disorder). For disorder problems, DMFT corresponds to the coherent potential approximation (CPA) of Soven, 1969 and Taylor, 1967, which has the same averaging as in Eq. (86) but for a fixed (quenched) w . If the electrons also interact, a combination of CPA and DMFT is possible. Among others, it yields information about the local density of states (Byczuk *et al.*, 2009) and the geometrically averaged density of states in the typical medium theory (Dobrosavljević *et al.*, 2003). The decay and the probability distribution of the latter quantity indicate the Anderson transition. Improved estimates of local and geometric DOS and critical disorder strengths can be obtained through cluster extensions of these theories (Ekuma *et al.*, 2014; Jarrell and Krishnamurthy, 2001; Terletska *et al.*, 2014).

The simplest model to incorporate the quenched disorder effects is the Anderson model, which reads

$$H = \sum_k \varepsilon_k n_k + \sum_i v_i n_i, \quad (88)$$

where random potentials v are distributed with a distribution $p(v)$.

Similar to the case of clean systems, the self-consistent description at the single particle level lacks some of the important physics present in the problem. For example, the vanishing conductivity in Anderson insulators needs a description at the two-particle level that is absent in CPA (Jarrell and Krishnamurthy, 2001) and requires additional diagrammatic calculations (Janiš and

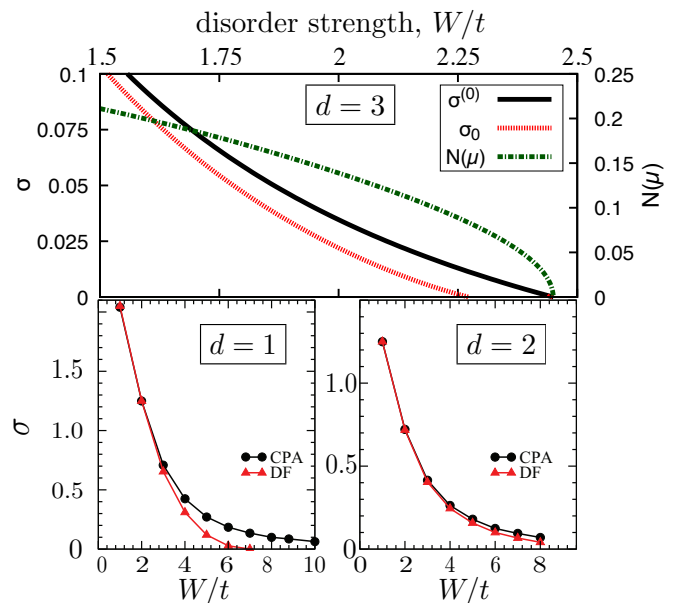


Figure 36 (Color online) Conductivity σ as a function of the disorder strength W . Top: Results for $3d$ at $T = 0$ with leading order vertex correction (σ_0) from Pokorny and Janis, 2013. Bottom: DF vs. CPA results for $d = 1$ (left) and $d = 2$ (right) at $T = 0.02t$ from Terletska *et al.*, 2013.

Kolorenč, 2005; Kroha, 1990). Diagrammatic extensions of the CPA for model (88) have been pioneered by Janiš, 2001, who has developed a parquet approach to calculate the two-particle vertex and the conductivity. Using the local irreducible vertex and the local Green’s function from CPA, self-consistent equations for the full vertex, the non-local Green’s function and the self-energy are derived and evaluated. The vertex corrections to the conductivity from this method have been calculated by Pokorny and Janis, 2013. The results for $3d$ and binary disorder are shown in Fig. 36 (top). Vertex corrections always reduce the conductivity, and the leading order correction renders the conductivity negative at a large disorder strength W .

A complementary DF extension of CPA for the Anderson model (88) has been put forward by Terletska *et al.*, 2013. Using the “replica trick” relation $\ln Z = \lim_{m \rightarrow 0} m^{-1}(Z^m - 1)$, the effect of disorder is replaced by a local elastic effective interaction between electrons in different replicas:

$$W^{\text{dis}} = \sum_{l=2}^{\infty} \frac{\kappa_l(v)}{l!} \left[\sum_m \int d\tau n_i^m(\tau) \right]^l, \quad (89)$$

Here $\kappa_l(v)$ is the l -th order cumulant of the disorder distribution $p(v)$ and m is the replica index. Since the disorder-induced interaction is local, the complexity of the problem at hand is similar to the Hubbard and Falicov-Kimball models, described in sections IV.A and

IV.C, respectively. The remaining ladder DF steps follow section III.B. Terletska *et al.*, 2013 use a box disorder distribution and show that weak localization effects suppress the conductivity in $1d$ and $2d$, see bottom panels of Fig. 36. Note that the DF extension of CPA can be done also without replica trick, as shown by Osipov and Rubtsov, 2013.

The advantage of the diagrammatic extensions of CPA is that they can be straightforwardly extended to interacting systems with disorder. This has been done by Yang *et al.*, 2014, Janiš and Pokorný, 2014 and Haase *et al.*, 2017, who considered the Anderson-Falicov-Kimball and Anderson-Hubbard models. Even a clean FK model exhibits localization effects due to the intrinsic annealed disorder, i.e. the scattering at the immobile f -electrons (Antipov *et al.*, 2016). Yang *et al.*, 2014 showed that the added quenched disorder in the Anderson-FK model also localizes the system. Janiš and Pokorný, 2014 have obtained the full phase diagram of the FK model in infinite dimensions, and showed that the critical disorder-driven metal-insulator transition shares its universal critical behavior with the interaction-driven Mott transition. Haase *et al.*, 2017 showed that the disorder in the Hubbard model at small disorder strength tends to increase the impact of antiferromagnetism by raising the Neel temperature, increases the U value of the Mott transition, and at large disorder strengths brings the conductivity of the $3d$ system to zero, in agreement with the picture of an Anderson transition.

E. Non-local interactions and multi-orbitals

Despite the successes of the Hubbard model to capture important physical aspects of correlated electrons and materials, it misses some interesting physics such as plasmons and inhomogeneous charge density waves. These effects are related to non-local interactions, which are included in the extended Hubbard model

$$\mathcal{H} = \sum_{ij,\sigma} t_{ij} c_{i\sigma}^\dagger c_{j\sigma} + U \sum_i n_{i\uparrow} n_{i\downarrow} + \sum_{ij\sigma\sigma'} V_{ij} n_{i\sigma} n_{j\sigma'}. \quad (90)$$

The non-local interaction V_{ij} can be sizable, with a magnitude reaching up to 60% of the on-site Coulomb interaction. As a result graphene for example appears metallic, even though it would be on the verge to the insulating state if only the local Coulomb interaction was considered (Wehling *et al.*, 2011). For certain surface systems, the non-local interaction may also exhibit a slow $1/r$ decay with distance r , rendering long-range contributions important (Hansmann *et al.*, 2016, 2013).

Addressing dynamical screening and long-range physics in correlated fermionic systems is challenging since QMC simulations typically suffer from the sign problem. In DMFT, on the other hand, the non-local

interaction is restricted to its static Hartree contribution. Cluster extensions of DMFT naturally face the difficulty to treat interaction terms that extend beyond the finite cluster. Hence, inter-cluster interactions are either truncated as in CDMFT (Bolech *et al.*, 2003) and DCA (Wu and Tremblay, 2014), or treated through a mean-field decoupling, as in variational cluster perturbation theory (Aichhorn *et al.*, 2004). In essence, the range of the interaction is limited by the size of the cluster.

This restriction is lifted in extended DMFT (EDMFT) (Chitra and Kotliar, 2000, 2001; Kajueter, 1996; Si and Smith, 1996; Smith and Si, 2000) and GW +DMFT (Biermann *et al.*, 2003; Sun and Kotliar, 2002, 2004), where the non-local interaction can have arbitrary momentum dependence and range. These methods capture the Mott transition and at the same time the effects of screening and the charge-order transition driven by the inter-site interaction. The GW +DMFT self-energy describes band renormalization effects and Hubbard satellites; EDMFT on the other hands captures the local correlations induced the non-local interaction. Both methods, EDMFT and GW +DMFT, require the calculation of a local impurity problem with a frequency dependent interaction, which is quite straightforward in CTQMC for a density-density type of interaction (Werner and Millis, 2007, 2010).

A highlight of EDMFT has been establishing the picture of local quantum criticality. Fig. 37 shows the results by Zhu *et al.*, 2003 for the Kondo lattice model (84) with an additional spin-dependent non-local interaction I of Ising type. At zero temperature there is a quantum critical point separating the Kondo phase with a large Fermi surface at small I and the magnetic phase for large I . Grempel and Si, 2003 determined the corresponding critical exponent $\alpha \approx 0.7$, which is outside the standard Hertz-Millis-Moriya theory (von Löhneysen *et al.*, 2007).

As regards GW +DMFT, Aryal *et al.*, 2012 showed that a fully self-consistent treatment of the GW +DMFT cures some of the deficiencies of self-consistent GW , such as the failure to describe plasmon satellites. Werner *et al.*, 2012 incorporated the frequency-dependent interaction obtained from constrained RPA into LDA+DMFT. This scheme may be viewed as a simplified version of GW +DMFT where the self-energy is local and the two-particle quantities are evaluated at a non-self-consistent level. The application to the normal phase of the iron pnictide superconductor BaFe_2As_2 showed that the dynamical screening of the interaction significantly affects the low-energy electronic structure. A second effect beyond standard DFT+DMFT are exchange contributions to the self-energy that stem from the non-locality of the interaction. These non-local self-energies were shown to be significant in BaFe_2As_2 , other iron pnictides and chalcogenides (Tomczak *et al.*, 2012b), as well as in transition metal oxides (Miyake *et al.*, 2013; Tomczak *et al.*, 2012a).

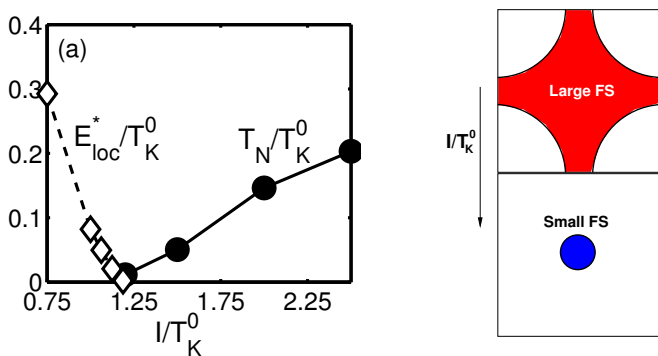


Figure 37 (Color online) Left: Néel Temperature T_N and Kondo breakdown scale E_{loc}^* as a function of the non-local interaction I relative to the Kondo scale T_K^0 for the Kondo lattice model with non-local spin interaction. The Kondo effect vanishes simultaneously with the magnetic phase transition. Right: Fermi surface volume collapse at the quantum critical point from a large Fermi surface where the f electrons contribute to the Fermi surface because of the Kondo effect (for $E_{\text{loc}}^* > 0$) to a small Fermi surface of the conduction electrons only. From [Zhu *et al.*, 2003](#).

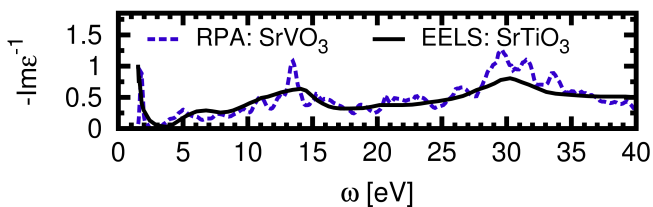


Figure 38 (Color online) Inverse dielectric function of SrVO_3 in $GW+DMFT$ as a function of frequency, showing plasmon peaks at 5 eV and 14 eV. From [Tomczak *et al.*, 2014](#).

These realistic calculations as well as $GW+EDMFT$ model calculations for the extended Hubbard Hamiltonian (90) by [Aryal *et al.*, 2013](#) show that the dynamical screening leads to plasmonic features in the spectral function. [Huang *et al.*, 2014](#) further found that including non-local interactions up to the third-nearest neighbors destabilizes the charge-ordered state, which may be viewed as a kind of frustration effect. [Tomczak *et al.*, 2012a, 2014](#) and [Boehnke *et al.*, 2016](#) studied the spectral properties of the prototypical correlated metal SrVO_3 using $GW+DMFT$ and self-consistent $GW+EDMFT$, respectively. They find that the effective local interaction is considerably reduced due to dynamical screening effects, and conclude that the spectral function exhibits a plasmon satellite in the region of the previously reported upper Hubbard band. In the dielectric function, Fig. 38, this plasmon peak is around 5 eV. This and the larger plasmon peak around 14 eV agree with the electron-energy-loss spectrum (EELS) of [Kohiki *et al.*, 2000](#).

Despite the successes of $EDMFT$ and $GW+EDMFT$, they do not provide a complete description of plasmons. This is due to an inconsistent treatment of the single and two-particle properties, which breaks local charge conservation and gauge invariance. In particular, from the continuity equation $\omega^2 \langle nn^* \rangle_{\mathbf{q}\omega} = q^2 \langle jj^* \rangle_{\mathbf{q}\omega}$ it follows that the polarization behaves as q^2/ω^2 for small q and finite (Matsubara) frequencies ω_m . This is the case for the Lindhardt function in RPA, non-self-consistent GW (so-called G_0W_0), quasiparticle self-consistent GW (QSGW) ([Faleev *et al.*, 2004](#)), and QSGW+DMFT ([Tomczak, 2015](#)), but not in $EDMFT$ and $GW+DMFT$. In $EDMFT$, the polarization is momentum-independent and the plasmon dispersion diverges for $q \rightarrow 0$ in the presence of long-range Coulomb interaction. Vertex corrections from a local but frequency-dependent irreducible vertex are necessary to fulfill the Ward identity. In the dual boson (DB) approach (Sec. III.G.2), such vertex corrections can be constructed diagrammatically via non-local polarization corrections. The resulting polarization Π_ω vanishes for small q as q^2 ([Hafermann, 2014](#); [Rubtsov *et al.*, 2012](#); [Stepanov *et al.*, 2016b](#)). Hence, the solution of the plasmon pole defined by $1 + V(\mathbf{q})\Pi_\omega(\mathbf{q}) = 0$, yields the correct dispersion relation $\omega(\mathbf{q}) = \omega_p + aq^2$ at small q . Here a is a constant and ω_p the plasma frequency.

Using DB, [van Loon *et al.*, 2014a](#) showed that the two-particle excitations exhibit both a renormalization of the dispersion and a spectral weight transfer. This is similar to the analogous interaction effects known for single-particle excitations. Fig. 39 shows the inverse dielectric function $-\text{Im}\epsilon_{\mathbf{q}}^{-1}(E)$ of 2d surface plasmons in the presence of long-range interaction $V(q)$. For weak interaction one observes a broad particle-hole continuum and the expected $\omega_p(q) \sim \sqrt{q}$ dispersion of the 2d plasmon at small q . As the interaction is increased (Fig. 39 middle), the plasmon dispersion is renormalized, and spectral weight is transferred to a second branch which now becomes visible at larger energies. Above $U^* \sim 2.4$ the system is a Mott insulator, and only the weakly dispersing second band at energy U^* associated with doublon-holon excitations survives.

The extended Hubbard model with nearest-neighbor interaction V also shows a transition to a charge density wave (CDW) ordering, which was studied in lattice Monte Carlo calculations by [Zhang and Callaway, 1989](#), in DMFT by [Wahle *et al.*, 1998](#), in $EDMFT$ by [Sun and Kotliar, 2002](#), and in the two-particle self-consistent approach by [Davoudi and Tremblay, 2007](#). In DB, also the momentum dependence of the polarization corrections is included. This shifts the DB CDW transition to smaller V values compared to $EDMFT$ and agrees with RPA in the weak-coupling limit ([van Loon *et al.*, 2014b](#)).

Long-range non-local interactions can also play a crucial role for ultra-cold quantum gases in optical lattices ([Bloch *et al.*, 2012, 2008](#); [Lewenstein *et al.*, 2012](#)). For example, these highly tunable systems allow one

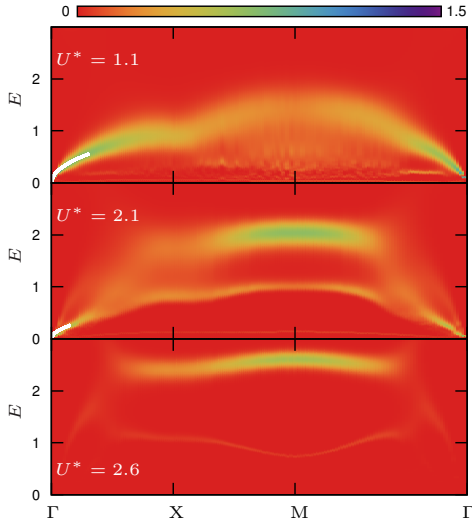


Figure 39 (Color online) Inverse dielectric function of the extended 2d Hubbard model with long-range Coulomb interaction as a function of momentum and energy, for three different values of the effective on-site interaction U^* . The two-particle excitations show a renormalized dispersion and spectral weight transfer. From [van Loon *et al.*, 2014a](#).

to realize the dipolar fermi Hubbard model ([Baranov, 2008](#); [Baranov *et al.*, 2012](#); [Lahaye *et al.*, 2009](#); [Lewenstein *et al.*, 2012](#)) which corresponds to Hamiltonian (90) with an anisotropic long-range dipolar interaction $V_{jk} \sim [1 - 3(\hat{r}_{jk} \cdot \hat{d})^2] / (r_{jk})^3$. Here \hat{r}_{jk} is the direction and r_{jk} the magnitude of the lattice vector from site j to k , and all dipoles are assumed to point in the same direction \hat{d} . Using the DB approach, [van Loon *et al.*, 2015b](#) found that for sufficiently large dipole strengths and dipoles oriented perpendicular to the lattice plane ($\phi = 0$), a transition to checkerboard order occurs, while a striped phase emerges when they point to nearest neighbors ($\phi = \pi/2$). For dipoles pointing along the diagonal ($\phi = \pi/4$), [van Loon *et al.*, 2015b](#) found a novel ultra-long-range ordered phase which can alter the topological properties and lead to a Lifshitz transition (Fig. 40).

Within the DGA framework, non-local interactions $V_{\mathbf{q}}$ can be taken into account as part of the irreducible vertex which also allows for *ab initio* materials calculations, see Sec. III.A.3. The first AbinitioDGA calculation for SrVO₃ by [Galler *et al.*, 2017](#) takes the local vertex of all three t_{2g} orbitals into account, calculated via worm sampling ([Gunacker *et al.*, 2015](#)) in CTQMC. Even for $V_{\mathbf{q}} = 0$, there is a momentum differentiation larger than 0.2eV in the real-part of the self-energy [see Fig. 41(a)], while the \mathbf{k} -dependence of its imaginary-part, of the quasiparticle weight and scattering rate is much weaker; cf. related findings for the 3d Hubbard model ([Schäfer *et al.*, 2015b](#)). This shows that even far away from a phase transition and even beyond GW-type of dia-

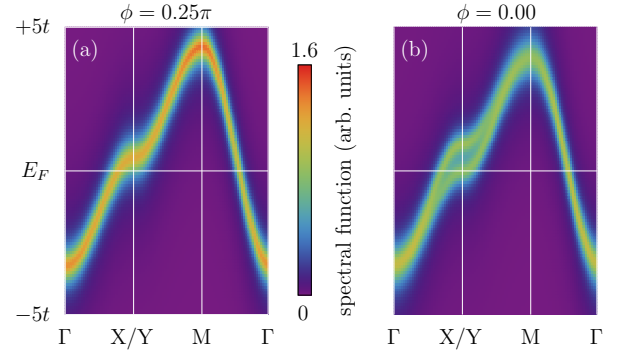


Figure 40 (Color online) Spectral function of the dipolar fermion Hubbard model superimposed over two different paths in the Brillouin zone via the X and Y points, respectively. In the symmetric case, both paths are equivalent (left). The dipolar interaction drives the Lifshitz transition by breaking the symmetry between X and Y points (right). From [van Loon *et al.*, 2016a](#).

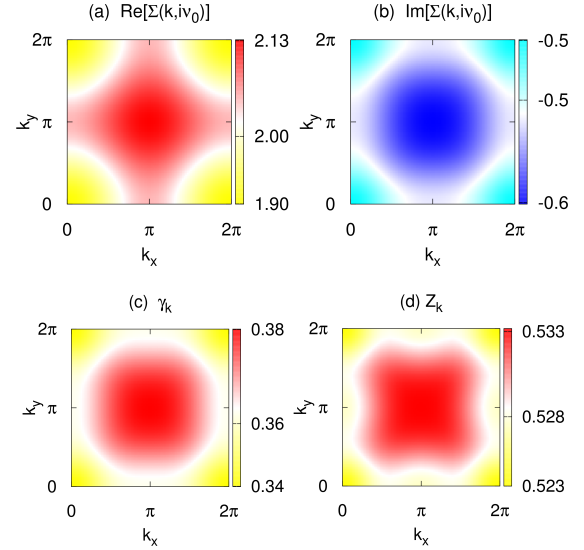


Figure 41 (Color online) AbinitioDGA for SrVO₃ showing the momentum-dependence of (a) the real and (b) the imaginary part of the self-energy at the lowest Matsubara frequency ($i\nu_0$) for the xy orbital in the $k_z=0$ -plane; (c) corresponding scattering rate $\gamma_{\mathbf{k}}$ and (d) quasi-particle weight $Z_{\mathbf{k}}$. From [Galler *et al.*, 2017](#).

grams ($V_{\mathbf{q}}=0$), non-local correlations play a role in actual materials. We expect realistic multi-orbital calculations that include non-local correlations beyond GW+DMFT to thrive in the future.

V. OPEN SOURCE IMPLEMENTATIONS

The increasing complexity of numerical methods requires expert knowledge and leads to increasing implementation efforts. For these reasons, and to ensure re-

producibility of results, it is vital to make codes publicly accessible. We encourage such efforts and believe they should be rewarded. In recent years, a number of open source libraries and codes have appeared or will appear in the near future. We can separate these into program packages that (i) solve a local impurity problem and allow calculating the two-particle vertex and that (ii) calculate non-local correlations beyond DMFT diagrammatically.

For step (i), solving the AIM, let us mention five program packages: `ALPS` (Bauer *et al.*, 2011; Gaenko *et al.*, 2017), `iQuist` (Huang *et al.*, 2015), `pomero1` (Antipov and Krivenko, 2015), `TRIQS` (Parcollet *et al.*, 2015) and `w2dynamics` (Parragh *et al.*, 2012). The `ALPS` and `TRIQS` libraries aim to provide a reusable set of components to facilitate the implementation of algorithms for strongly correlated systems. Strong-coupling CTQMC impurity solvers based on `ALPS` are available (Gull *et al.*, 2011; Hafermann *et al.*, 2013). The `iQuist` package (Huang *et al.*, 2015) provides a collection of impurity solvers and pre- and post-processing tools, with the implementation of Shinaoka *et al.*, 2017a allowing the computation of two-particle functions. The `pomero1` code (Antipov and Krivenko, 2015) provides an optimized implementation of the ED method to compute vertex functions. The `TRIQS` package includes strong-coupling CTQMC (Seth *et al.*, 2016) and has been extended to two-particle quantities with the development of `TRILEX` (Aryal and Parcollet, 2015, 2016b) and `QUADRILEX` (Aryal and Parcollet, 2016a). The `w2dynamics` package is also based on hybridization expansion CTQMC, and uses improved estimators and worm sampling for calculating all components of the two-particle multi-orbital vertex (Gunacker *et al.*, 2015, 2016) as well as vertex asymptotics (Kaufmann *et al.*, 2017).

As for (ii), diagrammatic extensions of DMFT, publicly available codes only start to emerge. `OPENDF` (Antipov *et al.*, 2015) is the first open source implementation of the DF approach. `parquet` (Yang *et al.*, 2009) and `Victory` (Li, 2015) are program packages to solve the parquet equations for a given fully irreducible vertex Λ as it is used for example in DfA. They differ in the way the vertex at large frequencies outside the initial frequency box is treated (periodic vs. asymptotic boundary conditions for frequencies).

Let us also mention some auxiliary codes: `gftools` (Antipov, 2013) for manipulating Green's functions and several codes for an analytical continuation with the maximum entropy method (MaxEnt): `MEM` (Jarrell and Gubernatis, 1996), `maxent` (Levy *et al.*, 2017), and `w2dynamics` (Parragh *et al.*, 2012) which incorporates MaxEnt with optimization techniques developed by Sandvik, 1998b.

VI. CONCLUSION AND OUTLOOK

Diagrammatic extensions of DMFT appealingly combine numerical and analytical techniques for studying strongly correlated electron systems. Local correlations are treated by the method which is arguably best at this: DMFT or a more general self-consistent (numerical) solution of an AIM. On top of this, non-local correlations in the self-energy and susceptibilities are constructed through Feynman diagrams. Historically this development started with methods that supplemented the local DMFT self-energy by a non-local one from another method such as spin boson theory, FLEX or *GW*. These combinations are discussed in Secs. III.F and III.G.1, respectively. More recently, we have seen the rise of methods which more intimately connect the local and non-local parts. These approaches calculate a dynamical frequency-dependent local vertex by solving an impurity model numerically and derive non-local correlations therefrom diagrammatically. One can envisage this as raising the DMFT concept of the locality of the one-particle (1PI) vertex (i.e., the self energy) to the next, i.e., two-particle vertex level. All of these dynamical vertex approaches are closely related and rely on the same concept, but they differ in which local two-particle vertex is taken and how the diagrams are constructed. One may compare this to the difference between different cluster extensions of DMFT, say DCA vs. CDMFT. Table II provides an overview of the various approaches.

In Sec. IV, we have extensively compared these vertex approaches with each other and against other state-of-the-art approaches such as cluster extensions of DMFT and lattice QMC. The application to the Hubbard model has shown a qualitatively consistent picture for the self-energy, susceptibility and its phase diagram, e.g., regarding coherent quasiparticle excitations and the suppression of long-range order in comparison with DMFT. The methods have been shown to reproduce highly nontrivial effects such as the pseudogap. In some cases where benchmarks are available, we have even seen quantitative agreement. In general, one finds that, while the second-order diagram already contains nontrivial effects of dynamical short-range correlations, ladder diagrams are important for a quantitative description. The fluctuation diagnostics (Gunnarsson *et al.*, 2015) of the self-energy can be exploited to choose which ladder should be considered. As expected, the one-dimensional case turned out to be the most challenging for an extension of (dynamical) mean-field theory. However it is encouraging that the corresponding results are improved substantially by using the vertex on a cluster of sites as a starting point. The application to the (extended) Hubbard-, Falicov-Kimball-, Kondo lattice- and Anderson models demonstrates that these methods are very versatile.

A unique feature of diagrammatic extensions is that they combine the nonperturbative physics of local cor-

Method	Local vertex	Green's function	Diagrams	Action/Functional
parquet DGA [Sec. III.A.1] QUADRILEX [Sec. III.A.4]	two-particle irreducible $\Lambda^{\nu\nu'\omega}$	$G_{\mathbf{k}\nu}$	parquet	$\mathcal{K}_4[G_\nu^{\text{loc}}, G_{\sigma\sigma'}^{(2),\nu\nu'\omega}]$ (28)
ladder DGA [Sec. III.A.2]	2PI in channel r : $\Gamma_r^{\nu\nu'\omega}$	$G_{\mathbf{k}\nu}$	ladder	—
DF [Sec. III.B]	one-particle reducible $F^{\nu\nu'\omega}$	$\tilde{G}_{0,\mathbf{k}\nu}$	2nd order, ladder, parquet	$\tilde{\mathcal{S}}[\tilde{c}^+, \tilde{c}]$ (37)
1PI [Sec. III.C]	one-particle irreducible ^a $F^{\nu\nu'\omega}$	$\tilde{G}_{0,\mathbf{k}\nu}, G_\nu^{\text{loc}}$	ladder	$\mathcal{S}^{1\text{PI}}$ (48)
DMF ² RG [Sec. III.D]	one-particle irreducible ^a $F^{\nu\nu'\omega}$	$G_{A,\mathbf{k}\nu}, S_{A,\mathbf{k}\nu}$	RG flow in Λ	$\mathcal{S}_\Lambda[c^+, c]$ (51)
TRILEX [Sec. III.G.3]	three-leg vertex $\gamma_{\nu\omega}$	$G_{\mathbf{k}\nu}, W_{\mathbf{q}\omega}$	Hedin Eqs. (81)	$\mathcal{K}_3[G_\nu, W_\omega, \chi_{\nu\omega}]$ (80)
DB [Sec. III.G.2]	$F^{\nu\nu'\omega}, \gamma_{\nu\omega}$	$\tilde{G}_{0,\mathbf{k}\nu}, \tilde{W}_{0,\mathbf{q}\omega}$	2nd order, ladder	$\tilde{\mathcal{S}}[\tilde{c}^+, \tilde{c}, \tilde{\rho}^*, \tilde{\rho}]$ (71)

Table II Summary of the various closely related diagrammatic extensions of DMFT. The *1st column* denotes the method and the *2nd column* the local vertex function that serves as a starting point; these are the different two-particle vertices defined in Sec. II.A^a and the bosonic three-leg vertex $\gamma_{\nu\omega}$. The *3rd column* identifies the Green's function lines connecting these local building blocks via the Feynman diagrams of the *4th column*.^b The *last column* denotes the fundamental functional \mathcal{K} or the action \mathcal{S} of the functional integral the method is based on. Here, DF and DB introduce dual fermionic $\tilde{c}^{(\dagger)}$ and bosonic variables $\tilde{\rho}^{(*)}$. For further details we refer the reader to the corresponding sections.

^a 1PI and DMF²RG expand in terms of 1PI vertices, which for the *two-particle vertex* happens to be identical to the full vertex F used in DF. Even if truncated at the two-particle level, the difference in the expansion scheme leads nonetheless to distinct 1PI and DF methods, see Sec. III.C.

^b G_ν^{loc} is the local propagator of the reference system and $\tilde{G}_{0,\mathbf{k}\nu}$ the non-local lattice propagator constructed with the local self-energy of the reference system [Eqs. (38), (49), (72)]; $\tilde{W}_{0,\mathbf{q}\omega}$ is a corresponding bosonic (interaction) propagator [Eq. (73)].

relations à la DMFT with truly long-ranged correlations over hundreds or thousands of sites. In addition, they obviously do not suffer from a sign problem. We have seen results which would be difficult or even impossible to obtain using other methods. Examples are the numerical calculation of (quantum) critical exponents of models for strongly correlated electrons, the absence of a Mott transition in the two-dimensional Hubbard model or the rich phase diagram of the frustrated triangular lattice Hubbard model. Another highlight is the renormalization of the dispersion and spectral weight transfer of collective modes. The application to the Kondo lattice model revealed an interplay of local Kondo physics and long-range antiferromagnetic correlations around the quantum critical point. These results establish the complementarity of diagrammatic extensions to other many-body methods, in particular cluster extensions.

After roughly ten years of development, we have only seen the tip of the iceberg of diagrammatic extensions of DMFT. The field is very dynamic and many new results emerged even during the preparation of this review. We expect to see many more applications in the future. This is driven by a growing community of users of these methods and techniques as well as by methodological advances. These have already allowed the treatment of non-local interactions as in AbinitioDGA or DB—as well as first *ab initio* materials calculations. This offers the prospects of improving even upon GW +DMFT. Recent advances in impurity solvers will trigger multi-orbital ap-

plications and the calculation of vertex corrections to the electrical conductivity. Using the real-space formulation of these methods one can imagine applications to ultracold atoms in harmonic trapping potentials or topological insulators.

The calculation of the local three-particle vertex has been feasible so far in isolated cases only. By means of new technical developments this quantity, and derived non-local diagrams therefrom, might become more accessible. This may lead to new insights and the discovery of physical effects originating from three-particle excitations. Diagrammatic extensions which expand around a DCA or CDMFT cluster as a starting point have been shown to be feasible and it is clear that such calculations will become more prevalent in the future. The combination of diagrammatic extensions with the functional renormalization group is very appealing from a theoretical point of view, which should be further explored. The DMF²RG has shown first encouraging results. Last but not least, we believe that the reviewed diagrammatic approaches offer a new route to the thriving field of strongly correlated electron systems out of equilibrium.

In the past, these methods were used by a number of specialized groups. Because these methods deal with vertex functions they are technically more involved than other approaches. This barrier will become much less important in the near future, not least due to efforts to release codes into the public domain. We are convinced that these methods will become standard tools in the

research of strongly correlated systems and hope that this review will encourage our readers to use one of these methods in their research.

ACKNOWLEDGEMENTS

To do ...

REFERENCES

- Abrikosov, A. A., L. P. Gorkov, and I. E. Dzyaloshinski (1975), *Methods of Quantum Field Theory in Statistical Physics* (Dover, New York).
- Aichhorn, M., H. G. Evertz, W. von der Linden, and M. Potthoff (2004), *Phys. Rev. B* **70**, 235107.
- Anderson, P. W. (1958), *Phys. Rev.* **109** (5), 1492.
- Anderson, P. W. (1997), *The Theory of Superconductivity in the High- T_c Cuprates* (Princeton University Press, Princeton, NJ).
- Antipov, A. A. (2013), Gftools [aentipov.github.io/gftools](https://github.com/gftools).
- Antipov, A. E., E. Gull, and S. Kirchner (2014), *Phys. Rev. Lett.* **112**, 226401.
- Antipov, A. E., Y. Javanmard, P. Ribeiro, and S. Kirchner (2016), *Phys. Rev. Lett.* **117**, 146601.
- Antipov, A. E., and I. Krivenko (2015), “pomerol: 1.1,” .
- Antipov, A. E., J. P. LeBlanc, and E. Gull (2015), *Physics Procedia* **68**, 43.
- Antipov, A. E., A. N. Rubtsov, M. I. Katsnelson, and A. I. Lichtenstein (2011), *Phys. Rev. B* **83**, 115126.
- Aoki, H., N. Tsuji, M. Eckstein, M. Kollar, T. Oka, and P. Werner (2014), *Rev. Mod. Phys.* **86**, 779.
- Aryasetiawan, F., and O. Gunnarsson (1998), *Reports on Progress in Physics* **61** (3), 237.
- Aryasetiawan, F., M. Imada, A. Georges, G. Kotliar, S. Biermann, and A. I. Lichtenstein (2004), *Phys. Rev. B* **70**, 195104.
- Assaad, F. F. (1999), *Phys. Rev. Lett.* **83**, 796.
- Avella, A., F. Mancini, and R. Münzner (2001), *Phys. Rev. B* **63**, 245117.
- Ayral, T., S. Biermann, and P. Werner (2013), *Phys. Rev. B* **87**, 125149.
- Ayral, T., and O. Parcollet (2015), *Phys. Rev. B* **92**, 115109.
- Ayral, T., and O. Parcollet (2016a), *Phys. Rev. B* **94**, 075159.
- Ayral, T., and O. Parcollet (2016b), *Phys. Rev. B* **93**, 235124.
- Ayral, T., P. Werner, and S. Biermann (2012), *Phys. Rev. Lett.* **109**, 226401.
- Baranov, M. (2008), *Physics Reports* **464** (3), 71 .
- Baranov, M. A., M. Dalmonte, G. Pupillo, and P. Zoller (2012), *Chemical Reviews* **112** (9), 5012.
- Bauer, B., L. D. Carr, H. G. Evertz, A. Feiguin, J. Freire, S. Fuchs, L. Gamper, J. Gukelberger, E. Gull, S. Guertler, A. Hehn, R. Igarashi, S. V. Isakov, D. Koop, P. N. Ma, P. Mates, H. Matsuo, O. Parcollet, G. Pawłowski, J. D. Picon, L. Pollet, E. Santos, V. W. Scarola, U. Schollwöck, C. Silva, B. Surer, S. Todo, S. Trebst, M. Troyer, M. L. Wall, P. Werner, and S. Wessel (2011), *Journal of Statistical Mechanics: Theory and Experiment* **2011** (05), P05001.
- Baym, G., and L. P. Kadanoff (1961), *Phys. Rev.* **124**, 287.
- Bednorz, J. G., and K. A. Müller (1986), *Zeitschrift für Physik B Condensed Matter* **64**, 189.
- Bickers, N. E. (2004), “Theoretical methods for strongly correlated electrons,” Chap. 6 (Springer-Verlag New York Berlin Heidelberg) pp. 237–296.
- Bickers, N. E., and S. R. White (1991), *Phys. Rev. B* **43**, 8044.
- Biermann, S., F. Aryasetiawan, and A. Georges (2003), *Phys. Rev. Lett.* **90**, 086402.
- Bloch, I., J. Dalibard, and S. Nascimbène (2012), *Nat. Phys.* **8**, 267.
- Bloch, I., J. Dalibard, and W. Zwerger (2008), *Rev. Mod. Phys.* **80**, 885.
- Blümer, N. (2002), *Mott-Hubbard Metal-Insulator Transition and Optical Conductivity in High Dimensions*, Ph.D. thesis (Universität Augsburg).
- Boehnke, L., H. Hafermann, M. Ferrero, F. Lechermann, and O. Parcollet (2011), *Phys. Rev. B* **84**, 075145.
- Boehnke, L., and F. Lechermann (2012), *Phys. Rev. B* **85**, 115128.
- Boehnke, L., F. Nilsson, F. Aryasetiawan, and P. Werner (2016), *Phys. Rev. B* **94**, 201106.
- Bolech, C. J., S. S. Kancharla, and G. Kotliar (2003), *Phys. Rev. B* **67**, 075110.
- Brandt, U., and C. Mielsch (1989), *Zeitschrift für Phys. B Condens. Matter* **75** (3), 365.
- Brandt, U., and C. Mielsch (1990), *Zeitschrift für Phys. B Condens. Matter* **79** (2), 295.
- Brandt, U., and C. Mielsch (1991), *Zeitschrift für Phys. B Condens. Matter* **82** (1), 37.
- Brandt, U., and R. Schmidt (1986), *Zeitschrift für Phys. B Condens. Matter* **63** (1), 45.
- Brener, S., H. Hafermann, A. N. Rubtsov, M. I. Katsnelson, and A. I. Lichtenstein (2008), *Phys. Rev. B* **77** (19), 195105.
- Bulla, R., T. Costi, and T. Pruschke (2008), *Rev. Mod. Phys.* **80**, 395.
- Bulla, R., A. C. Hewson, and T. Pruschke (1998), *Journal of Physics: Condensed Matter* **10** (37), 8365.
- Byczuk, K., W. Hofstetter, U. Yu, and D. Vollhardt (2009), *Eur. Phys. J. Spec. Top.* **180** (1), 135.
- Capone, M., and G. Kotliar (2006), *Phys. Rev. B* **74**, 054513.
- Castellani, C., C. D. Castro, D. Feinberg, and J. Ranninger (1979), *Phys. Rev. Lett.* **43**, 1957.
- Vekić, M., and S. R. White (1993), *Phys. Rev. B* **47**, 1160.
- Chakravarty, S., R. B. Laughlin, D. K. Morr, and C. Nayak (2001), *Phys. Rev. B* **63**, 094503.
- Chitra, R., and G. Kotliar (2000), *Phys. Rev. Lett.* **84**, 3678.
- Chitra, R., and G. Kotliar (2001), *Phys. Rev. B* **63**, 115110.
- Dagotto, E. (1994), *Rev. Mod. Phys.* **66**, 763.
- Dai, X., K. Haule, and G. Kotliar (2005), *Phys. Rev. B* **72**, 045111.
- Daré, A.-M., and G. Albinet (2000), *Phys. Rev. B* **61**, 4567.
- Das, H., G. Sangiovanni, A. Valli, K. Held, and T. Saha-Dasgupta (2011), *Phys. Rev. Lett.* **107**, 197202.
- Davoudi, B., and A.-M. S. Tremblay (2007), *Phys. Rev. B* **76**, 085115.
- De Dominicis, C. (1962), *J. Math. Phys.* **3** (5), 983.
- De Dominicis, C., and P. C. Martin (1964a), *J. Math. Phys.* **5** (1), 14.
- De Dominicis, C., and P. C. Martin (1964b), *J. Math. Phys.* **5** (1), 31.
- Diatlov, I. T., V. V. Sudakov, and K. A. Ter-Martirosian (1957), *Sov. Phys. JETP* **5**, 631.
- Dobrosavljević, V., A. A. Pastor, and B. K. Nikolić (2003), *Europhys. Lett.* **62** (1), 76.

- Eckstein, M., and M. Kollar (2008), *Phys. Rev. Lett.* **100** (12), 120404.
- Eckstein, M., M. Kollar, and P. Werner (2009), *Phys. Rev. Lett.* **103**, 056403.
- Ekuma, C. E., H. Terletska, K.-M. Tam, Z.-Y. Meng, J. Moreno, and M. Jarrell (2014), *Phys. Rev. B* **89** (8), 081107.
- Faleev, S. V., M. van Schilfgaarde, and T. Kotani (2004), *Phys. Rev. Lett.* **93**, 126406.
- Falicov, L. M., and J. C. Kimball (1969), *Phys. Rev. Lett.* **22** (19), 997.
- Florens, S. (2007), *Phys. Rev. Lett.* **99**, 046402.
- Fratino, L., P. Sémon, M. Charlebois, G. Sordi, and A.-M. Tremblay (2017), preprint arXiv:1702.01821.
- Freericks, J. K., and V. Zlatić (2003), *Rev. Mod. Phys.* **75**, 1333.
- Freericks, J. K., and R. Lemański (2000), *Phys. Rev. B* **61** (20), 13438.
- Freericks, J. K., and P. Miller (2000), *Phys. Rev. B* **62** (15), 22.
- Fuchs, S., E. Gull, L. Pollet, E. Burovski, E. Kozik, T. Pruschke, and M. Troyer (2011), *Phys. Rev. Lett.* **106**, 030401.
- Gaenko, A., A. Antipov, G. Carcassi, T. Chen, X. Chen, Q. Dong, L. Gamper, J. Gukelberger, R. Igarashi, S. Isakov, M. Könz, J. LeBlanc, R. Levy, P. Ma, J. Paki, H. Shinaoka, S. Todo, M. Troyer, and E. Gull (2017), *Computer Physics Communications* **213**, 235 .
- Galler, A., P. Thunström, P. Gunacker, J. M. Tomczak, and K. Held (2017), *Phys. Rev. B* **95**, 115107.
- Gebhard, F. (1997), *The Mott Metal-insulator transition* (Springer-Verlag (Berlin)).
- Georges, A., and G. Kotliar (1992), *Phys. Rev. B* **45**, 6479.
- Georges, A., G. Kotliar, W. Krauth, and M. J. Rozenberg (1996), *Rev. Mod. Phys.* **68** (1), 13.
- Greif, D., G. Jotzu, M. Messer, R. Desbuquois, and T. Esslinger (2015), *Phys. Rev. Lett.* **115** (26), 260401.
- Grepel, D. R., and Q. Si (2003), *Phys. Rev. Lett.* **91**, 026401.
- Gukelberger, J., L. Huang, and P. Werner (2015), *Phys. Rev. B* **91**, 235114.
- Gukelberger, J., E. Kozik, and H. Hafermann (2016), preprint arXiv:1611.07523.
- Gull, E., A. J. Millis, A. I. Lichtenstein, A. N. Rubtsov, M. Troyer, and P. Werner (2011a), *Rev. Mod. Phys.* **83** (2), 349.
- Gull, E., O. Parcollet, and A. J. Millis (2013), *Phys. Rev. Lett.* **110**, 216405.
- Gull, E., P. Staar, S. Fuchs, P. Nukala, M. S. Summers, T. Pruschke, T. C. Schulthess, and T. Maier (2011b), *Phys. Rev. B* **83**, 075122.
- Gull, E., P. Werner, S. Fuchs, B. Surer, T. Pruschke, and M. Troyer (2011c), *Computer Physics Communications* **182** (4), 1078 .
- Gull, E., P. Werner, A. Millis, and M. Troyer (2007), *Phys. Rev. B* **76**, 235123.
- Gull, E., P. Werner, O. Parcollet, and M. Troyer (2008), *EPL (Europhysics Letters)* **82** (5), 57003.
- Gunacker, P., M. Wallerberger, E. Gull, A. Hausoel, G. Sangiovanni, and K. Held (2015), *Phys. Rev. B* **92**, 155102.
- Gunacker, P., M. Wallerberger, T. Ribic, A. Hausoel, G. Sangiovanni, and K. Held (2016), *Phys. Rev. B* **94**, 125153.
- Gunnarsson, O., T. Schäfer, J. P. F. LeBlanc, E. Gull, J. Merino, G. Sangiovanni, G. Rohringer, and A. Toschi (2015), *Phys. Rev. Lett.* **114**, 236402.
- Gunnarsson, O., T. Schäfer, J. P. F. LeBlanc, J. Merino, G. Sangiovanni, G. Rohringer, and A. Toschi (2016), *Phys. Rev. B* **93**, 245102.
- Haase, P., S.-X. Yang, T. Pruschke, J. Moreno, and M. Jarrell (2017), *Phys. Rev. B* **95**, 045130.
- Hafermann, H. (2010), *Numerical Approaches to Spatial Correlations in Strongly Interacting Fermion Systems*, Ph.D. thesis (University of Hamburg).
- Hafermann, H. (2014), *Phys. Rev. B* **89**, 235128.
- Hafermann, H. (2016), (unpublished).
- Hafermann, H., S. Brener, A. Rubtsov, M. Katsnelson, and A. Lichtenstein (2008), *JETP Letters* **86**, 677.
- Hafermann, H., C. Jung, S. Brener, M. I. Katsnelson, A. N. Rubtsov, and A. I. Lichtenstein (2009a), *Europhysics Letters* **85**, 27007.
- Hafermann, H., M. Kecker, S. Brener, A. N. Rubtsov, M. I. Katsnelson, and A. I. Lichtenstein (2009b), *J Supercond Nov Magn* **22**, 45.
- Hafermann, H., G. Li, A. N. Rubtsov, M. I. Katsnelson, A. Lichtenstein, and H. Monien (2009c), *Phys. Rev. Lett.* **102**, 206401.
- Hafermann, H., E. G. C. P. van Loon, M. I. Katsnelson, A. I. Lichtenstein, and O. Parcollet (2014), *Phys. Rev. B* **90**, 235105.
- Hafermann, H., K. R. Patton, and P. Werner (2012), *Phys. Rev. B* **85**, 205106.
- Hafermann, H., P. Werner, and E. Gull (2013), *Computer Physics Communications* **184** (4), 1280 .
- Hague, J. P., M. Jarrell, and T. C. Schulthess (2004), *Phys. Rev. B* **69**, 165113.
- Hansmann, P., T. Ayrál, A. Tejada, and S. Biermann (2016), *Scientific Reports* **6**, 10.1038/srep19728.
- Hansmann, P., T. Ayrál, L. Vaugier, P. Werner, and S. Biermann (2013), *Phys. Rev. Lett.* **110**, 166401.
- Harland, M., M. I. Katsnelson, and A. I. Lichtenstein (2016), *Phys. Rev. B* **94**, 125133.
- Hedin, L. (1965), *Phys. Rev.* **139**, A796.
- Hedin, L. (1999), *J. Phys.: Condens. Matter* **11** (42), R489.
- Held, K. (2007), *Advances in Physics* **56**, 829 .
- Held, K. (2014), *Dynamical Vertex Approximation* [arXiv:1411.5191] In Lecture Notes "Autumn School on Correlated Electrons. DMFT at 25: Infinite Dimensions", Reihe Modeling and Simulation, Vol. 4, Forschungszentrum Juelich GmbH (publisher), E. Pavarini, E. Koch, D. Vollhardt, and A. I. Lichtenstein (editors) [ISBN 978-3-89336-953-9].
- Held, K., A. Katanin, and A. Toschi (2008), *Progress of Theoretical Physics (Supplement)* **176**, 117.
- Hertz, J. A. (1976), *Phys. Rev. B* **14**, 1165.
- Hertz, J. A., and D. M. Edwards (1973), *J. Phys. F: Met. Phys.* **3**, 2174.
- Hettler, M. H., M. Mukherjee, M. Jarrell, and H. R. Krishnamurthy (2000), *Phys. Rev. B* **61**, 12739.
- Hettler, M. H., A. N. Tahvildar-Zadeh, M. Jarrell, T. Pruschke, and H. R. Krishnamurthy (1998), *Phys. Rev. B* **58**, R7475.
- Hirsch, J. E., and R. M. Fye (1986), *Phys. Rev. Lett.* **56**, 2521.
- Hirschmeier, D., H. Hafermann, E. Gull, A. I. Lichtenstein, and A. E. Antipov (2015), *Phys. Rev. B* **92**, 144409.
- Holm, C., and W. Janke (1993), *Phys. Rev. B* **48**, 936.
- Huang, L., T. Ayrál, S. Biermann, and P. Werner (2014), *Phys. Rev. B* **90**, 195114.

- Huang, L., Y. Wang, Z. Y. Meng, L. Du, P. Werner, and X. Dai (2015), *Computer Physics Communications* **195**, 140 .
- Hugenholtz, N. M. (1957), *Physica* **23** (1-5), 481.
- Imada, M., A. Fujimori, and Y. Tokura (1998), *Rev. Mod. Phys.* **70**, 1039.
- Isakov, S., A. E. Antipov, and E. Gull (2016), *Phys. Rev. B* **94**, 035102.
- Jacob, D., K. Haule, and G. Kotliar (2010), *Phys. Rev. B* **82**, 195115.
- Janiš, V. (2001), *Phys. Rev. B* **64**, 115115.
- Janiš, V., A. Kauch, and V. Pokorný (2017), *Phys. Rev. B* **95**, 045108.
- Janiš, V., and J. Kolorenč (2005), *Phys. Rev. B* **71**, 245106.
- Janiš, V., and V. Pokorný (2014), *Phys. Rev. B* **90**, 045143.
- Janiš, V., and D. Vollhardt (1992), *Int. J. Mod. Phys. B* **06**, 731.
- Jarrell, M. (1992), *Phys. Rev. Lett.* **69** (1), 168.
- Jarrell, M., and J. E. Gubernatis (1996), *Physics Reports* **269** (3), 133 .
- Jarrell, M., and H. R. Krishnamurthy (2001), *Phys. Rev. B* **63**, 125102.
- Jotzu, G., M. Messer, F. Görg, D. Greif, R. Desbuquois, and T. Esslinger (2015), *Phys. Rev. Lett.* **115**, 073002.
- Jung, C. (2010), *Superperturbation theory for correlated fermions*, Ph.D. thesis (University of Hamburg).
- Jung, C., A. Lieder, S. Brener, H. Hafermann, B. Baxevanis, A. Chudnovskiy, A. Rubtsov, M. Katsnelson, and A. Lichtenstein (2012), *Annalen der Physik* **524** (1), 49.
- Jung, C., A. Wilhelm, H. Hafermann, S. Brener, and A. Lichtenstein (2011), *Annalen der Physik* **523** (8-9), 706.
- Kajueter, H. (1996), Ph.D. thesis (Rutgers University).
- Katanin, A. A. (2005), *Phys. Rev. B* **72**, 035111.
- Katanin, A. A. (2013), *J. Phys. A: Math. Theor.* **46** (4), 045002.
- Katanin, A. A. (2015), *JETP* **120**, 1085.
- Katanin, A. A. (2016), preprint arXiv:1604.01702.
- Katanin, A. A., A. Toschi, and K. Held (2009), *Phys. Rev. B* **80**, 075104.
- Katsnelson, M. I., V. Y. Irkhin, L. Chioncel, A. I. Lichtenstein, and R. A. de Groot (2008), *Rev. Mod. Phys.* **80**, 315.
- Kaufmann, J., P. Gunacker, and K. Held (2017), preprint arXiv:1703.09407.
- Kennedy, T., and E. H. Lieb (1986), *Physica A* **138** (1-2), 320.
- Kent, P. R. C., M. Jarrell, T. A. Maier, and T. Pruschke (2005), *Phys. Rev. B* **72**, 060411.
- Kinza, M., and C. Honerkamp (2013), *Phys. Rev. B* **88**, 195136.
- Kitatani, M., N. Tsuji, and H. Aoki (2015), *Phys. Rev. B* **92**, 085104.
- Kohiki, S., M. Arai, H. Yoshikawa, S. Fukushima, M. Oku, and Y. Waseda (2000), *Phys. Rev. B* **62**, 7964.
- Kotliar, G., S. Y. Savrasov, K. Haule, V. S. Oudovenko, O. Parcollet, and C. A. Marianetti (2006), *Rev. Mod. Phys.* **78**, 865.
- Kotliar, G., S. Y. Savrasov, G. Pálsson, and G. Biroli (2001), *Phys. Rev. Lett.* **87**, 186401.
- Kotov, V. N., B. Uchoa, V. M. Pereira, F. Guinea, and A. H. Castro Neto (2012), *Rev. Mod. Phys.* **84**, 1067.
- Kozik, E., E. Burovski, V. W. Scarola, and M. Troyer (2013), *Phys. Rev. B* **87**, 205102.
- Kozik, E., M. Ferrero, and A. Georges (2015), *Phys. Rev. Lett.* **114**, 156402.
- Krivenko, I., A. Rubtsov, M. Katsnelson, and A. Lichtenstein (2010), *JETP Letters* **91** (6), 319.
- Kroha, J. (1990), *Physica A* **167** (1), 231.
- Kuchinskii, E. Z., I. A. Nekrasov, and M. V. Sadovskii (2005), *JETP Letters* **82**, 198.
- Kuchinskii, E. Z., I. A. Nekrasov, and M. V. Sadovskii (2006), *Low Temp. Phys.* **32**, 398.
- Kuchinskii, E. Z., and M. V. Sadovskii (1999), *JETP* **88**, 968.
- Kuneš, J. (2011), *Phys. Rev. B* **83**, 085102.
- Kusunose, H. (2006), *J. Phys. Soc. Jpn.* **75** (5), 054713.
- Lahaye, T., C. Menotti, L. Santos, M. Lewenstein, and T. Pfau (2009), *Reports on Progress in Physics* **72** (12), 126401.
- Laubach, M., R. Thomale, C. Platt, W. Hanke, and G. Li (2015), *Phys. Rev. B* **91**, 245125.
- LeBlanc, J., X. Chen, R. Levy, A. E. Antipov, A. Millis, and E. Gull (2017), (unpublished).
- LeBlanc, J. P. F., A. E. Antipov, F. Becca, I. W. Bulik, G. K.-L. Chan, C.-M. Chung, Y. Deng, M. Ferrero, T. M. Henderson, C. A. Jiménez-Hoyos, E. Kozik, X.-W. Liu, A. J. Millis, N. V. Prokof'ev, M. Qin, G. E. Scuseria, H. Shi, B. V. Svistunov, L. F. Tocchio, I. S. Tupitsyn, S. R. White, S. Zhang, B.-X. Zheng, Z. Zhu, and E. Gull (Simons Collaboration on the Many-Electron Problem) (2015), *Phys. Rev. X* **5**, 041041.
- Lee, H., G. Li, and H. Monien (2008), *Phys. Rev. B* **78**, 205117.
- Levy, R., J. LeBlanc, and E. Gull (2017), *Computer Physics Communications* , (in print).
- Lewenstein, M., A. Sanpera, and V. Ahufinger (2012), *Ultracold Atoms in Optical Lattices: Simulating Quantum Many-Body Systems* (Oxford University Press, Oxford).
- Li, G. (2015), *Phys. Rev. B* **91**, 165134.
- Li, G., A. E. Antipov, A. N. Rubtsov, S. Kirchner, and W. Hanke (2014), *Phys. Rev. B* **89**, 161118.
- Li, G., M. Laubach, A. Fleszar, and W. Hanke (2011), *Phys. Rev. B* **83**, 041104.
- Li, G., H. Lee, and H. Monien (2008), *Phys. Rev. B* **78**, 195105.
- Li, G., N. Wentzell, P. Pudleiner, P. Thunström, and K. Held (2016), *Phys. Rev. B* **93**, 195134.
- Lichtenstein, A. I., and M. I. Katsnelson (2000), *Phys. Rev. B* **62**, R9283.
- Lieb, E. H., and F. Y. Wu (1968), *Phys. Rev. Lett.* **20**, 1445.
- Lifshitz, I. M. (1960), *Sov. Phys. JEPT* **11**, 1130.
- Liu, Y.-H., and L. Wang (2015), *Phys. Rev. B* **92** (23), 235129.
- von Löhneysen, H., A. Rosch, M. Vojta, and P. Wölfle (2007), *Rev. Mod. Phys.* **79**, 1015.
- van Loon, E. G. C. P., H. Hafermann, A. I. Lichtenstein, and M. I. Katsnelson (2015a), *Phys. Rev. B* **92**, 085106.
- van Loon, E. G. C. P., H. Hafermann, A. I. Lichtenstein, A. N. Rubtsov, and M. I. Katsnelson (2014a), *Phys. Rev. Lett.* **113**, 246407.
- van Loon, E. G. C. P., M. I. Katsnelson, L. Chomaz, and M. Leshchko (2016a), *Phys. Rev. B* **93**, 195145.
- van Loon, E. G. C. P., M. I. Katsnelson, and M. Leshchko (2015b), *Phys. Rev. B* **92**, 081106.
- van Loon, E. G. C. P., F. Krien, H. Hafermann, E. A. Stepanov, A. I. Lichtenstein, and M. I. Katsnelson (2016b), *Phys. Rev. B* **93**, 155162.

- van Loon, E. G. C. P., A. I. Lichtenstein, M. I. Katsnelson, O. Parcollet, and H. Hafermann (2014b), *Phys. Rev. B* **90**, 235135.
- Mahan, G. D. (2000), *Many-Particle Physics* (Kluwer Academic/Plenum Publishers, New York).
- Maier, T., M. Jarrell, T. Pruschke, and M. H. Hettler (2005a), *Rev. Mod. Phys.* **77**, 1027.
- Maier, T. A., M. Jarrell, T. C. Schulthess, P. R. C. Kent, and J. B. White (2005b), *Phys. Rev. Lett.* **95**, 237001.
- Maier, T. A., M. S. Jarrell, and D. J. Scalapino (2006), *Phys. Rev. Lett.* **96**, 047005.
- Mancini, F. (2000), *EPL (Europhysics Letters)* **50** (2), 229.
- Maška, M., and K. Czajka (2006), *Phys. Rev. B* **74** (3), 035109.
- Maška, M. M., and K. Czajka (2005), *Phys. Status Solidi B* **242** (2), 479.
- Merino, J., and O. Gunnarsson (2014), *Phys. Rev. B* **89**, 245130.
- Merker, L., S. Kirchner, E. Muñoz, and T. A. Costi (2013), *Phys. Rev. B* **87**, 165132.
- Mermin, N. D., and H. Wagner (1966), *Phys. Rev. Lett.* **17**, 1307.
- Metzner, W. (1991), *Phys. Rev. B* **43**, 8549.
- Metzner, W., M. Salmhofer, C. Honerkamp, V. Meden, and K. Schönhammer (2012), *Rev. Mod. Phys.* **84**, 299.
- Metzner, W., and D. Vollhardt (1989), *Phys. Rev. Lett.* **62**, 324.
- Mielke, A., and H. Tasaki (1993), *Commun. Math. Phys.* **158**, 341.
- Millis, A. J. (1993), *Phys. Rev. B* **48**, 7183.
- Miyake, T., C. Martins, R. Sakuma, and F. Aryasetiawan (2013), *Phys. Rev. B* **87**, 115110.
- Montorsi, A., Ed. (1992), *The Hubbard Model - A Reprint Volume* (World Scientific, Singapore).
- Moreo, A. (1993), *Phys. Rev. B* **48** (5), 3380.
- Moriya, T. (1985), *Spin Fluctuations in Itinerant Electron Magnetism*, edited by M. Cardona, P. Fulde, and H.-J. Queisser (Springer Verlag, Berlin, Heidelberg).
- Moukouri, S., S. Allen, F. Lemay, B. Kyung, D. Poulin, Y. M. Vilks, and A.-M. S. Tremblay (2000), *Phys. Rev. B* **61**, 7887.
- Moukouri, S., and M. Jarrell (2001), *Phys. Rev. Lett.* **87**, 167010.
- Muñoz, E., C. J. Bolech, and S. Kirchner (2013), *Phys. Rev. Lett.* **110**, 016601.
- Negele, J. W., and H. Orland (1998), *Quantum Many-Particle Systems*, edited by D. Pines (Westview Press).
- Nekrasov, I., E. Kokorina, E. Kuchinskii, Z. Pchelkina, and M. Sadovsikii (2008), *J. Phys. Chem. Solids* **69** (12), 3269.
- Nekrasov, I., E. Kuchinskii, and M. Sadovsikii (2011), *J. Phys. Chem. Solids* **72** (5), 371.
- Ohashi, T., T. Momoi, H. Tsunetsugu, and N. Kawakami (2008), *Phys. Rev. Lett.* **100**, 076402.
- Osipov, A. A., and A. N. Rubtsov (2013), *New J. Phys.* **15** (7), 075016.
- Otsuki, J. (2013), *Phys. Rev. B* **87**, 125102.
- Otsuki, J. (2015), *Phys. Rev. Lett.* **115**, 036404.
- Otsuki, J., H. Hafermann, and A. I. Lichtenstein (2014), *Phys. Rev. B* **90**, 235132.
- Otsuki, J., H. Kusunose, and Y. Kuramoto (2009), *Phys. Rev. Lett.* **102**, 017202.
- Otsuki, J., M. Ohzeki, H. Shinaoka, and K. Yoshimi (2017), preprint arXiv:1702.03056.
- Pairault, S., D. Sénéchal, and A.-M. S. Tremblay (1998), *Phys. Rev. Lett.* **80**, 5389.
- Pairault, S., D. Sénéchal, and A.-M. S. Tremblay (2000), *Eur. Phys. J. B* **16**, 85.
- Parcollet, O., M. Ferrero, T. Ayrál, H. Hafermann, I. Krivenko, L. Messio, and P. Seth (2015), *Computer Physics Communications* **196**, 398.
- Park, H., K. Haule, and G. Kotliar (2008), *Phys. Rev. Lett.* **101**, 186403.
- Parragh, N., A. Toschi, K. Held, and G. Sangiovanni (2012), *Phys. Rev. B* **86**, 155158.
- Pavarini, E., E. Koch, D. Vollhardt, and A. Lichtenstein (2014), *DMFT at 25: Infinite Dimensions*, Reihe Modeling and Simulation 4, Vol. 4 (Forschungszentrum Jülich Zentralbibliothek, Verlag (Jülich), Jülich).
- Philipp, M.-T., M. Wallerberger, P. Gunacker, and K. Held (2016), preprint arXiv:1611.10079.
- Pokorny, V., and V. Janis (2013), *J. Phys. Condens. Matter* **25** (2), 175502.
- Pollet, L., N. V. Prokof'ev, and B. V. Svistunov (2011), *Phys. Rev. B* **83**, 161103.
- Pudleiner, P., T. Schäfer, D. Rost, G. Li, K. Held, and N. Blümer (2016), *Phys. Rev. B* **93**, 195134.
- Ramirez, R., L. Falicov, and J. Kimball (1970), *Phys. Rev. B* **2** (8), 3383.
- Ribic, T., G. Rohringer, and K. Held (2016a), preprint arXiv:1612.03011.
- Ribic, T., G. Rohringer, and K. Held (2016b), *Phys. Rev. B* **93** (19), 195105.
- van Roekeghem, A., T. Ayrál, J. M. Tomczak, M. Casula, N. Xu, H. Ding, M. Ferrero, O. Parcollet, H. Jiang, and S. Biermann (2014), *Phys. Rev. Lett.* **113**, 266403.
- Rohringer, G. (2013), *New routes towards a theoretical treatment of nonlocal electronic correlations*, Ph.D. thesis (Vienna University of Technology).
- Rohringer, G., and A. Toschi (2016), *Phys. Rev. B* **94**, 125144.
- Rohringer, G., A. Toschi, H. Hafermann, K. Held, V. I. Anisimov, and A. A. Katanin (2013), *Phys. Rev. B* **88**, 115112.
- Rohringer, G., A. Toschi, A. Katanin, and K. Held (2011), *Phys. Rev. Lett.* **107**, 256402.
- Rohringer, G., A. Valli, and A. Toschi (2012), *Phys. Rev. B* **86**, 125114.
- Rost, D., E. V. Gorelik, F. Assaad, and N. Blümer (2012), *Phys. Rev. B* **86**, 155109.
- Rubtsov, A. N. (2006), preprint arXiv:0601333.
- Rubtsov, A. N., M. I. Katsnelson, and A. I. Lichtenstein (2008), *Phys. Rev. B* **77**, 033101.
- Rubtsov, A. N., M. I. Katsnelson, and A. I. Lichtenstein (2012), *Ann. Phys.* **327** (5), 1320.
- Rubtsov, A. N., M. I. Katsnelson, A. I. Lichtenstein, and A. Georges (2009), *Phys. Rev. B* **79** (4), 045133.
- Rubtsov, A. N., V. V. Savkin, and A. I. Lichtenstein (2005), *Phys. Rev. B* **72**, 035122.
- Sadovsikii, M. V., I. A. Nekrasov, E. Z. Kuchinskii, T. Pruschke, and V. I. Anisimov (2005), *Phys. Rev. B* **72**, 155105.
- Sakai, S., Y. Motome, and M. Imada (2009), *Phys. Rev. Lett.* **102**, 056404.
- Sakai, S., G. Sangiovanni, M. Civelli, Y. Motome, K. Held, and M. Imada (2012), *Phys. Rev. B* **85**, 035102.
- Sandvik, A. W. (1998a), *Phys. Rev. Lett.* **80**, 5196.
- Sandvik, A. W. (1998b), *Phys. Rev. B* **57**, 10287.

- Sarker, S. K. (1988), *J. Phys. C: Solid State Physics* **21** (18), L667.
- Scalapino, D. J. (2012), *Rev. Mod. Phys.* **84**, 1383.
- Schäfer, T., S. Ciuchi, M. Wallerberger, T. P., O. Gunnarsson, G. Sangiovanni, G. Rohringer, and A. Toschi (2016a), *Phys. Rev. B* **94**, 235108.
- Schäfer, T., F. Geles, D. Rost, G. Rohringer, E. Arrigoni, K. Held, N. Blümer, M. Aichhorn, and A. Toschi (2015a), *Phys. Rev. B* **91**, 125109.
- Schäfer, T., A. Katanin, K. Held, and A. Toschi (2016b), preprint arXiv:1605.06355.
- Schäfer, T., G. Rohringer, O. Gunnarsson, S. Ciuchi, G. Sangiovanni, and A. Toschi (2013), *Phys. Rev. Lett.* **110**, 246405.
- Schäfer, T., A. Toschi, and K. Held (2016c), *Journal of Magnetism and Magnetic Materials* **400**, 107.
- Schäfer, T., A. Toschi, and J. M. Tomczak (2015b), *Phys. Rev. B* **91**, 121107.
- Schauerte, T., and P. G. J. van Dongen (2002), *Phys. Rev. B* **65**, 081105.
- Schiller, A., and K. Ingersent (1995), *Phys. Rev. Lett.* **75**, 113.
- Schmalian, J., D. Pines, and B. Stojković (1999), *Phys. Rev. B* **60**, 667.
- Seth, P., I. Krivenko, M. Ferrero, and O. Parcollet (2016), *Computer Physics Communications* **200**, 274 .
- Shinaoka, H., E. Gull, and P. Werner (2017a), *Computer Physics Communications*, (in print).
- Shinaoka, H., J. Otsuki, M. Ohzeki, and K. Yoshimi (2017b), preprint arXiv:1702.03054.
- Shvaika, A. M. (2000), *Physica C* **341-348**, 177.
- Si, Q., and J. L. Smith (1996), *Phys. Rev. Lett.* **77**, 3391.
- Slezak, C., J. M., T. Maier, and J. Deisz (2009), *J. Phys.: Condens. Matter* **21**, 435604.
- Smith, J. L., and Q. Si (2000), *Phys. Rev. B* **61**, 5184.
- Sordi, G., K. Haule, and A.-M. S. Tremblay (2011), *Phys. Rev. B* **84**, 075161.
- Soven, P. (1969), *Phys. Rev.* **178** (3), 1136.
- Staar, P., T. A. Maier, and T. C. Schulthess (2012), *Journal of Physics: Conference Series* **402** (1), 012015.
- Staar, P., T. A. Maier, M. S. Summers, G. Fourestey, R. Solca, and T. C. Schulthess (2013), in *Proceedings of the International Conference on High Performance Computing, Networking, Storage and Analysis*, SC '13 (ACM, New York, NY, USA) pp. 1:1–1:11.
- Stan, A., P. Romaniello, S. Rigamonti, L. Reining, and J. A. Berger (2015), *New J. Phys.* **17** (9), 093045.
- Stanescu, T. D., and G. Kotliar (2004), *Phys. Rev. B* **70**, 205112.
- Stepanov, E. A., A. Huber, E. G. C. P. van Loon, A. I. Lichtenstein, and M. I. Katsnelson (2016a), *Phys. Rev. B* **94**, 205110.
- Stepanov, E. A., E. G. C. P. van Loon, A. A. Katanin, A. I. Lichtenstein, M. I. Katsnelson, and A. N. Rubtsov (2016b), *Phys. Rev. B* **93**, 045107.
- Sun, P., and G. Kotliar (2002), *Phys. Rev. B* **66**, 085120.
- Sun, P., and G. Kotliar (2004), *Phys. Rev. Lett.* **92**, 196402.
- Sweep, J., A. Rubtsov, and M. Katsnelson (2013), *JETP Letters* **98** (7), 427.
- Tahvildar-Zadeh, A. N., J. K. Freericks, and M. Jarrell (1997), *Phys. Rev. B* **55**, 942.
- Takahashi, M. (1977), *J. Phys. C: Solid State Physics* **10** (8), 1289.
- Takemori, N. (2016), *Strong electron correlation effects in a quasiperiodic lattice*, Ph.D. thesis (Tokyo Institute of Technology).
- Takemori, N., A. Koga, and H. Hafermann (2016), *J. Phys.: Conference Series* **683** (1), 012040.
- Tam, K.-M., H. Fotsos, S.-X. Yang, T.-W. Lee, J. Moreno, J. Ramanujam, and M. Jarrell (2013), *Phys. Rev. E* **87**, 013311.
- Tanaka, (2016), private communication.
- Taranto, C., S. Andergassen, J. Bauer, K. Held, A. Katanin, W. Metzner, G. Rohringer, and A. Toschi (2014), *Phys. Rev. Lett.* **112**, 196402.
- Taylor, D. W. (1967), *Phys. Rev.* **156**, 1017.
- Terasaki, I., Y. Sasago, and K. Uchinokura (1997), *Phys. Rev. B* **56**, R12685.
- Terletska, H., C. E. Ekuma, C. Moore, K.-M. Tam, J. Moreno, and M. Jarrell (2014), *Phys. Rev. B* **90** (9), 094208.
- Terletska, H., S.-X. Yang, Z. Y. Meng, J. Moreno, and M. Jarrell (2013), *Phys. Rev. B* **87** (13), 134208.
- Thouless, D. (1974), *Phys. Rep.* **13** (3), 93.
- Tomczak, J. M. (2015), *J. Phys.: Conference Series* **592** (1), 012055.
- Tomczak, J. M., M. Casula, T. Miyake, F. Aryasetiawan, and S. Biermann (2012a), *EPL (Europhysics Letters)* **100** (6), 67001.
- Tomczak, J. M., M. Casula, T. Miyake, and S. Biermann (2014), *Phys. Rev. B* **90**, 165138.
- Tomczak, J. M., P. Liu, A. Toschi, G. Kresse, and K. Held (2017), preprint arXiv:1703.08446.
- Tomczak, J. M., M. van Schilfgaarde, and G. Kotliar (2012b), *Phys. Rev. Lett.* **109**, 237010.
- Toschi, A., A. Katanin, and K. Held (2007), *Phys. Rev. B* **75**, 045118.
- Toschi, A., G. Rohringer, A. Katanin, and K. Held (2011), *Annalen der Physik* **523** (8-9), 698.
- Valli, A., H. Das, G. Sangiovanni, T. Saha-Dasgupta, and K. Held (2015a), *Phys. Rev. B* **92**, 115143.
- Valli, A., G. Sangiovanni, O. Gunnarsson, A. Toschi, and K. Held (2010), *Phys. Rev. Lett.* **104**, 246402.
- Valli, A., G. Sangiovanni, A. Toschi, and K. Held (2012), *Phys. Rev. B* **86**, 115418.
- Valli, A., T. Schäfer, P. Thunström, G. Rohringer, S. Andergassen, G. Sangiovanni, K. Held, and A. Toschi (2015b), *Phys. Rev. B* **91**, 115115.
- Vilk, Y. M., and A.-M. S. Tremblay (1996), *EPL (Europhysics Letters)* **33** (2), 159.
- Vilk, Y. M., and A.-M. S. Tremblay (1997), *J. Phys. I France* **7** (11), 1309.
- Vollhardt, D., N. Blümer, K. Held, M. Kollar, J. Schlipf, M. Ulmke, and J. Wahle (1998), *Advances In Solid State Physics* **38**, 383.
- Wahle, J., N. Blümer, J. Schlipf, K. Held, and D. Vollhardt (1998), *Phys. Rev. B* **58**, 12749.
- Wang, N. L., P. Zheng, D. Wu, Y. C. Ma, T. Xiang, R. Y. Jin, and D. Mandrus (2004), *Phys. Rev. Lett.* **93**, 237007.
- Wehling, T. O., E. Şaşoğlu, C. Friedrich, A. I. Lichtenstein, M. I. Katsnelson, and S. Blügel (2011), *Phys. Rev. Lett.* **106**, 236805.
- Wentzell, N., G. Li, A. Tagliavini, C. Taranto, G. Rohringer, K. Held, A. Toschi, and S. Andergassen (2016), arXiv:1610.06520.
- Wentzell, N., C. Taranto, A. Katanin, A. Toschi, and S. Andergassen (2015), *Phys. Rev. B* **91**, 045120.
- Werner, P. (2013), private communication.

- Werner, P., M. Casula, T. Miyake, F. Aryasetiawan, A. J. Millis, and S. Biermann (2012), *Nat. Phys.* **8**, 331.
- Werner, P., A. Comanac, L. de' Medici, M. Troyer, and A. J. Millis (2006), *Phys. Rev. Lett.* **97**, 076405.
- Werner, P., and A. J. Millis (2006), *Phys. Rev. B* **74**, 155107.
- Werner, P., and A. J. Millis (2007), *Phys. Rev. Lett.* **99**, 146404.
- Werner, P., and A. J. Millis (2010), *Phys. Rev. Lett.* **104**, 146401.
- Wilhelm, A., F. Lechermann, H. Hafermann, M. I. Katsnelson, and A. I. Lichtenstein (2015), *Phys. Rev. B* **91**, 155114.
- Wissgott, P., A. Toschi, G. Sangiovanni, and K. Held (2011), *Phys. Rev. B* **84**, 085129.
- Wissgott, P., A. Toschi, H. Usui, K. Kuroki, and K. Held (2010), *Phys. Rev. B* **82**, 201106(R).
- Wu, W., and A.-M. S. Tremblay (2014), *Phys. Rev. B* **89**, 205128.
- Yang, S.-X., H. Fotso, H. Hafermann, K.-M. Tam, J. Moreno, T. Pruschke, and M. Jarrell (2011), *Phys. Rev. B* **84**, 155106.
- Yang, S. X., H. Fotso, J. Liu, T. A. Maier, K. Tomko, E. F. D'Azevedo, R. T. Scalettar, T. Pruschke, and M. Jarrell (2009), *Phys. Rev. E* **80**, 046706.
- Yang, S.-X., P. Haase, H. Terletska, Z. Y. Meng, T. Pruschke, J. Moreno, and M. Jarrell (2014), *Phys. Rev. B* **89**, 195116.
- Yang, S.-X., H. Terletska, Z. Y. Meng, J. Moreno, and M. Jarrell (2013), *Phys. Rev. E* **88**, 063306.
- Yoshioka, T., A. Koga, and N. Kawakami (2009), *Phys. Rev. Lett.* **103**, 036401.
- Yudin, D., D. Hirschmeier, H. Hafermann, O. Eriksson, A. I. Lichtenstein, and M. I. Katsnelson (2014), *Phys. Rev. Lett.* **112**, 070403.
- Zhang, Y., and J. Callaway (1989), *Phys. Rev. B* **39**, 9397.
- Zhu, J.-X., D. R. Grempel, and Q. Si (2003), *Phys. Rev. Lett.* **91**, 156404.
- Žonda, M., P. Farkašovský, and H. Čenčariková (2009), *Solid State Commun.* **149** (45-46), 1997.